



JOHANNES-GUTENBERG-UNIVERSITÄT MAINZ
FACHBEREICH CHEMIE, PHARMAZIE UND GEOWISSENSCHAFTEN
INSTITUT FÜR PHYSIKALISCHE CHEMIE

Dissertation zur Erlangung des Grades "Doktor der
Naturwissenschaften" im Promotionsfach Chemie

Revealing atomic-scale details in the force fields above carbonate surfaces

Stefan Kuhn

geboren in Frankenthal (Pfalz)

Mainz, den 09. Februar 2015

This thesis was supervised by [REDACTED] and was carried out at the Johannes Gutenberg-Universität Mainz from April 2012 to March 2015.

D77 (Dissertation Johannes Gutenberg-Universität Mainz)

Dean of the Faculty

[REDACTED]

1st report

[REDACTED]

Johannes Gutenberg-Universität Mainz

2nd report

[REDACTED]

Max Planck Institut für Polymerforschung Mainz

Submitted: 09 February 2015

Oral examination: 21 April 2015

Für meine Familie

"It is exciting to discover electrons and figure out the equations that govern their movement; it is boring to use those principles to design electric can openers. From here on out, it's all can openers."

NEAL STEPHENSON

Contents

1	Introduction	1
2	Techniques	5
2.1	Non-contact atomic force microscopy	6
2.1.1	Frequency modulation	6
2.1.2	Working principle	8
2.2	Forces	10
2.2.1	Electrostatic forces	11
2.2.2	Van der Waals forces	12
2.2.3	Short-range forces	14
2.3	Experimental set-up	14
2.4	Atom-tracking	16
2.5	Force mapping	19
2.5.1	Acquisition approaches	20
2.5.2	Scan protocol	21
3	Calculation of forces, potential and dissipation	25
3.1	Recovery of the vertical force $F_z(z)$	26
3.1.1	Procedure for evaluating the recovery quality	26
3.1.2	General strategy	27
3.1.3	Filtering	31
3.2	Deconvolution of the potential	33
3.3	Calculation of lateral forces	35
3.4	Rescaling of the dissipation	35
4	Strategy for extracting short-range forces	39
4.1	Introduction	40
4.2	Example data	42
4.3	Models	43
4.4	Fit and subtraction strategies	48
4.4.1	Model selection	49
4.4.2	Refinement of the cutoff position	52
4.5	Error analysis	55
4.6	Conclusion	56

5	Bulk insulator surfaces	59
5.1	Calcite CaCO_3	59
5.2	Dolomite $\text{CaMg}(\text{CO}_3)_2$	61
5.3	Magnesite MgCO_3	63
6	Force mapping experiments on bulk insulators	67
6.1	Identifying the absolute orientation of a low-symmetry surface in real space	68
6.1.1	Introduction	68
6.1.2	Properties of calcite	69
6.1.3	Optical identification	70
6.1.4	Tip-sample force measurement	71
6.1.5	Discussion	74
6.1.6	Conclusions	77
6.2	Force mapping on other bulk insulators	78
6.2.1	Magnesite	78
6.2.2	Dolomite	82
6.3	Aim for chemical identification	83
7	Summary	87
	Bibliography	91
A	Parameter dependency of fit models	97
B	Supplementary data for 2D force slice and additional datasets	101
C	Details on the short-range force extraction for the magnesite data	109
D	Details on the short-range force extraction for the dolomite data	113
E	MATLAB Code for fitting a van der Waals Model	115
	Acknowledgements	127
	Publications and presentations	129
	Curriculum vitae (educational)	131

Nature has the habit of fascinating us with the most amazing and influential processes to shape life for centuries to an unparalleled extent. The most fundamental ones are beyond our understanding and are therefore researched by many different fields of science. The formation of biominerals is one of them. When an inorganic material combines with organic molecules they can form a new compound material with outstanding properties. These compounds are called biominerals and are formed in the process of biomineralisation. In terms of material science these biominerals attract a great deal of attention, as it is desirable to understand and to copy their formation to ultimately achieve the ability to influence the material properties in any desired way [1].

Calcite, one of the most abundant simple salts in nature, is the most stable polymorph of CaCO_3 and plays a major role in biomineralisation. CaCO_3 can be found in molluscs in form of the shells of slugs. Mother-of-pearl, or nacre, is a well-known biomineral of calcite. Besides several interesting application-oriented aspects [2–5], calcite is furthermore a candidate to potentially explain the homochirality of life [6]. This is deduced from the fact that amino acids are naturally found in one specific chirality, only. The cause for this remains undiscovered, but an enantiospecific adsorption of amino acids on calcite might be a possible explanation [7]. Furthermore, an enantiospecific influence on the macroscopic growth of calcite has been demonstrated [8]. Therefore, chirality and the knowledge of absolute surface directions play a significant role when investigating calcite.

Calcite is not the only abundant rock-forming mineral. Closely related to calcite are the minerals dolomite $\text{CaMg}(\text{CO}_3)_2$ and magnesite MgCO_3 . All of these materials play a prominent role in the carbon cycle [9]. This cycle describes the level of atmospheric carbon dioxide CO_2 which is a balance between two processes: First, the uptake of CO_2 into the mineral by weathering from silicate to carbonate rocks and, second, the vice versa reaction by precipitation of silicate rocks and therefore a release of CO_2 into the atmosphere. Equilibrium reactions between the respective kind of rocks result in the formation and dissolving of the Mg^{2+} and Ca^{2+} carbonates calcite, magnesite and dolomite. A discussion of the today's carbon cycle is still prevailing, for instance, due to the changed weathering rates of the present day. In addition, dolomite is also known for the so-called "dolomite problem" [10]. Here the denomination already indicates that some aspects about dolomite seem to remain undiscovered. The "dolomite problem" describes the still unexplained fact that although dolomite can widely be found in sedimentary rocks, it is virtually

non-existent in modern marine depositional environments. Therefore, dolomite has so far not been produced synthetically under aqueous conditions in the laboratory. All of this is in sharp contrast to calcite.

In every respect, as stated above, it is necessary to gain deeper insight into the material properties at the nanoscale. Regarding calcite, for example, the adsorption of chiral molecules is relevant for biomineralisation, thus, the understanding of the surface symmetry is crucial. Consequently, the measurement of the surface force field at the atomic level becomes the focal point of interest. The knowledge of the force field does not only shed light on the interaction with molecules to gain a better understanding on the biomineralisation of calcite, but also holds the possibility to resolve atomistic processes and the identification of surface properties.

When it comes to measuring forces at the nanoscale the atomic force microscope (AFM) [11] immediately comes to mind. The AFM even holds the power to resolve single atoms on a crystalline surface when operated in the non-contact (NC) mode [12]. Yet, a commercial set-up to measure a surface force field is not available. This not only raises the problem of how to measure the force field in principle, but even more, also very fundamental technical aspects have to be handled.

To measure the force field, a so-called force map, it is not sufficient to just regularly scan over a surface, but it is indispensable to quantify the distance dependency of the interaction. Different propositions to do so have been made, so a suitable mode has to be found and implemented first. In order to achieve information that is helpful in the context of biomineralisation, the measurements have to be carried out at room temperature. This, however, introduces the obstacle of thermal drift. To allow for a high-precision force map measurement over a long period, typically 16 h for the case of this work, but more has been reported, the thermal drift has to be compensated for effectively. An introduction to the technical details and a presentation of the implemented force mapping protocol used for this work is given in Chapter 2.

Implementing a scan protocol does not readily give the desired data, but further processing must take place, i.e. the actual calculation of the force. This is a complicated task where many possibilities for a force calculation have been offered, which are also dependent on the experimental parameters for each study. Especially when smoothing the data is necessary, a generalized protocol can not be given, that is why the force calculation has to be reconsidered for every set of different experimental parameters. Chapter 3 describes how the force is calculated and how other important physical parameters were determined in this work to exploit the full potential of the force mapping technique.

For understanding the atomistic processes of the surface, the chemical forces are of utmost importance. The force measured in a force map, though, is a composition of several contributions of long-range and short-range nature, which cloud the interaction of interest, the chemical forces. Separating the chemical short-range forces from the net force is a highly delicate and error-prone task. While some contributions of long-range nature, like electrostatics, can be compensated for in an NC-AFM measurement, other contributions, like the van der Waals interaction, are ubiquitous and can not be neglected. To subtract this kind of interaction, a suitable model for the tip shank has to be found and fitted to the data. This bears a very high risk to produce wrong short-range force data.

Chapter 4 describes extensively, how this highly demanding task was mastered and how trustworthy short-range forces were obtained to allow for an interpretation of the force field data. A detailed study of the errors gives even more confidence in this newly found strategy.

The analysed data are presented in Chapter 6 and show that one of the fundamental surface properties could be identified by force mapping: the absolute orientation of the $\text{CaCO}_3(10.4)$ surface. The data reveal an unusual contrast that allows for a microscopic assignment of the surface directions. Though this unusual contrast leaves the question of whether it is an artefact or not. It could be cleared by several repeated measurements that the contrast in the data is of physical origin. By inspecting the short-range and the lateral forces a contrast formation mechanism could be identified that includes a relaxation of the carbonate groups within the surface.

A comparison of the force fields of different carbonates, i.e. magnesite and dolomite, exhibits the possibility of chemically identifying the varying cations with a microscopic technique. Final evidence for a clear assignment of the different cations is missing though.

This work gives, therefore, a comprehensive study of the demanding force mapping technique. Ranging from fundamental technical aspects to a dense interpretation of the data revealing atomic-scale mechanisms, this work is not only a guideline for correct data acquisition and extraction of the desired forces but also contributes to interesting questions in the field of biomineralisation.

Contents

2.1	Non-contact atomic force microscopy	6
2.1.1	Frequency modulation	6
2.1.2	Working principle	8
2.2	Forces	10
2.2.1	Electrostatic forces	11
2.2.2	Van der Waals forces	12
2.2.3	Short-range forces	14
2.3	Experimental set-up	14
2.4	Atom-tracking	16
2.5	Force mapping	19
2.5.1	Acquisition approaches	20
2.5.2	Scan protocol	21

The method of choice to obtain a detailed understanding about atomistic processes on insulator surfaces is the non-contact atomic force microscope (NC-AFM) operated in the frequency modulated (FM) mode. This is for two reasons. First, the AFMs predecessor the scanning tunnelling microscope (STM), which also allows for real space imaging of surfaces, is restricted to conducting surfaces. Second, atomistic processes on surfaces are subject to various kinds of forces, which can be measured, visualised and even separated post data acquisition with the elaborate force mapping technique, only accessible with the NC-AFM.

Therefore, a brief introduction to NC-AFM will be given in Section 2.1 explaining the FM mode and the working principle, followed in Section 2.2 by an overview of the forces typically present at NC-AFM. The experimental set-up, introducing the ultra-high vacuum (UHV) apparatus, is described in Section 2.3. An indispensable tool for this work was a home-built atom-tracking system. It was used for drift compensation, since all measurements took place at room temperature, which poses a severe drift environment. An introduction to this technique can be found in Section 2.4. In Section 2.5 follows a general description of force mapping experiments, comprising the discussion of different data acquisition approaches as well as an introduction to the implemented method.

2.1 Non-contact atomic force microscopy

The scanning tunnelling microscope (STM), invented in 1981 [13], states the ancestor of a huge variety of scanning probe microscopy (SPM) techniques and so opens up a whole new field in surface science. For the first time it allowed for imaging of surfaces in real space. STM is based on measuring the tunnelling current between a metallic probe and a conducting surface. Consequently, it is restricted to metallic samples.

This limitation was overcome in 1986 with the design of the atomic force microscope (AFM), which can visualise the topography of insulating surfaces in real space [11]. This is realised by a very sharp tip which is attached to the free end of a cantilever. This tip is brought in close proximity and then scanned across a sample surface. In its most basic operation mode, the so-called *contact mode*, the tip is pressed onto the sample surface. Due to the interaction of sample and tip, the deflection of the cantilever is changed. To detect this deflection, a laser beam is focussed on the free end of the cantilever, which is then reflected to a photosensitive diode. In this beam-deflection configuration [14] the deflection of the cantilever, which is the measurement signal, is detected via the laser deflection on the detector.

2.1.1 Frequency modulation

When working with the FM technique [15] the cantilever motion is, contrary to the *contact mode*, no longer static, but excited to its eigenfrequency f_0 at a certain pre-set amplitude A . When the tip is brought into the interaction range of the sample, f_0 changes to the current eigenfrequency f , which deviates from the eigenfrequency f_0 . It follows that the measurement signal is then a frequency shift $\Delta f = f - f_0$. The frequency shift Δf is a function of the force between tip and sample F_{ts} , so it is desirable to deduce an expression connecting Δf and F_{ts} .

For the free oscillation, the cantilever is a harmonic oscillator, so f_0 is

$$f_0 = \frac{1}{2\pi} \sqrt{\frac{k}{m^*}}, \quad (2.1)$$

with k being the cantilever spring constant and m^* the effective mass of the cantilever.

Now the interaction of tip and sample has to be considered which induces a disturbance. It can be described by the tip-sample force gradient $k_{ts} = \frac{\partial F_{ts}}{\partial z}$ [16]. The current eigenfrequency f can now be written as

$$f = \frac{1}{2\pi} \sqrt{\frac{k + k_{ts}}{m^*}}. \quad (2.2)$$

In case of small oscillation amplitudes A in the sub-Å range, k_{ts} can be treated as constant [15]. Figure 2.1 (a) sketches the resonance curves for a free (black) and a disturbed cantilever (blue), respectively. It is immediately visible that f is reduced for the interacting cantilever. In general this is true for an attractive interaction between tip and sample, since k_{ts} has a negative sign in that case. Consequently, Δf will be negative since it is defined as $\Delta f = f - f_0$. For the scanning process this is illustrated in Fig. 2.1 (b) above a corrugated surface. Far away the cantilever oscillates at f_0 , but when brought closer to the surface the measured Δf is reduced when the tip is in the attractive interaction regime above a surface feature.

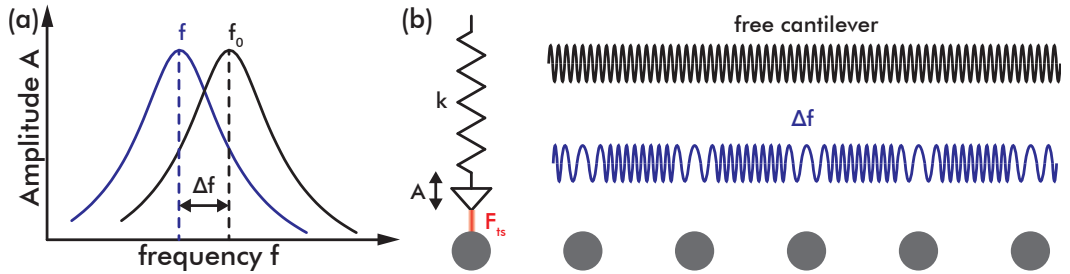


Fig. 2.1.: (a) Resonance curves for a free (black) and a disturbed (blue) cantilever, respectively. (b) Frequency behaviour of the cantilever far away (black) and close to the sample surface (blue). Adapted from [17].

To obtain an expression for Δf as a function of the force gradient, Eqs. (2.1) and (2.2) can be used. Since usually $k_{ts} \ll k$ the equation for Δf can be expanded in a Taylor series, so in the end it gives

$$\Delta f = f_0 \frac{k_{ts}}{2k}. \quad (2.3)$$

Since in this entire work exclusively large amplitudes ($A \sim 15$ nm) were used, the assumption that $k_{ts} = \text{const.}$ does not hold true any more. Therefore, the interaction has to be averaged over a whole oscillation cycle within the bounds from 0 to $T = 1/f_0$ [18], giving

$$\Delta f = -\frac{f_0}{kA^2} \langle F_{ts}q \rangle, \quad (2.4)$$

where q describes the motion of the cantilever along the vertical Z axis and the brackets indicate the averaging over a whole oscillation cycle. Using the equation of motion for the cantilever $q = A\cos(2\pi f_0 t)$ this gives [18]:

$$\Delta f(z) = \frac{f_0}{\pi k A^2} \int_{-A}^A F_{ts}(z + A - q) \frac{q}{\sqrt{A^2 - q^2}} dq. \quad (2.5)$$

This shows that Δf is also a function of the tip-to-sample distance z . Equation (2.5) now can be integrated partially from where a convolution with a weight function of semispherical shape results which describes the movement of the cantilever of a full oscillation cycle [18]. This can be normalised with the factor $\frac{2}{\pi A^2}$ describing the area of the semicircle, so it follows

$$\Delta f(z) = \frac{f_0}{2k} \frac{2}{\pi A^2} \int_{-A}^A k_{ts} \sqrt{A^2 - q^2} dq \quad (2.6)$$

$$= \frac{f_0}{2k} \langle k_{ts} \rangle. \quad (2.7)$$

In order to obtain the ability to compare different large-amplitude experiments, the so-called normalised frequency shift has been introduced [19]. Under the large-amplitude assumption, a formula for the frequency shift can be deduced that is no longer dependent on the specific amplitude. It reads

$$\gamma(z) = \frac{kA^{\frac{3}{2}}}{f_0} \Delta f(z, A, k, f_0), \quad (2.8)$$

where γ is the normalised frequency shift. $\gamma(z)$ has the advantage that it condenses four parameters to fully describe a NC-AFM experiment in one. Consequently multiple $\Delta f(z)$ -curves recorded with different amplitudes condense to one $\gamma(z)$ -curve. It follows that all $\Delta f(z)$ -curves give the same $F_z(z)$ -curve. This has been validated experimentally for amplitudes larger than 5.4 nm [20].

2.1.2 Working principle

Only nine years after the invention of the AFM and four years after the introduction of the FM technique first reports of true atomic resolution have been given [12, 21] where from NC-AFM became a tool of major relevance in the field of surface science.

Since then atomic resolution has been shown with this technique on many surfaces [22]. Even atomic resolution on molecules was achieved [23] as well as subatomic resolution [24], although the latter results are still under controversial discussion.

All the mentioned results as well as all data within this thesis used a NC-AFM that has been operated in the previously described FM mode (see Section 2.1.1). The employed experimental set-up is schematically shown in Fig. 2.2.

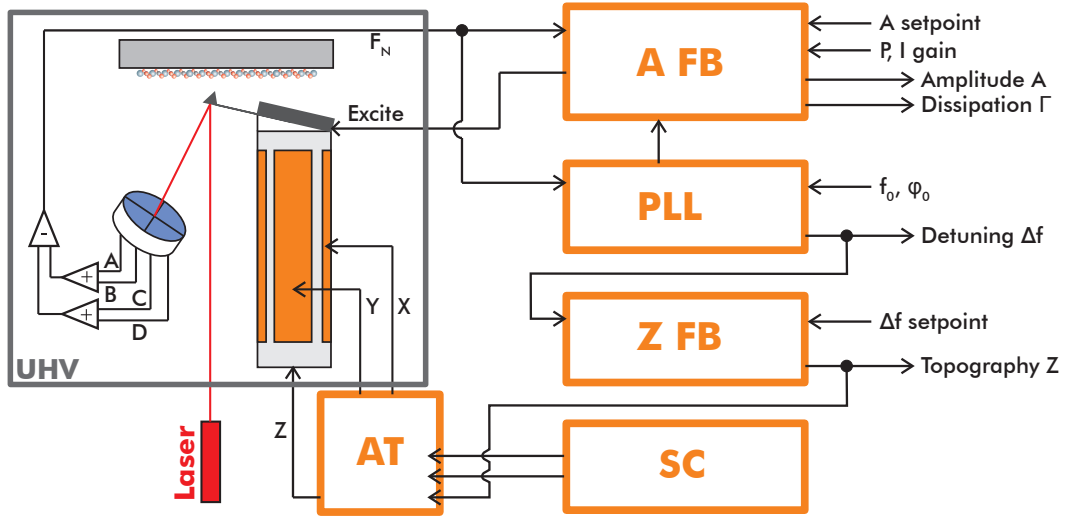


Fig. 2.2.: NC-AFM set-up as used throughout this thesis. The left side shows the components within the UHV chamber. To them belong the scan head with the piezo tube and the cantilever, the beam-deflection set-up with a photodiode and the sample. The right side depicts the electronics, including the amplitude feedback (A FB), phase-locked loop (PLL), distance feedback (Z FB), scan controller (SC) and an atom-tracking system (AT). Adapted from [25].

As described earlier, working with an AFM using the beam-deflection technique a laser is focussed on the back of the cantilever, from where it is reflected to a photo-sensitive diode. In our case this is a four quadrant photodiode where, in analogy to *contact mode*, the deflection signal F_N is calculated as the difference in intensity of the upper and lower half of the diode. F_N contains the main signal of interest, namely the current frequency f and the amplitude A of the oscillation and, thus, fully describes the cantilever motion. F_N , therefore, is a sinusoidal function.

In the following F_N is fed to a phase-locked loop (PLL). Here the phase difference between the excitation and the input signal is compared to determine $\Delta f = f - f_0$, where f_0 is identified before starting the experiment. The PLL constitutes the first feedback loop in this set-up, because it always fixes the phase difference to 90° . As a consequence a separation of conservative and dissipative interaction is possible. It follows for this set-up that Δf is the main measurement signal.

When feeding this signal into a second feedback loop, the distance feedback (Z FB), Δf is adjusted to a setpoint chosen by the operator. Due to the distance dependency of Δf as was shown in Eq. (2.5), a variation of the setpoint alters the tip-to-sample

distance. The output of the Z feedback can be extracted to image the topography. In addition a third feedback loop is employed, namely the amplitude feedback (A FB). Here the amplitude A of the input signal F_N is detected. If the detected amplitude deviates from the amplitude setpoint, the excitation voltage is changed for restoring the preset oscillation amplitude, keeping it constant during the whole measurement. This is of major importance as discussed in Section 3.1. This adjusted excitation is a measure for the energy that is lost due to dissipative processes and can be extracted as another imaging signal besides Δf . This channel is called dissipation Γ .

A scan controller (SC) applies voltages to the piezo scanner to allow for the scanning movement of the tip in lateral and vertical direction, while the excitation signal is applied to the tip by the amplitude feedback. Deviating from this standardized commercial set-up, an additional home-built atom-tracking (AT) system [25, 26] is employed throughout all measurements presented in this thesis. It adds an additional low-voltage signal to the high-voltage output of the scan controller. With the atom-tracking system, it is possible to compensate for thermal drift during the measurement to obtain virtually drift free images without post-processing and ensure utmost stability of the positioning of the tip on a specific sample site.

2.2 Forces

The measured frequency shift in an NC-AFM experiment is induced by a force acting between the tip and the sample. Often it is analytically described by the force that can be derived from the empirical Lennard-Jones potential [27]. Potential and force are in general connected by

$$F = -\nabla U, \quad (2.9)$$

where the potential is denoted with U . The Lennard-Jones potential which accounts for a pairwise interaction of atoms is given by

$$U_{LJ}(z) = -E_{Bond} \left[2 \left(\frac{\sigma}{z} \right)^6 - \left(\frac{\sigma}{z} \right)^{12} \right], \quad (2.10)$$

while the respective force law reads

$$F_{LJ}(z) = -12 \frac{E_{Bond}}{\sigma} \left[\left(\frac{\sigma}{z} \right)^7 - \left(\frac{\sigma}{z} \right)^{13} \right]. \quad (2.11)$$

Here E_{Bond} is the bonding energy and σ the equilibrium distance, where attractive and repulsive forces cancel each other out. Equation (2.10) shows that the interaction between two atoms is described by a repulsive (z^{-12} , Pauli repulsion) and an attractive term (z^{-6} , van der Waals), respectively. The Lennard-Jones potential as well as the derived force are shown in Fig. 2.3 with the region of repulsive interaction marked as the blue shaded area.

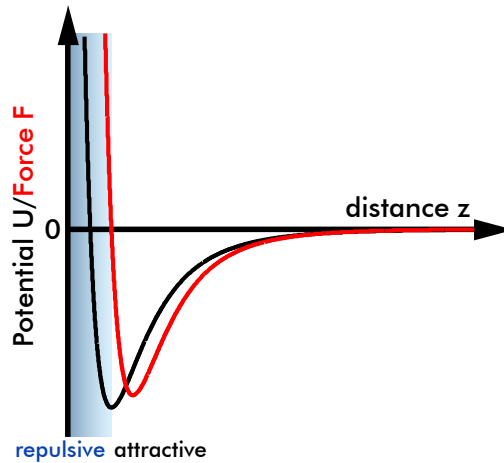


Fig. 2.3.: Lennard-Jones potential (black) and the resulting force (red). The region of repulsive interaction is marked with the blue shaded area and starts at $z = \sigma$.

It is obvious that attractive forces always have a negative and repulsive forces have a positive sign.

The vertical force is usually composed of various contributions and it is a highly non-trivial task to separate these contributions from the experimentally obtained net force F_{ts} . The relevant forces for NC-AFM can be classified in terms of their range. Typical long-range forces are electrostatic and van der Waals forces. Chemical forces, among which, for instance, Pauli repulsion is counted, are of short-range nature and usually responsible for atomic contrast.

2.2.1 Electrostatic forces

Electrostatic forces are of long-range nature and occur in general when a potential difference is present between tip and sample. Causes for this might be, in case of two metals for instance, a different work function of the tip and the sample, which

causes a contact potential difference (CPD). Also localized charges can remain on the surface after cleaving an insulating bulk crystal *in situ*. For describing electrostatic forces F_{ES} the tip and the sample are treated as a capacitor with capacitance C . This results in the equation

$$F_{ES} = -\frac{1}{2} \frac{dC(z)}{dz} (V_{DC} - \Delta V)^2, \quad (2.12)$$

where V_{DC} is an externally applied DC voltage and ΔV the potential difference. Electrostatic forces can be minimized by externally applying $V_{DC} = \Delta V$ to the tip, where ΔV is measured at the beginning of the experiment. Sophisticated methods like Kelvin Probe Force Microscopy (KPFM) exist, where ΔV (CPD for metals) is compensated for at every scanning point, which allows for directly imaging electrostatic forces [28, 29]. For the measurements in this work it usually is sufficient though to minimize an overall potential difference for the chosen scan area.

2.2.2 Van der Waals forces

Van der Waals forces describe electrostatic dipole-dipole interactions and can be divided into three categories. These are interactions of two permanent dipoles (Debye interaction), a permanent and an induced dipole (Keesom interaction) and of two induced dipoles (London dispersion forces). Dispersion forces are, in contrast to electrostatics, ubiquitous and can not be neglected in an AFM experiment. Van der Waals forces are of long-range nature and under the conditions of this work always attractive.

To obtain an expression for the interaction energy $U(z)$ in case of two neutral atoms, their mutual polarizability [30] has to be accounted for. It can be written:

$$U(z) = -\frac{C}{z^6}, \quad (2.13)$$

where C is a constant containing the two atoms' material properties.

Since van der Waals forces are of long-range nature the whole macroscopic tip shank has to be considered for the case of AFM. Accordingly, there are uncountable dipole-dipole interactions between the tip and the sample, which makes considering every single interaction complicated. For such conditions Hamaker offered a solution by treating the examined bodies as continuous materials, characterized by their particular material properties [31]. Usually the interacting bodies are described by a

Hamaker integration over all atoms of a specific macroscopic geometry. This can be written in the general form

$$F_{\text{vdW}} = \rho_t \rho_s \int_{V_t} \int_{V_s} -\nabla \left(-\frac{C}{z^6} \right) dV_t dV_s, \quad (2.14)$$

where $\rho_{t,s}$ are the materials densities and $V_{t,s}$ the respective volumes for tip and sample. The material properties are condensed in the Hamaker constant $H = \pi^2 C \rho_t \rho_s$ [31], so Eq. (2.14) can be rewritten as

$$F_{\text{vdW}} = H \int_{V_t} \int_{V_s} -\nabla \left(-\frac{1}{z^6} \right) \frac{1}{\pi^2} dV_t dV_s. \quad (2.15)$$

Regarding AFM, there are many different geometries to describe the tip, resulting in many different formulas and, consequently, different distance dependencies. A simple example of a sphere with radius R against an infinite flat sample F_{vdW} results in [32]:

$$F_{\text{vdW}}(z) = -\frac{HR}{6z^2}, \quad (2.16)$$

Another effect of dispersion forces that shall be mentioned here is the retardation effect. Assuming a body A has a spontaneous dipole and emits an electromagnetic wave that reaches body B and induces a dipole compatible to the initial dipole of body A. If the two bodies are significantly far apart from each other, i.e. the distance between the particles is comparable to the wavelength corresponding to the atomic frequencies, an influence of retardation on the interaction has to be expected. This means that the dipole of body A might have changed, before the electromagnetic wave of body B reaches it again [33]. The electromagnetic wave of B and the dipole of A are now no longer compatible to each other. In this case the dispersion energy begins to decay faster (with $\sim -\frac{1}{z^7}$ instead of $-\frac{1}{z^6}$ for atoms). This effect usually plays a role at distances greater than 10 nm [34–37].

2.2.3 Short-range forces

Chemical forces are of short-range nature and can be attractive or repulsive. Chemical binding forces can arise from orbital overlap, bond formation or a repulsion due to the Pauli exclusion principle. When performing an AFM experiment, the chemical forces are of ultimate interest since they provide atomic resolution and an insight into imaging mechanisms or atomistic processes on the surface. An analytically calculated distance dependency for chemical forces can hardly be given, they are often calculated with computational methods.

The sum of all the above mentioned contributions result in the measured net force F_{ts} . How the different contributions compose F_{ts} is exemplarily shown in Fig. 2.4 for the case of a Si tip and a Si sample. Here the chemical force between the frontmost tip atom and a surface atom has been calculated (F_{Si} , black curve) using a Morse force law with parameters for the interaction from [38]. The electrostatic force (F_{el} , green dotted curve) has been calculated for a parallel plate capacitor and the van der Waals interaction (F_{vdW} , blue dashed curve) using the tip model from [39] (also see Fig. 4.3(g)). The sum of all contributions gives F_{ts} (red solid curve).

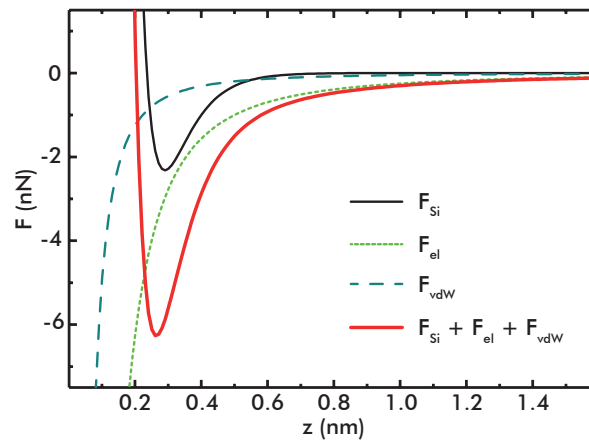


Fig. 2.4.: Common force contributions: chemical short-range (black curve), electrostatic (green dotted curve) and van der Waals interaction (blue dashed curve). The sum of all three contributions compose the solid red curve [40].

2.3 Experimental set-up

The data presented within this thesis were exclusively obtained with a commercially available VT AFM 25 (Omicron Nanotechnology, Taunusstein, Germany) atomic force microscope operated in the frequency modulated non-contact mode using the beam-deflection configuration. Si tips from Nanoworld (Neuchâtel, Switzerland) were used and calcite crystals were purchased from Korth Kristalle (Altenholz (Kiel), Germany), magnesite and dolomite samples from SurfaceNet GmbH (Rheine,

Germany). For amplitude control and frequency-shift detection an easyPLL Plus (Nanosurf, Liestal, Switzerland) was used as well as an HF2 lock-in amplifier (Zurich Instruments AG, Switzerland) for recording thermal spectra. All data were acquired under ultra-high vacuum conditions and at room temperature. The base pressure was well below 10×10^{-10} mbar.

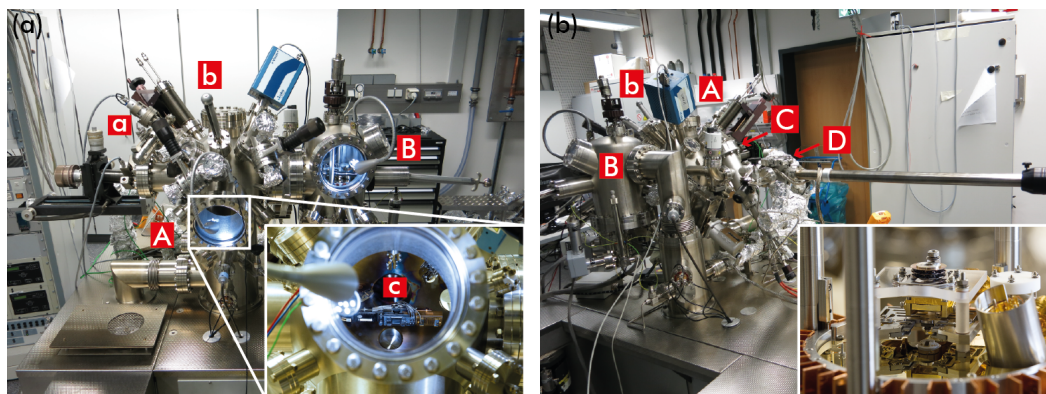


Fig. 2.5.: (a) Front view of the chamber. Inset: Close-up of the preparation chamber with the heating stage ("c") of the manipulator. (b) Rear view of the chamber. Inset: Detailed view of the scan head.

The AFM system consists of four separable chambers as shown on Fig. 2.5. The chamber parts are marked with capital letters, while devices at the chamber are denoted with lower-case letters.

First the load lock (Fig. 2.5(b), marked "D") allows the lock-in and lock-out of samples and tips without breaking the vacuum inside the main chamber. A specially designed evaporator chamber (Fig. 2.5(b), "C") contains a metal evaporator. The preparation chamber (Figs. 2.5 (a) and (b), "A") holds the possibilities for a variety of tip and sample preparation methods like the following. Tips were prepared by Ar^+ -ion sputtering for 5 min at 2 keV and an Argon pressure of 4.4×10^{-6} mbar using the sputter gun (Fig. 2.5 (a), "a"). Fresh sample crystals were mechanically cut to fit into the sample holder [41] and clean surfaces were prepared by *in-situ* annealing in the heating stage (Fig. 2.5 (a), "c") to roughly 280 °C and then cleaved with the cleaver (Figs. 2.5 (a) and (b), "b"). Another subsequent annealing step to about 200 °C was necessary to minimize remaining surface charges. Dolomite and magnesite crystals had to be annealed under much milder conditions. Samples were never annealed above 115 °C and the second annealing step was skipped completely. From my experience annealing to higher temperatures resulted in heavy outgassing of the sample crystals and, thus, dirtier surfaces.

The AFM scan head is placed inside the measurement chamber (Figs. 2.5 (a) and (b), "B") and can be seen in the inset of Fig. 2.5 (b). During the measurement noise was cancelled out via eddy current damping and the temperature was kept constant at a certain setpoint to ensure minimum temperature fluctuation.

2.4 Atom-tracking

When using a scanning probe microscope, thermal drift is an effect which has always to be taken into consideration. Thermal drift is the response of a material to temperature variations entailing a compression or an expansion of the material. For scanning probe methods this is very harmful because images will always show a distortion due to the uncontrolled tip-sample movement. Furthermore, a precise positioning of the tip on the sample surface is prevented as well as long-term measurements with high precision requirements. Additionally, thermal drift is neither linear nor monotonic over time, so a straight forward drift compensation is often impossible. An often used solution is to measure at low temperatures around 4 K, employing a bath cryostat, where the residual thermal drift velocity between 0.1 pm/min and 1 pm/min is so small that it can be neglected [23, 42, 43]. If one is interested in processes at room temperature though, a different approach has to be found since here drift velocities around 100 pm/min and above are present. What can be done is to keep the sample at a constant temperature. Temperature fluctuations are hereby reduced but not eliminated and so is thermal drift. An answer to this problem can be to apply different post-processing methods [43, 44]. However, these methods rely on assumptions that might not always be correct and can, as a consequence, easily entail errors.

This problem can be circumvented when using an atom-tracking system. Such an atom-tracking system allows for precise following/tracking of the movement of surface species with the tip in all spatial directions and, in consequence, ensures drift compensation already during the measurement. This makes the use of post-processing methods completely obsolete.

The possibility to track single atoms was presented for the first time in 1988 by Pohl and Möller [45], designed for the AFM predecessor, the STM. It was later used by Swartzentruber in 1996 and Krueger in 1997 to directly measure the diffusion of single atoms and dimers on a Silicon surface with STM [46, 47], while in 1999 it was used to track the diffusion of hydrogen [48]. The first combined use of atom-tracking and AFM was not before 2005 by Abe *et al.* who used this technique to reproducibly record force spectroscopy curves at room temperature on one specific surface site [49].

Since the aim for the present work was to acquire force spectroscopic data at room temperature for a long duration, an atom-tracking system was indispensable. Consequently, a home-built version [25, 26] was employed throughout this whole work.

Obtaining drift-free images from a standard AFM XY scan is a two-stage process. First, the drift has to be measured by tracking a surface species. Second, the drift velocity and direction, i.e. the drift vector, is applied as an additional voltage to the

piezo scanner to enable the measurement in the same direction and with the same velocity as the drift. The latter step is called *feed-forward* and results in drift-free images.

The whole process takes place during a usual scan. At some arbitrary point during the measurement the XY scanning movement is paused and the tip is centred above a suitable surface species. This can be a single molecule or, if atomic resolution is achieved, a single atom. Afterwards, the tip is oscillating in a circular trajectory around the chosen stationary feature, where it follows a line of equivalent interaction, sketched as the red circle in Fig. 2.6(a). The distance z_{ref} of the tip at the circular trajectory of equivalent interaction (red circle in Fig. 2.6(a)) and the surface is similar to the distance that corresponds to the chosen Δf setpoint during the XY scan.

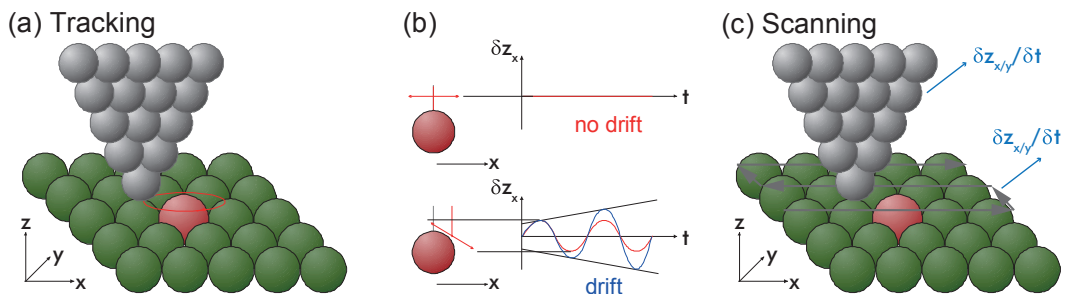


Fig. 2.6.: Atom-tracking principle. (a) Tracking. The tip oscillates in a circular trajectory above a suitable reference site, here: an atom. (b) Top: No drift, tip centred above the atom. The equiline of interaction is parallel, thus, the vertical deviation of the signal δz_x over time is zero. Bottom: Tip is displaced from the atom's centre. The contour line is no longer parallel to the surface, giving an oscillating signal δz_x (red). When introducing drift, the atom moves away from the tip, thus changing the amplitude of δz_x over time (blue). (c) Feed-forward. Stopped oscillation and resumed XY scan. The scanning movement is indicated by the grey arrows. The acquired drift velocities $\frac{\delta z_{x,y}}{\delta t}$ are applied to the tip as shown with the blue arrows. Adapted from [25].

Assume a situation without drift and the tip being centred directly above the species, the contour line is parallel to the surface, see Fig. 2.6(b), top. Therefore, the vertical deviation δz_x is zero. In the case where the tip is not centred above the surface feature, the equiline of interaction is tilted by an angle, shown by the red line in Fig. 2.6(b), bottom. A vertical deviation will be measured, resulting in an oscillation in δz_x . If now drift is introduced, the species continuously moves away from the tip, so that the contour line is tilted more and more, giving an increased vertical deviation as indicated by the blue line of δz_x in Fig. 2.6(b). This is detected in both lateral directions, X and Y.

The vertical deviations in both lateral directions $\delta z_{x,y}$ are fed into a two-phase lock-in amplifier (LIA) where they are separated into the *in-phase* and the *quadrature* signal to provide a measure for the tip displacement in X- and Y-direction, respectively. Two independent feedback loops now correct for δz_x and δz_y . This effectively re-centres the tip above the feature, the tip is locked to it. If this is continued for a certain period of time the tip follows the feature's movement, it is tracking it. The movement

in Z-direction is given by the output of the distance feedback loop.

Before starting an experiment the parameters for the width of the oscillation A_{osc} and its frequency f_{osc} have to be chosen. This should be carried out in accordance with the tracked feature. For all experiments presented in this work A_{osc} was always set to 150 pm to match the size of the oxygen atoms on the $\text{CaCO}_3(10.4)$ surface. The oscillation frequency f_{osc} was set to 20 Hz.

The drift is measured in $x_{drift}(t)$, $y_{drift}(t)$ and $z_{drift}(t)$ and plotted in path-time diagrams, once a stable tracking is ensured. If in a certain time interval the evolution of the drift is roughly linear, a fit can be applied to the data to receive the drift velocity. This can be carried out for each spatial direction, giving the overall direction of the drift. These velocities can now be added as a voltage to the piezo, activating the *feed-forward*. The oscillation of the tip is now stopped and the XY scanning is resumed. In addition to the usual scanning movement, the tip is moved in the same direction as the drift with matching speed, thus compensating for drift during the measurement as sketched in 2.6(c) with blue arrows.

A demonstration of the atom-tracking system is given in Fig. 2.7. At the bottom, atomic resolution on $\text{CaCO}_3(10.4)$ with distorted features is clearly visible. After pausing the scanning process (position indicated with an arrow), exercising the above mentioned procedure on a feature (marked with a circle) and applying the measured drift vector to the piezo scanner, the scan is continued with highly reduced drift as seen in the upper half of Fig. 2.7. The unit cell of the $\text{CaCO}_3(10.4)$ surface, displayed as the white rectangle, matches exactly the imaged features, proving the minimisation of drift.

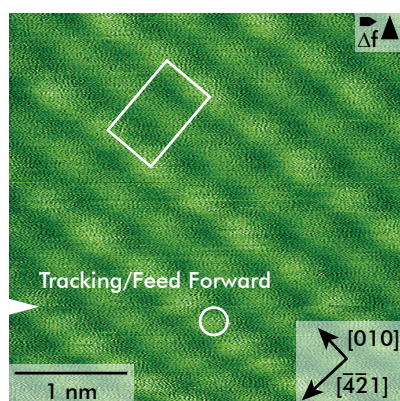


Fig. 2.7.: Demonstration of the employed drift compensation system. The white arrow indicates the line, where the XY scan was paused for drift acquisition and subsequent activation of the *feed-forward*. The chosen tracking feature is marked with a circle, the unit cell of $\text{CaCO}_3(10.4)$ with a rectangle in the upper half, exactly matching the literature values.

The process as described above can be repeated several times to reduce the residual thermal drift to a minimum. More detailed information about the principle, the

implementation and the performance of the employed atom-tracking system have been given in previous studies [25, 26].

2.5 Force mapping

The evolution of AFM advanced rapidly in many regards, so it did not take long until new measurement techniques were presented, one of which attracted major attention. In 2002 the simple scanning of surfaces in a horizontal plane was surpassed by the demonstration of so-called three-dimensional force maps [42]. The implementation of atom-tracking opens up the possibility to acquire these data, where highest precision over a long duration is required. With the force mapping technique the interaction between the tip and the sample is not only recorded in one plane of fixed distance, but extended by the third, the vertical dimension, filling up a data cube. With this technique it is possible to obtain the whole interaction between the tip and the sample as a function of distance for each scan point.

The huge advantage of force maps is that it is now possible to calculate the actual force from the collected data. So far only the frequency shift Δf at one certain distance Z is known, which prevents a conversion to force, as will be discussed later in Chapter 3. In order to convert Δf to force F_{ts} , the distance dependency of Δf is required. The basic idea of force mapping therefore is to measure Δf as a function of distance. With the calculation of the net force F_{ts} and subsequent separation of the chemical short-range forces $F_{z,SR}$ (discussed in Chapter 4), it is possible to gain insight into NC-AFM contrast formation and to unravel the mechanisms behind atomistic processes.

By now a great amount of different force mapping results have been published. Force data have not only been shown on many different substrates, such as metals/metal oxides [42, 50–53], molecules [23, 54–58] and insulators [26, 59–64], but also varying in dimensions, reaching from single point force spectroscopic F_{ts} curves (1D measurements) [65–68] over vertical force lines (2D slices, ZX or ZY mode) [69–72] to full 3D force cubes [50, 73–75]. What mode to choose depends on the goal of the specific study. Even combined AFM and STM studies, where additionally the tunnelling current as a function of distance is measured, have been presented [76–78]. Even force maps in liquid have been demonstrated [79, 80]. In this work, vertical 2D force maps, i.e. slices or ZX measurements, will mainly be shown and that on insulating surfaces.

2.5.1 Acquisition approaches

The basic goal of force mapping, as mentioned before, is to record the frequency shift as a function of distance on a specified grid on the surface. To do so, there are mainly two ways: the *layer-by-layer* and the *curve-by-curve* mode. Both are sketched in the following Fig. 2.8.

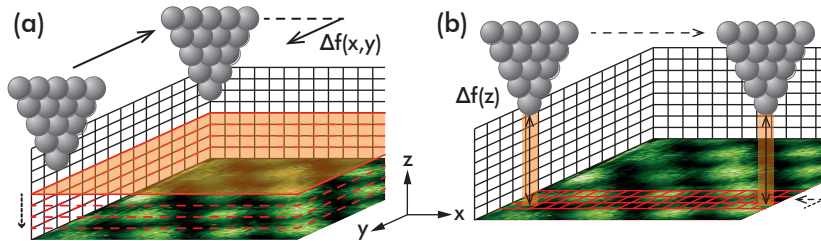


Fig. 2.8.: Force mapping approaches. (a) *layer-by-layer* mode. Consecutive XY planes are recorded with stepwise reduction of the tip-to-sample distance z . (b) *curve-by-curve* mode. $\Delta f(z)$ -curves are recorded along X- and Y-direction, respectively. Adapted from [25].

For the *layer-by-layer* approach, see Fig. 2.8 (a), the Δf vs. z dependency is collected by recording consecutive horizontal planes, just like standard XY scanning, with stepwise decreasing the tip-to-sample distance. It follows, that the fast scan direction is the X-direction and the slow scan direction is the Z-direction. These consecutive images compose the full data cube, giving the $\Delta f(z)$ -relation only indirectly. This method has first been used by Albers *et al.* to record a 3D force map on HOPG at low temperatures [43, 74]. Other results obtained with this approach have been reported [53].

In contrast to this method stands the *curve-by-curve* approach shown in Fig. 2.8(b). This is the approach that has been used by Hölscher *et al.* in the very first 3D force map [42]. Many force maps using this approach have been reported after that [23, 26, 63, 70, 72, 75]. Here, the distance dependency of Δf is measured directly as a $\Delta f(z)$ -curve on a predefined lateral grid. A 3D map is then composed of the consecutive $\Delta f(z)$ -curves in X- and Y-direction, while for a 2D slice only $\Delta f(z)$ -curves along one specified line along X is recorded. Therefore, the fast scan direction is the vertical Z-direction and the lateral X- or Y-direction is the slow scan direction, respectively.

This work exclusively uses the latter technique for three reasons. First, tip changes are easily identified while acquiring the data. Every curve at each position (X,Y) is recorded in a single approach and retract cycle. If a change in the configuration of the tip occurs, the approach and retract curve will deviate heavily from each other, thus, directly indicating the point up to which the data can be used.

Second, if a tip change occurs within the data acquisition, it is possible to use the data up to the point of the tip change for the force recovery and data interpretation. A change in tip configuration means a change in interaction, so data before and after

a tip change can not be treated equally for the data analysis. For the *curve-by-curve* method the whole desired interaction range in vertical direction is covered with each $\Delta f(z)$ -curve, thus at least a part of the full data can be used for interpretation if a tip change occurs. This is quite in contrast to the *layer-by-layer* mode, where the full interaction range is only covered, when the data acquisition is finished completely. So after a tip change during the measurement the partly recorded force map does not contain any useful information.

Third, it is expected to reduce artefacts caused by creep and hysteresis of the scanning piezos as well as residual drift in the *curve-by-curve* approach. Especially, the most sensitive data is sampled nearby the $\Delta f(z)$ and $F_z(z)$ curve minima without vastly repositioning the tip before data acquisition. There has been a theoretical study addressing the different kind of approaches [81] regarding artefacts like piezo creep and thermal drift, but a direct experimental comparison of the two modes with the same tip is still missing.

2.5.2 Scan protocol

The data in this work are solely recorded at room temperature, so the use of the atom-tracking system is mandatory. Since mostly 2D slices will be shown in this thesis, the scan protocol that I used shall exemplarily be visualized for this kind of data in Fig. 2.9. The procedure is easily adaptable for full data cubes.

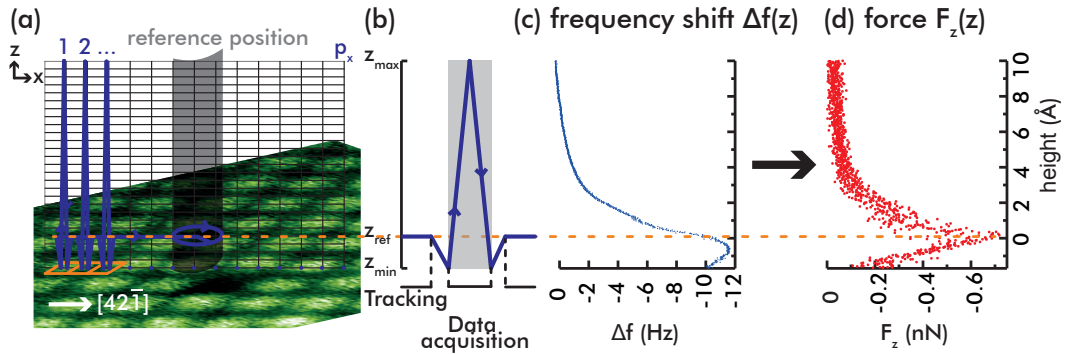


Fig. 2.9.: (a) Scan protocol for the *curve-by-curve* mode, where alternating steps of tracking and data acquisition are used. The total number of $\Delta f(z)$ curves for a single slice is p_x . The dashed orange line marks the reference tip-to-sample distance z_{ref} given by the Δf set point. (b) Timing and Z trajectory of the data acquisition. (c) Exemplary $\Delta f(z)$ curve, showing the frequency shift Δf as a function of tip-to-sample distance z . (d) $F_z(z)$ curve extracted from the raw $\Delta f(z)$ data in (b) with applied filters [72], as it will be discussed in Chapter 3.

Before acquiring the actual 2D slice (ZX mode), I scanned several images in regular AFM imaging (XY mode) with repeated correction for thermal drift. This procedure not only ensures to reduce the effective drift to a minimum already before the 2D data acquisition, but especially decreases scanner creep. The residual drift due to the

non-linear contribution was typically significantly below 100 pm/min before starting the ZX data acquisition.

Figs. 2.9(a) and (b) visualize the scan protocol itself. The atom-tracking technique was used to centre the tip at a reference position usually located in the middle of the slice (grey shaded area in Fig. 2.9(a)). In this case, the reference position is assigned to a single atomic surface site and the tip is moved to every lateral position from this site to acquire a single $\Delta f(z)$ curve. The data acquisition requires a time t_{acq} per curve. After moving the tip back to the reference position, the atom tracking compensates for non-linear drift and creep contributions by precisely re-centring the tip on the selected feature for a time t_{track} . In the herein presented data, residual and non-linear drift contributions were in the order of approx. 4 pm/min along X and Y and approx. 7 pm/min along Z and cause an error in the absolute lateral and vertical tip positioning during the acquisition time t_{acq} of 6 s to a maximum deviation along X (Z) of about 0.4 pm (0.7 pm), respectively. This uncertainty is smaller than the grid spacing and, thus, negligible.

Frequency-shift versus distance $\Delta f(z)$ curves are recorded by first approaching the tip from the tip-to-sample distance z_{ref} , as defined by the Δf setpoint, closer to the surface to z_{min} . The tip is then retracted along Z to a maximum distance z_{max} while sampling the frequency shift Δf data. The retraction (approach) curve is sampled when moving the tip from z_{min} to z_{max} (z_{max} to z_{min}), respectively, and the tip is finally moved back to the reference height z_{ref} . The resulting Z trajectory is depicted in Fig. 2.9(b). The stable point of smallest tip-sample separation z_{min} is highly dependent on the tip configuration and, accordingly, it is chosen carefully for each experiment. Exemplary $\Delta f(z)$ and $F_z(z)$ curves are reproduced in Figs. 2.9(c) and (d).

Additionally, several curves with a z_{max} of around 50 nm need to be recorded. These are joined with each of the p_x $\Delta f(z)$ curves which is necessary to be able to convert the frequency shift to force. Another necessity is the calibration of the amplitude and the determination of the cantilevers spring constant. Details on why this is important and how this is carried out in this work will be given in Section 3.1.2. Ideally, the acquisition of the 50 nm curves, the amplitude calibration and the determination of the spring constant are carried out immediately after the grid measurement has been finished.

The scan protocol [72] requires a large number of parameters to be carefully chosen to optimize the data resolution, the drift compensation accuracy and the signal to noise ratio. A list of parameters that I used for the data in this work is given in Table 2.1.

Usually, the resolution for the different acquisition approaches is highest in their fastest scan direction. This is giving the *layer-by-layer* mode a better lateral and the *curve-by-curve* mode a superior vertical resolution. The data points along the slow

Tab. 2.1.: List of parameters including values for the ZX slice data acquisition.

Parameter	Variable	Value
Grid settings:		
Number of curves along X	p_x	201 - 361
Samples along Z	p_z	1000
Size along X	s_x	3.48 nm - 4.35 nm
Size along Z	s_z	1.13 nm - 1.33 nm
Sampling resolution in X	res_x	12.0 pm - 17.3 nm
Sampling resolution in Z	res_z	approx. 1.2 pm
Atom tracking:		
Dither frequency	f_{dither}	20 Hz
Dither amplitude	A_{dither}	1.5 Å
Tracking time	t_{track}	8 s
Drift comp. update interval	t_{update}	15 min
Data acquisition:		
Time/sample along Z	t_{sample}	3 ms
Data acquisition time	t_{acq}	6 s

scan direction have to be set manually.

To achieve a sufficiently good resolution along the slow scan direction, usually the number of points chosen has to be quite large. This states a considerable problem, as the number of data points considerably affects the data acquisition time. Typical durations for collecting a full 3D force map are up to 24 hours. This results in two difficulties. First, the longer the acquisition time, the higher is the chance for a tip change. Naturally, this poses a problem, as described above, so one always wants to reduce the acquisition time. This problem however can not be circumvented, as often a compromise has to be found between acceptable acquisition time and sufficient resolution. The usually present second obstacle, the thermal drift, is overcome by using the aforementioned atom-tracking system or measuring at low temperatures around 4 K.

Calculation of forces, potential and dissipation

Contents

3.1	Recovery of the vertical force $F_z(z)$	26
3.1.1	Procedure for evaluating the recovery quality	26
3.1.2	General strategy	27
3.1.3	Filtering	31
3.2	Deconvolution of the potential	33
3.3	Calculation of lateral forces	35
3.4	Rescaling of the dissipation	35

When aiming at understanding the atomistic processes on surfaces, the knowledge of the interaction force at the atomic level is crucial. Ways to measure the force field have been described in the preceding Section 2.5, but so far the focus was on the pure data acquisition. After having successfully finished a force field measurement, though, only a frequency shift Δf map is available. For data interpretation F_{ts} is a lot more desirable than Δf . Therefore, ways have to be found to calculate the force from the frequency shift raw data. After all, it is the main purpose of the elaborate acquisition protocol to be able to convert the measured Δf signal to the force F_{ts} . The fact that several different approaches have been published [18, 82, 83] indicates that this is not a straight forward procedure.

This chapter is dedicated to more technical aspects of how I calculated the desired quantities from the raw data for this work. Most importantly, the deconvolution of the Δf data into the vertical force $F_z(z)$ will be given in Section 3.1, including an elaborate discussion of different filter functions and their correct application in order not to falsify the raw data. This will be followed by the computation of the potential which will be described briefly in Section 3.2. The extraction of lateral forces $F_x(z)$ is based on knowing the potential landscape and is therefore quickly described in Section 3.3. Finally, an overview of how to rescale the dissipation raw data into the correct units will be shown in Section 3.4.

3.1 Recovery of the vertical force $F_z(z)$

In an NC-AFM experiment the Δf signal is obtained from a convolution of the sample and the tip. The calculation of the vertical force $F_z(z)$ and, therefore, the potential is in principle based on the inversion of Eq. (2.5). This can be done in several ways, as has been demonstrated in literature. Formulations have been presented, where the solution is iterated until convergence is obtained [82], a matrix of Eq. (2.5) is inverted numerically using quadrature scheme [18] or Eq. (2.5) is inverted analytically using Laplace transformation [83]. The latter two approaches are the most widely used formulas until today, that is why for this work the focus lied on these two solutions.

In the following, the commonly used designations in literature for the two methods shall be adapted; consequently, the method derived by Giessibl to numerically invert a matrix shall be called "matrix method", while the analytical inversion by Sader and Jarvis will be called "Sader-Jarvis method". Both approaches are applicable to the large-amplitude limitation throughout this work. The question will be addressed, which of these methods is best suitable for the data showed herein.

3.1.1 Procedure for evaluating the recovery quality

Both methods show a complex amplitude dependence for the deconvolution. Since the question what formula to use was relevant to many other groups, there has been an elaborate comparison between those formulas in 2012 by Welker *et al.* [84] to exactly address this question. In their work, they have created a force F_{ts} from a Lennard-Jones and a Morse potential, determined the frequency shift Δf from Eq. (2.5) and deconvoluted this Δf back to the force $F_{S/M}$, using both, the Sader-Jarvis and the matrix method for certain amplitudes. To compare the quality of both deconvolution methods, the coefficient of determination (CoD) has been calculated via

$$R^2 = 1 - \frac{\sum_{i=1}^N (F_{S/M,i} - F_{ts,i})^2}{\sum_{i=1}^N (F_{S/M,i} - \overline{F_{S/M}})^2}, \quad (3.1)$$

as a measure for the similarity of the initial, modelled force F_{ts} and the deconvoluted force $F_{S/M}$. R^2 can only have values between 0 and 1 where $R^2 = 1$ means a perfect match of the initial and the calculated data. In Eq. (3.1) $\overline{F_{S/M}}$ denotes the average of the deconvoluted force, while N is the number of data points. This procedure was followed for a range of amplitude from $0.01 \text{ nm} < A < 1 \text{ nm}$. In their study, Welker

et al. have stated that the matrix method yields a slightly better deconvolution quality in the observed amplitude range, although for both methods they have never found $R^2 < 0.995$, which indicates an almost perfect deconvolution quality for both formulas.

To further examine the deconvoluted force, they have determined the deviation of the magnitude of the modelled and deconvoluted force minimum ΔF_{min} and the position Δz_{min} with similar results: both solutions have almost the same accuracy, combined with an overall minimal deviation.

Although they address most of the relevant factors, it still is of limited use for the present thesis, since it only considers small amplitudes, a lot smaller than the amplitudes used here. A further problem that comes up with real data, i.e. data that is not modelled, is noise. The influence of noise is not at all considered in [84].

Throughout the present work, the Sader-Jarvis formalism was used, because based on the analysis by Welker *et al.* this formalism is still expected to yield accurate results with reasonable numerical effort. Additionally, the matrix method is restricted to large amplitudes only, while the Sader-Jarvis algorithm can be used for all amplitudes. This grants a higher flexibility for future work. Furthermore, I carried out similar calculations as in [84] including noise in the relevant amplitude region for the specific setting in this thesis.

3.1.2 General strategy

A general remark shall be made here at this point. When speaking of a frequency shift, a force or a potential as a function of distance this is coined "spectroscopy" in literature. It shall be stressed here that spectroscopy describes a quantity as a function of the energy and not distance and therefore using this term in AFM to describe $\Delta f(z)$, F_z or U_z curves is misleading. However, to avoid confusion with literature the term spectroscopy is used for the distance dependent data presented in this work.

The analytically deduced formula for deconvoluting the frequency shift into vertical force $F_z(z)$ from Sader and Jarvis has the following form [83]:

$$F_{z,ts}(z) = \frac{2k}{f_0} \int_z^\infty \left[\left(1 + \frac{\sqrt{A}}{8\sqrt{\pi(q-z)}} \Delta f(q) \right) - \frac{A^{\frac{3}{2}}}{\sqrt{2(q-z)}} \frac{d(\Delta f(q))}{dq} \right] dq, \quad (3.2)$$

where k is the spring constant of the cantilever, f_0 the eigenfrequency and A the amplitude. It can be seen that this formula is only valid for one specific amplitude, which requires a constant amplitude during a force field measurement. Equation (3.2) integrates the measured frequency shift from a tip-to-sample distance z to infinity. In the experiment the upper bound of integration is replaced by a distance z_{top} . To allow for a proper application of Eq. (3.2), this value z_{top} has to be chosen carefully. At z_{top} the value for Δf must remain zero upon further retraction of the tip, i.e. z_{top} is a distance where there is no tip-sample interaction. This is achieved, for large-amplitude experiments, by a value for z_{top} larger than twice the oscillation amplitude. Since it would result in either much longer acquisition times or a drastically reduced vertical resolution, $\Delta f(z)$ curves are only recorded up to a distance, where no site-specific interaction is apparent. For this work this value is always 1 nm. As described earlier in Section 2.5.2, several so called long-range $\Delta f(z)$ curves are recorded with a z_{top} of around 50 nm subsequent to the grid spectroscopy. Those long-range $\Delta f(z)$ curves are averaged to one curve which is then joined with every of the p_x high-resolution grid data curves. This is accomplished by at first shifting the grid data along the Δf axis so that the 500 outermost points of the grid data fit the long-range curve. This offset of the grid curves is due to thermal drift of the eigenfrequency f_0 . A shift of the $\Delta f(z)$ curves along the Δf axis is, therefore, justified. Furthermore, no assumptions on the sample system were made when following this procedure. As can be seen from simulations, this is a necessary step, since $\Delta f(z)$ data that were not shifted to fit a zero frequency shift at large distances induce an artefact when applying Eq. (3.2). This is pointed out in Fig. 3.1, where I carried out simulations with values different from 0 Hz at z_{top} . An obvious slope of the long-range part of the converted force is immediately visible.

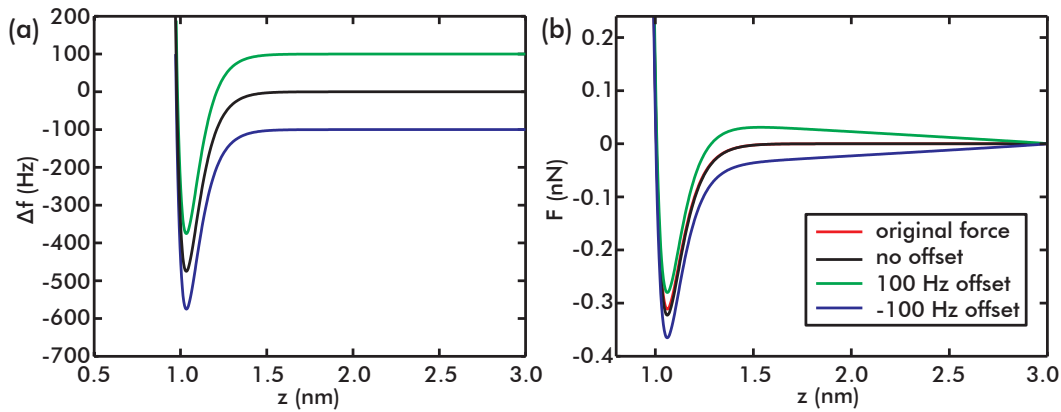


Fig. 3.1.: (a) Simulated $\Delta f(z)$ curves. (b) Recovered force with different offsets at z_{top} in the Δf data.

Another major problem that needed to be tackled is the pole of the integrand in Eq. (3.2) at $q = z$, making the integral improper. Simply deleting that point prior to the calculation introduces a large error. Aware of this problem, Sader and Jarvis have introduced three correction factors to compensate for this obstacle. These

correction factors have been calculated from the first derivation of each of the three summands in Eq. (3.2) and have been given in their released `mathematica` script [85].

Furthermore, it has to be noted that for the employed scan protocol the recorded data are only available as discrete $\Delta f(z_i)$ values. In order to use Eq. (3.2) the way it is written here, the obtained $\Delta f(z)$ curves would have to be described by a continuous interaction function. Consequently, I had to re-write Eq. (3.2) in such a way that it can be used for discrete values. Including the aforementioned correction factors, the employed formula for the calculation of the vertical force now reads

$$F_{z,ts}(z_k) = \frac{2k}{f_0} \left[\Delta f(z_k) \Delta z + \frac{\sqrt{A}}{4\sqrt{\pi}} \Delta f(z_k) \Delta z - \frac{2A^{\frac{3}{2}}}{\sqrt{2}} \frac{\Delta f(z_{k+1}) - \Delta f(z_k)}{\sqrt{\Delta z}} \right] + \frac{2k}{f_0} \sum_{i=k+1}^{N-1} \left[1 + \frac{A^2}{8\sqrt{\pi}(z_i - z_k)} \Delta f(z_i) - \frac{A^{\frac{3}{2}}}{\sqrt{2}(z_i - z_k)} \frac{\Delta f(z_{i+1}) - \Delta f(z_i)}{\Delta z} \right] \Delta z. \quad (3.3)$$

It is $\Delta z = z_{k+1} - z_k$. The three terms in the first square brackets denote the correction factors.

Besides the pure spectroscopic data, several other experimental parameters are necessary to recover the force, namely the resonance frequency f_0 , the oscillation amplitude A and the cantilever spring constant k . The resonance frequency was determined by the PLL prior to the experiment.

The amplitude is calibrated by the constant- γ method described by Simon *et al.* [86]. For determining the amplitude calibration according to this method the excitation amplitude and the frequency shift setpoint are varied in such a way that the normalised frequency shift in Eq. (2.8) is constant for every set of parameters. By keeping the normalised frequency shift constant it is guaranteed that the distance, z , of the tip at the lower turning point of the oscillation and the sample is constant throughout the calibration experiment, as shown in Fig. 3.2. The distance in piezo extension, Δz , can then be used to obtain the difference in the oscillation amplitudes. From this, a scaling factor can be determined to convert the voltage amplitude for the mechanical oscillation into physical amplitude. The amplitude calibration is executed directly after the spectroscopy experiment is finished.

The spring constant is obtained from thermal cantilever noise spectra, which has been discussed in detail by Lübbe *et al.* [88]. This can in principle be done in two ways. One method is described by Cook *et al.*, where the peak of the thermal spectrum is fitted with [89]:

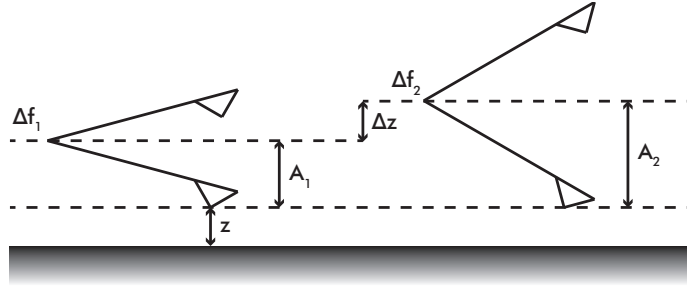


Fig. 3.2.: Scheme of an amplitude calibration. For several sets of frequency shifts Δf the excitation amplitude A is changed in such a way that the normalised frequency shift γ and, thus, the tip sample distance z at the lowest oscillation point is constant. The corresponding piezo extension Δz can then be used to obtain the difference in the oscillation amplitude. Adapted from [87].

$$R(f) = \frac{\frac{2k_B T}{\pi k_0 f_0 Q_0}}{\left(1 - \frac{f^2}{f_0^2}\right)^2 + \left(\frac{f}{f_0 Q_0}\right)^2}. \quad (3.4)$$

Here, k_B is the Boltzmann constant, T the temperature, and k_0 , f_0 and Q_0 the spring constant, eigenfrequency and quality factor of the lever's first eigenmode. Another method described by Hutter *et al.* calculates k via integration of the thermal peak via [90]:

$$k = \frac{k_B T}{P}. \quad (3.5)$$

Here, P is the energy of the resonance peak obtained by integration.

Since both methods are equally applicable to the same thermal spectrum, in this entire work both methods were employed to evaluate the spring constant. Thermal spectra were recorded after the amplitude calibration. It is important to note that for a correct use of this method it is necessary to exclude any excitation but thermal. To ensure this, the cable of the piezo connector needed to be disconnected from the AFM.

It should be noted that up to this point the force data is obtained directly from the raw data. The force conversion and all following calculations were performed in MATLAB (MathWorks Inc; Natick MA, USA).

3.1.3 Filtering

When discussing and interpreting force data, a detailed comparison of different surface sites is highly desirable. Unfortunately, it is very hard to distinguish between subtle site-specific differences if the data is too noisy, so data smoothing has to be considered. This has to be done very carefully, in order to avoid distortion of the data or introduce artefacts. The following section presents considerations, simulations and results as to what filters can be used and how to use them effectively.

The quality of the force conversion is of greatest importance and can be checked by the method introduced by Welker *et al.*, which is excellently qualified for this task. Therefore, the checks on the deconvolution quality that I carried out here are based on this method, including an investigation of the influence of noise. Therefore, a simulated Morse force with parameters best fitting the experimental data, was simulated with random noise added to the calculated Δf data. Several different smoothing parameters were then tested for the now following back conversion step. The most suitable set of parameters could then easily be determined by evaluating R^2 , ΔF_{\min} and Δz_{\min} .

For filtering data, two different filter functions were considered, namely Lanczos differentiators and Savitzky-Golay filters. Lanczos differentiators are used to calculate the derivative in Eq. (3.2), employing a least-squares approximation. Here a function $f(x)$ is approximated by a polynomial near point of interest x^* with the assumption that $f'(x^*)$ is equal to the derivative of the polynomial. As a prerequisite, the input data need to be equally spaced. This requirement is met in the experimentally obtained data. For the calculations the number N_{Lanczos} of (odd) points around x^* were varied.

Savitzky-Golay filters were used to smooth the data after the force recovery. These filters perform a local polynomial regression on a series of equally spaced data points. The smoothed values are obtained from the coefficients of the polynomials. The variables for this kind of filters are the order m_p of the polynomial and the span n_{SG} , in which the regression shall be performed. It should be noted that n_{SG} must always exceed m_p , otherwise the calculation can not be performed. For the smoothing of the data the `smooth` function implemented in MATLAB was used. The following Table 3.1 gives an excerpt of the different parameters considered for the calculations.

The simulations were carried out for every combination of parameters given in Table 3.1. All other values necessary were set in such a way that they fit best with the experimental ones. Those values include the bonding energy E_{bond} , the equilibrium distance σ , the decay length κ , the number of points of one single $\Delta f(z)$ curve and the Δf noise. An overview of all additional parameters is given in Table 3.2.

Tab. 3.1.: Filter parameters used for the smoothing calculations.

Parameter	Variable	Values
Lanczos differentiator		
order	n_{Lanczos}	0, 5
Savitzky-Golay		
degree	m_p	1, 3, (4), 5
span	n_{SG}	5, 11, 17

Tab. 3.2.: Parameters for simulating the Morse force

	E_{bond}	σ	κ	Number of Points	Δf noise
value	$1.5 \times 10^{-19} \text{ J}$	$1.0 \times 10^{-11} \text{ m}$	$0.8 \times 10^{10} \text{ 1/m}$	1000	0.5

The result of these calculations is summarized in Table 3.3 for an amplitude of 17 nm, according to the experiments.

Tab. 3.3.: Left: $n_{\text{Lanczos}} = 0$. Right: $n_{\text{Lanczos}} = 5$. The optimum set of parameters is marked in green.

	R^2	ΔF_{min} pN	Δz_{min} pm	R^2	ΔF_{min} pN	Δz_{min} pm
$m_p = 1, n_{\text{SG}} = 5$	0.6371	160.5	56.5	0.9975	-12.1	5.5
$m_p = 1, n_{\text{SG}} = 11$	0.3166	187.6	-96.6	0.9605	81.6	5.5
$m_p = 1, n_{\text{SG}} = 17$	0.2835	215.1	-96.6	0.8406	186.6	5.5
$m_p = 3, n_{\text{SG}} = 5$	0.9667	10.1	5.5	0.9994	-4.2	5.5
$m_p = 3, n_{\text{SG}} = 11$	0.8819	88.3	56.5	0.9985	-20.1	5.5
$m_p = 3, n_{\text{SG}} = 17$	0.6204	216.2	56.5	0.9975	-30.4	5.5
$m_p = 4, n_{\text{SG}} = 5$	0.9655	27.3	5.5	0.9978	-2.2	5.5
$m_p = 5, n_{\text{SG}} = 11$	0.9651	14.2	5.5	0.9997	-2.7	5.5
$m_p = 5, n_{\text{SG}} = 17$	0.9453	39.7	5.5	0.9993	-12.0	5.5

From Table 3.3 it is immediately visible that the implementation of Lanczos differentiators considerably increases the quality of the back conversion for noisy data. Further simulations, not discussed here, show that the quality decreases again for even higher-order Lanczos differentiators. Despite slightly better values for R^2 and ΔF_{min} for different sets of parameters, I conducted all further force conversions in this work with $n_{\text{Lanczos}} = 5$, $m_p = 3$ and $n_{\text{SG}} = 5$, since this parameter set give good results in all of the examined criteria. Figure 3.3 shows R^2 , ΔF_{min} and Δz_{min} for the whole amplitude range of the simulation for the chosen parameters, including $n_{\text{Lanczos}} = 0$ for comparison. These parameters allow for an overall good quality for the back conversion, without smoothing the data too much. From Fig. 3.3 it is obvious that the quality of the force recovery decreases considerably for amplitudes larger than 20 nm.

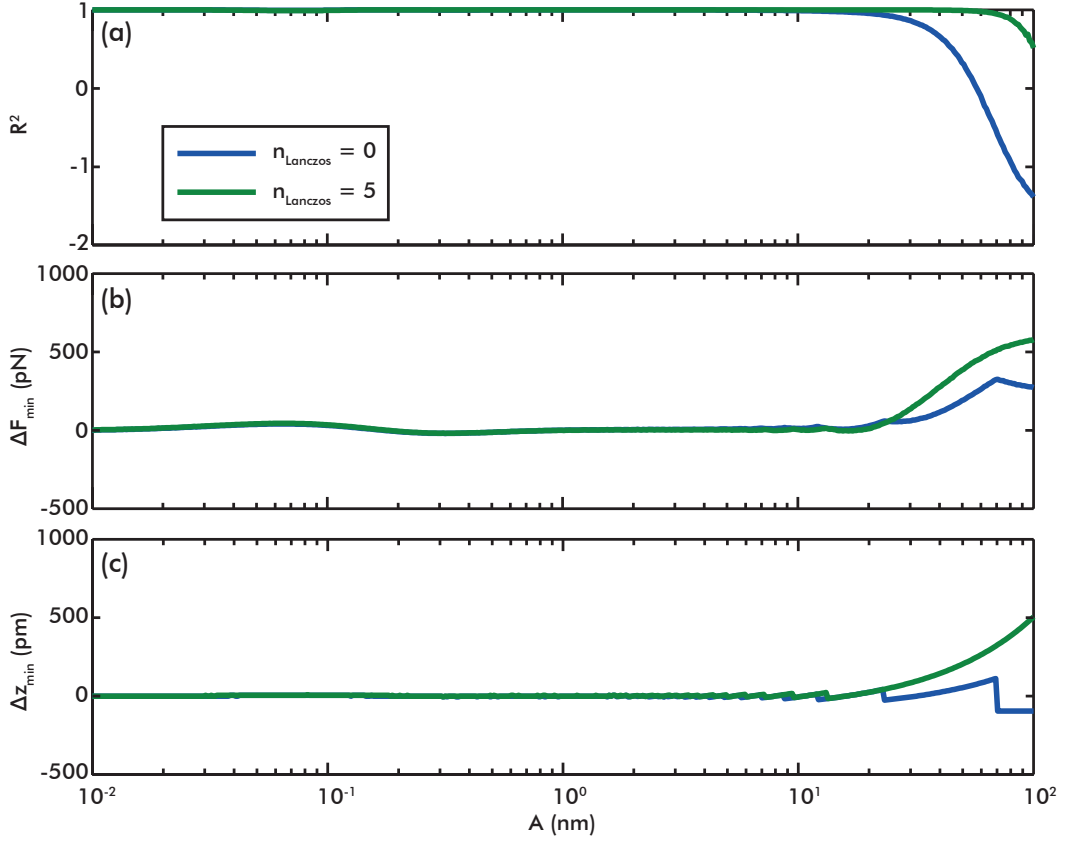


Fig. 3.3.: Comparison of a modelled and the deconvoluted force for $n_{\text{Lanczos}} = 0$ (blue) and $n_{\text{Lanczos}} = 5$ (green). In both cases are $m_p = 3$ and $n_{\text{SG}} = 5$. (a) Deconvolution quality expressed as the coefficient of determination (CoD) R^2 . (b) Deviation of the maximum attractive force ΔF_{min} . (c) Deviation of the position of the force minimum Δz_{min} . The quality check has been performed in an amplitude range from 0.01 nm to 100 nm.

3.2 Deconvolution of the potential

The potential is connected to the force with the relation given in Eq. (2.9), so the same strategy for the deconvolution of the potential has to be used as described before in Section 3.1.2 for the vertical force. The knowledge of the potential landscape is crucial, because it enables the calculation of lateral forces $F_x(z)$ as discussed in Section 3.3.

As for $F_z(z)$, an analytically derived connection between the potential and the frequency shift is given in [83]. This expression is similar to Eq. (3.2) and reads

$$U_{ts}(z) = \frac{2k}{f_0} \int_z^\infty \left((q-z) + \frac{\sqrt{A}}{4} \sqrt{\frac{q-z}{\pi}} + \frac{A^{\frac{3}{2}}}{\sqrt{2(q-z)}} \right) \Delta f(q) dq. \quad (3.6)$$

It is obvious that Eq. (3.6) is an improper integral as well, so the same problem as for Eq. (3.2) also holds true in this case. Thus, the correction factors were determined in the same manner as for $F_z(z)$, as given in [85]. The implemented formula considering the correction factors is the following:

$$U_{z,ts}(z_k) = \frac{2k}{f_0} \left[\Delta f(z_k)(\Delta z)^2 + \frac{\sqrt{A}}{6\sqrt{\pi}} \Delta f(z_k) (\sqrt{\Delta z})^3 + \frac{2A^{\frac{3}{2}}}{\sqrt{2}} \Delta f(z_k) \sqrt{\Delta z} \right] + \frac{2k}{f_0} \sum_{i=k+1}^N \left[(z_i - z_k) + \frac{\sqrt{A}}{4} \sqrt{\frac{z_i - z_k}{\pi}} + \frac{A^{\frac{3}{2}}}{\sqrt{2}(z_i - z_k)} \right] \Delta f(z_i) \Delta z. \quad (3.7)$$

This allows for the calculation of the potential landscape from the raw Δf data. Since Eq. (3.6) contains no differentiation, as is in contrast to Eq. (3.2), the potential data is usually not noisy and does not require the use of Lanczos differentiators or filtering in general. Therefore, an elaborate filtering analysis as described in Section 3.1.3 for $F_z(z)$ is not necessary here and the data obtained from Eq. (3.7) can readily be used.

A comparison of the Δf (blue), raw and smoothed $F_z(z)$ (grey and red, respectively) as well as $U(z)$ (green) data is shown for a single curve at an arbitrary position on the $\text{CaCO}_3(10.4)$ substrate in the following Fig. 3.4. It can be seen that the filtering procedure significantly reduces noise in the force without distorting significant values like F_{\min} or z_{\min} , while the potential is overall smooth even without filtering. Figure 3.4 shows that F_{\min} is around -0.6 nN which at the point of z_{\min} corresponds to an energy difference compared to a distance of no interaction of roughly -1.2 eV.

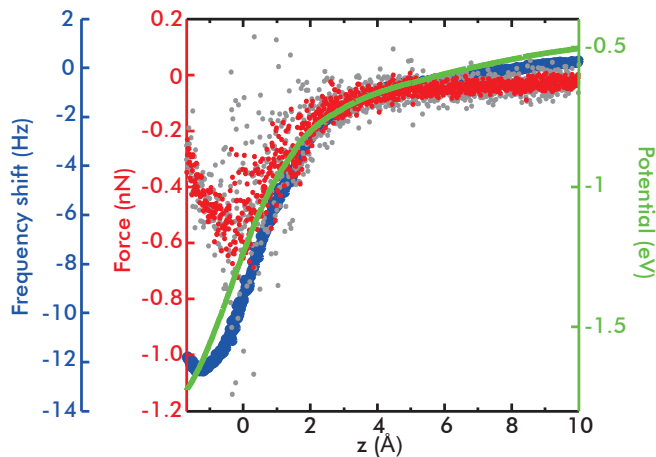


Fig. 3.4.: Comparison of Δf (blue circles), raw and smoothed $F_z(z)$ (grey and red dots, respectively) and $U(z)$ (green solid line) at an arbitrary position on a $\text{CaCO}_3(10.4)$ surface.

3.3 Calculation of lateral forces

Lateral forces $F_x(z)$ are highly interesting for manipulation experiments, because a mechanical manipulation relies on the forces parallel to the surface [91, 92]. Furthermore, $F_x(z)$ does not require a long-range force subtraction as $F_z(z)$ does, because $F_x(z)$ is only sensitive to the short-range force acting in the horizontal direction [93, 94]. When vertical short-range force $F_{z,SR}$ are desired, the onset of lateral force contrast states a valuable information for extracting $F_{z,SR}$, as will be discussed in Chapter 4.

Lateral forces can be accessed in different ways. Pfeiffer *et al.* excite the cantilevers torsional mode to directly and exclusively measure the lateral interaction [95], while Kawai *et al.* use bimodal excitation of the cantilever [94] to measure vertical and lateral forces simultaneously. For all presented ways the cantilever oscillates nearly parallel to the surfaces, so an extraction of lateral forces is justified.

From a frequency shift $\Delta f(x,y,z)$ map it is not only possible to calculate the vertical force $F_z(z)$, but also the lateral force $F_x(z)$ acting parallel to the surface. This is at first counterintuitive, because the data were sampled vertically (see Section 2.5), but since the interaction potential can be calculated independent of the path of the integration of the force field, an extraction of forces parallel to the surface is allowed [69, 70]. While vertical forces $F_z(z)$ are the derivative of the potential with respect to the Z axis, the lateral forces can be obtained in a similar way via

$$F_x = -\frac{\partial U}{\partial x}. \quad (3.8)$$

Equation (2.9) does not specify, in which direction the derivative has to be taken, so it is both applicable for lateral and vertical forces. While $F_z(z)$ is obtained via deconvolution methods, compare Eq. (3.6), $F_x(z)$ has to be derived using the deconvoluted potential data $U(z)$. In general, positive values for $F_x(z)$ describe a force in the same direction as the positive X-axis, while negative values point in the negative X-axis. A zero value for $F_x(z)$ is similar to the equilibrium position of the tip.

3.4 Rescaling of the dissipation

NC-AFM provides the possibility to separate conservative and dissipative interaction. The knowledge of the dissipation allows for a deeper understanding of the measured

data. Although dissipation is not yet fully understood, quite some publications deal with the physical origin of non-conservative forces [96–101].

As was shown in Section 2.1.2 and in Fig. 2.2, the dissipation signal is an output of the amplitude feedback. In the case of non-conservative interaction between tip and sample the cantilever dissipates energy into the sample which causes a lowering of the original excitation amplitude $A_{exc,0}$. The feedback loop has to increase the excitation by a certain value in order to reach $A_{exc,0}$ again. This signal A_{exc} includes the additional excitation and is a direct measure for the dissipated energy. This measurement, based on the strict separation of conservative and dissipative forces, is only allowed if the phase shift between the cantilever movement and excitation signal is 90° .

Non-conservative forces cause a hysteresis in an approach and retract cycle of $F_z(z)$. It is desirable to obtain the dissipation in the units of energy loss per oscillation cycle. Therefore, at first the energy stored in the cantilever has to be known. This is [16]

$$E_{stored} = \frac{1}{2}kA^2. \quad (3.9)$$

The cantilever's dimensionless quality factor, which for UHV is in the order of 30.000, is defined as [16]

$$Q = 2\pi \frac{E_{stored}}{\Delta E_{int}}. \quad (3.10)$$

Combining Eqs. (3.9) and (3.10) gives an expression of the energy dissipated in the cantilever due to internal friction. Far away from the sample this internal energy loss per cycle can be written as

$$\Delta E_{int} = \frac{\pi k A^2}{Q}, \quad (3.11)$$

If additional damping occurs due to the dissipative interaction of the tip with the sample, the energy dissipation per cycle can be written as:

$$\Delta E = \frac{\Gamma}{\Gamma_0} \Delta E_{int} \quad (3.12)$$

The increase of energy loss per cycle due to dissipative tip-to-sample interaction is, therefore, the difference between the dissipation with additional tip-sample interaction and the internal dissipation of the cantilever. It can, thus, be written as [102]:

$$\Delta E_{ts} = \Delta E - \Delta E_{int} \quad (3.13)$$

$$= \frac{\pi k A^2}{Q} \left(\frac{\Gamma}{\Gamma_0} - 1 \right) \quad (3.14)$$

The ratio $\frac{\Gamma}{\Gamma_0}$ is easily accessible, since the amplitude feedback gives these values as a linear scaled voltage and with the recording of a $\Delta f(z)$ curve, $\Gamma(z)$ curves are acquired simultaneously. Thus, the voltage output signal of the amplitude feedback can directly be used for rescaling the raw dissipation data into energy loss per cycle $\frac{eV}{cycle}$. Replacing the dissipation Γ and Γ_0 by the feedback voltage output V_{exc} and $V_{exc,0}$, respectively, Eq. (3.14) can be written as [16, 99, 101, 102]

$$\Delta E_{ts} = \frac{\pi k A^2}{Q} \left(\frac{V_{exc}}{V_{exc,0}} - 1 \right). \quad (3.15)$$

For the rescaling of the dissipation, Eq. (3.15) was implemented into the MATLAB conversion routine. $V_{exc,0}$ is hereby determined by averaging the outermost 400 points of a $\Gamma(z)$ curve, where only internal energy loss of the cantilever is measured. Figure 3.5 shows a $\Gamma(z)$ curve with the raw V_{exc} data in volts on the left ordinate and the rescaled dissipation values in $\frac{eV}{cycle}$ on the right ordinate. The region used for $V_{exc,0}$ is marked with a red bar. As can be seen, the typical energy loss due to dissipative interaction with the $\text{CaCO}_3(10.4)$ surface is around 150 meV/cycle.

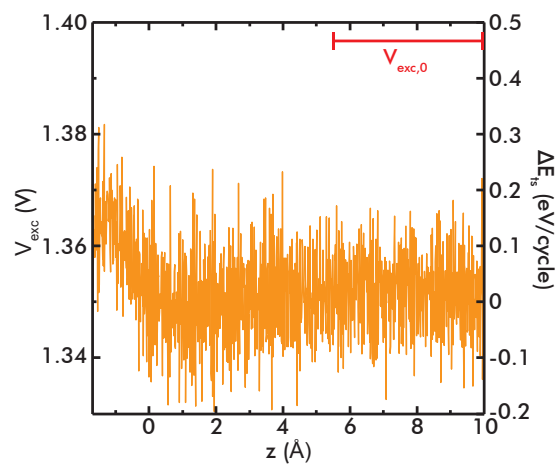


Fig. 3.5.: Dissipation data. The left ordinate gives the raw output of the amplitude feedback, the right ordinate is the rescaled energy loss per cycle. The red bar indicates the area used for $V_{exc,0}$.

Strategy for extracting short-range forces

Contents

4.1	Introduction	40
4.2	Example data	42
4.3	Models	43
4.4	Fit and subtraction strategies	48
4.4.1	Model selection	49
4.4.2	Refinement of the cutoff position	52
4.5	Error analysis	55
4.6	Conclusion	56

NC-AFM features the measurement of forces with highest spatial resolution and sensitivity, resolving forces of the order of pico-Newtons with submolecular resolution. However, the measured total force is a mixture, composed of various interactions. While some interactions such as electrostatic or magnetic forces can be excluded by a careful design of the experiment, the subtraction of van der Waals forces, which mainly originate from London dispersion interactions between the macroscopic tip shank and the bulk sample, remains a challenge.

This chapter concerns about the determination of the inherently present van der Waals forces in total interaction force data from fitting a suitable model, allowing for extraction of the short-range force component. These results were obtained in cooperation with Philipp Rahe and are already published [40]. An introduction will be given in Section 4.1, followed by a presentation of example data from the calcite(10.4) surface in Section 4.2. Several models for fitting the long range van der Waals background are introduced in Section 4.3. The feasibility to fit these models to the experimental data is critically discussed in Section 4.4, where, furthermore, criteria to assess the transition point from pure long-range interaction to mixed short- and long-range forces based on the variance of lateral and vertical force data are introduced. The chapter will be closed with an elaborate error analysis of the successfully obtained short-range force data in Section 4.5 and a short conclusion in Section 4.6.

4.1 Introduction

Generally, the AFM measures the total tip-sample interaction force, which is composed possibly of, e.g., electrostatic, magnetic, van-der-Waals or chemical interactions between one or multiple atoms in the tip and the sample. Depending on the topic of interest, only one or a few of these contributions might be of relevance and strategies to separate the different interactions from the total force become necessary.

As sketched in Fig. 4.1, we understand *site-specific* forces as the interaction between the tip and a specific surface site in a periodic lattice, namely single surface atoms such as the prominent adatom on the Si(111)-(7 × 7) surface [103], different atomic species on the TiO₂(110) substrate [104] or dopant atoms. We distinguish this case from the system of surface-supported molecules, where the contribution of *adsorbate-specific* forces, defined by the exclusive adsorbate-tip interaction, are of interest. In this case, this specific force is clouded by contributions from the underlying substrate. For the latter case, a well-studied molecule is C₆₀, deposited on Si(111)-(7 × 7) [58] or Cu(111) [105] surfaces to name two examples.

Usually, in both cases the relevant forces are known as *short-range* forces, but the approach to extract these might highly differ.

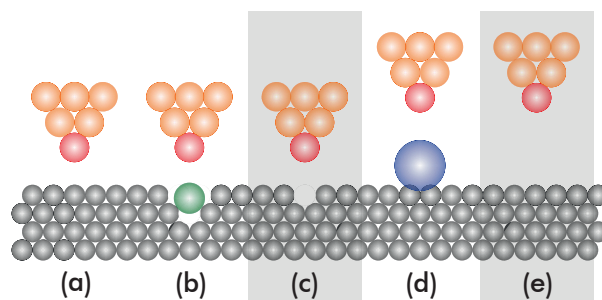


Fig. 4.1.: (a) and (b) depict the case of *site-specific* forces, where the interaction of the tip with one specific lattice site (shaded gray in (a)) or with a specific dopant atom (depicted green in (b)) is investigated. (d) is a scheme of an *adsorbate-specific* interaction, where the force between the tip apex and the adsorbate is the relevant observable. (c) and (e) represent suitable reference positions for a so-called “off”-curve

Some of the interactions listed above can be separated by a careful design of the experiment. Electrostatic forces can be minimized using the Kelvin Probe technique (Refs. [22, 28, 29]) and the magnitude of magnetic forces can be governed by an applied external field and the tip material [106]. In sharp contrast, long-range van-der-Waals forces are ubiquitous and, to our best knowledge, no strategy is known so far to nullify them during a regular AFM experiment.

These van der Waals forces act measurably between the macroscopic part of the tip shank of the cantilever and a widespread part of the investigated sample, clouding the usually short-ranged forces of interest. Consequently, the main motivation in

high-resolution AFM studies is to subtract these background forces F_{vdW} from the total vertical force F_z , ultimately yielding the short-range vertical force $F_{z,\text{SR}}$:

$$F_{z,\text{SR}}(z) = F_z(z) - F_{\text{vdW}}(z). \quad (4.1)$$

Here, we will discuss a generally applicable and reliable method to extract either the *site-specific* or *adsorbate-specific* forces of *short-range* nature from the total interaction force typically measured in AFM force measurements. In particular, we will discuss the reliability of the models described in literature and introduce criteria to determine the transition point between the interaction regimes.

The necessity for the separation of short-range forces from total force data has been realized in few literature studies before. The usage of a reference curve as pioneered by Lantz *et al.* [103] on Si(111)-(7 × 7) surfaces and recently analysed in detail by Sweetman and Stannard [107] can be considered as the most reliable method – although its application is limited to specific sample systems. This method uses an experimental $F_z(z)$ -curve from a reference site (see Fig. 4.1(c) and (e)), which is numerically subtracted from the total force data at the relevant sample site after the experiment. The force curve at the reference site has to exclude any short-range interaction of interest, instead, it must only contain the long-range contribution. For the Si(111)-(7 × 7) surface, the cornerhole has successfully been used as the reference position [103], while in case for adsorbed species, such as C₆₀ on Si(111)-(7 × 7) [58] or single Pt atoms on Pt(111) or Cu atoms on Cu(111) [108], a simple *off-species* curve has served as a well-suited reference.

Despite the robustness of this method, the strategy can only be applied when a well-defined reference position is available. For some sample systems, where no suitable reference position is found, an approach free of assumptions is to compare the site-specific interaction between two positions [52, 109, 110], although the resulting force curves cannot be interpreted as site-specific short-range interactions.

For sample systems, where neither a reference position exists nor the site-difference method is appropriate, a post-processing approach modelling the van der Waals interaction has been followed before [50, 67, 68, 103]. This approach relies on fitting a suitable model to the long-range part of the total interaction force data. Straightforward models using simplified, phenomenological formulae have been pursued [50, 105], while more sophisticated descriptions involving physical parameters for reasonable tip models, though rarely used in the context of short-range force subtraction, have been derived in literature before [32, 39, 111, 112]. The crux of this strategy lies in the fact that the long-range forces are necessarily extrapolated into the short-range regime, an extrapolation highly dependent on the fitted regime

and the chosen model.

Here, we will critically investigate the strategy of fitting and extrapolating the long-range data into the short-range interaction regime. We will use atomically-resolved interaction data from the calcite (10.4) surface to exemplify our strategy. This ionic material does not exhibit a site which could serve as a reference point and, thus, discussing the short-range tip-sample interaction [40] completely relies on a well-working subtraction scheme. We will compare several models for realistic tip geometries and will develop criteria to assess the reliability of the short-range force extraction.

4.2 Example data

We demonstrate our strategy on force field data. Our approach as described in Chapter 2, resulted in dense 2D slices of the atomic-scale interaction data on the calcite $\text{CaCO}_3(10.4)$ surface [72], which will serve as exemplary data throughout this chapter. We compensated for long-range electrostatic forces by applying a suitable tip voltage determined at representative sample positions [28]. This voltage was held fixed during the short-range data acquisition with no modulated voltage applied. We note that tips prepared by Ar^+ -Ion sputtering, as described in Section 2.3, usually yield atomic resolution without the necessity of severe surface-induced tip modification [109]. Especially, we do not follow common STM strategies including hard surface contact, which likely alters the tip apex into a complex and likely unknown geometry.

The vertical and lateral forces $F_z(z)$ and $F_x(z)$ as well as the potential $U(z)$ were calculated as described in Chapter 3. The resulting lateral force data is smoothed afterwards using a 2D average filter over 5 pixel along both axes. The resulting frequency shift Δf , total force F_z and lateral force F_x data are reproduced in Fig. 4.2. We arbitrarily set $z = 0$ nm at the point of closest tip-sample distance.

The routines for fitting the van der Waals interactions are implemented using the function *fit* in MATLAB (MathWorks Inc; Natick MA, USA). We used the Trust-Region algorithm and carefully checked the abort criteria to reliably find the minimum in the parameter space. Further details on the specific fit strategy for each model is given in the next section.

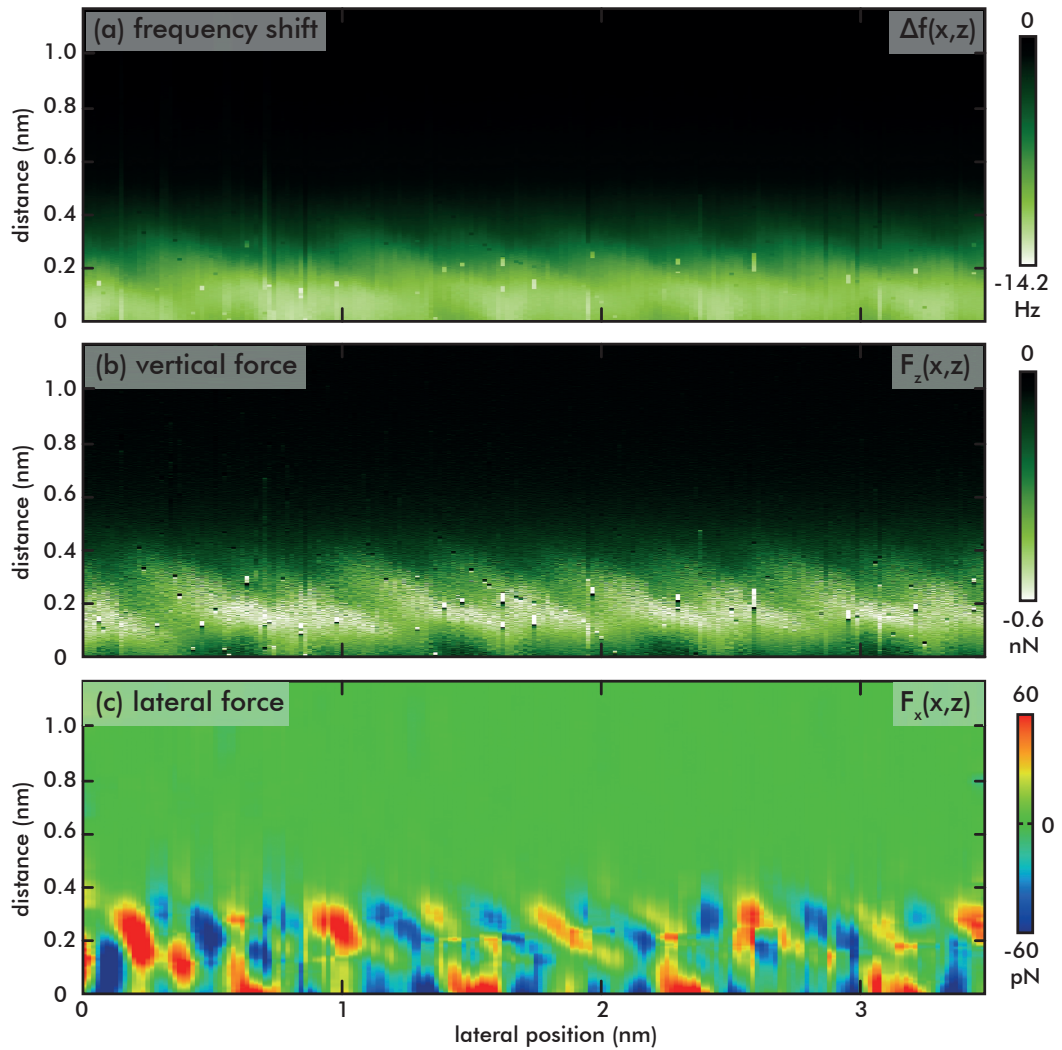


Fig. 4.2.: Experimental data acquired on the calcite(10.4) surface at room temperature [72]. (a) frequency shift $\Delta f(x, z)$, (b) total vertical force $F_z(x, z)$ and (c) lateral force $F_x(x, z)$ data.

4.3 Models

Although the physical origin for the measured total force in an AFM experiment might be multifaceted as discussed before, in a simplified picture under vacuum conditions usually three contributions [111] are prevalent, namely chemical, electrostatic and van der Waals interaction as sketched in Fig. 2.4.

We understand chemical forces as the forces leading to atomic (or even subatomic) resolution, whose origin is the chemical interaction between the foremost tip atoms and nearby sample species. Their simplified description can rely on potentials such as the Lennard-Jones or Morse [113] formulae. More important, however, is the large body of literature nowadays available for a description of the tip-sample interaction for specific sample systems usually analysed by means of ab-initio calculations [67, 114–117]. Experimentally, these are the relevant forces in most high-resolution

NC-AFM experiments that need to be separated from the measured total force. Electrostatic forces originate from an applied tip-sample voltage, different contact potentials of tip and sample materials or from local charges or multipoles [29]. They are of long-range nature and, in contrast to other contributions, can be minimized during the experiment using the Kelvin Probe technique [28]. Consequently, a post experimental correction is usually not necessary and we neglect these forces in the following discussion.

In contrast, long-range van der Waals forces (specifically the contribution from London dispersion interactions that is discussed herein), which we understand as the forces originating from all species framing the macroscopic tip and macroscopic sample, are ubiquitous in AFM experiments and create a site-independent background force. Few approaches for the measurement and extrapolation of long-range forces have been proposed for the case of unavailable off-site reference curve.

First, we review approaches based on phenomenological formulae. Simple mathematical relations aim for modelling the expected electrostatic and van der Waals force laws at a simplified level. Langkat *et al.* [50] have used a power-law of the form

$$F_{lr,1}(z) = \frac{B}{z - z_{\text{off}}} \quad (4.2)$$

to describe the long-range electrostatic and van der Waals interactions acting on a conical tip [19, 118]. Parameter B is a phenomenological fitting parameter with unit of energy, while z_{off} represents a shift of the long-range data with respect to the short-range interaction. Including this shift between the short- and long-range data is a commonly followed approach, fully justified by the fact that the “origins” of both interaction types might be slightly shifted against each other. This fact is usually visualized by a small nanotip of height z_{off} attached to the macroscopic tip.

Hauptmann *et al.* [105] followed a similar strategy by using another phenomenological formula for the approximation of the long-range van der Waals force

$$F_{lr,2}(z) = a(z_{\text{off}} - z)^b. \quad (4.3)$$

where two fitting parameters a and b describe the interaction and z_{off} again the shift of the data. a has the unit of $\frac{N}{m^b}$ and b is a unitless number.

More realistic models describing the van der Waals interaction in AFM experiments are based on calculating the force from a Hamaker integration for different tip models positioned above an infinite sample plane. In contrast to the phenomenological formulae cited before, these models involve physically justified parameters that allow for assessing the plausability of each model. In principle, it is especially possible to

determine parameters with complementary methods. The force equations are fitted to the experimental data by using the physical parameters as fitting variables. We will critically discuss each of the following models and quantify their fit quality as an example for atomic-scale data acquired on the calcite(10.4) surface.

Due to the small tip-sample distance regime, we herein only discuss formulae for the non-retarded case by neglecting retardation effects. This is justified by the fact that usually retardation only plays a major role for tip-sample distances larger than 10 nm [34–37].

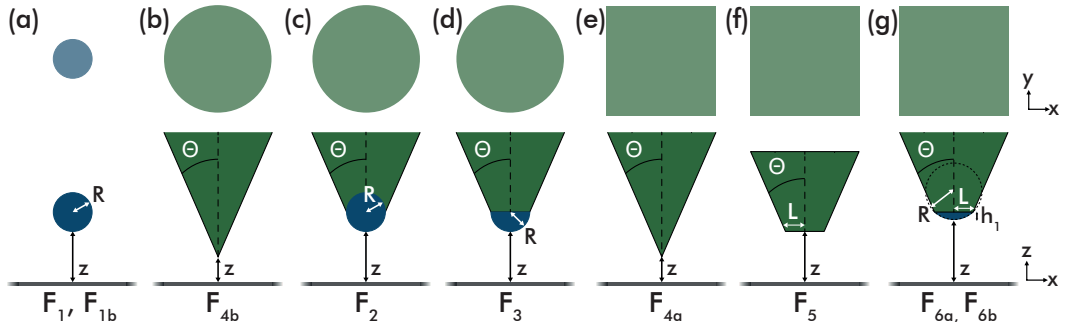


Fig. 4.3.: Schemes of typical tip models used for van der Waals interactions in literature including references to each formula reviewed within this manuscript.

Geometrical schemes for various tip models considered herein are depicted in Fig. 4.3. Argento and French [32] have used a simple sphere-plate geometry (see Fig. 4.3(a)) resulting in the force law [31]

$$F_1(z; H, R, z_{\text{off}}) = - \frac{2HR^3}{3\hat{z}^2(\hat{z} + 2R)^2} \quad (4.4)$$

where H is the Hamaker constant, R is the sphere radius and $\hat{z} = z + z_{\text{off}}$ is the distance between the infinite plane and the lowest point of the tip sphere shifted by the offset z_{off} . The latter variable represents the shift between short- and long-range interaction as discussed before. This force law contains three fit parameters (H, R, z_{off}) , which we found to be dependent on each other when Eq. (4.4) is fitted to our experimental data. We give a detailed discussion of the fit characteristics for this and all other formulae in appendix A. Fixing one parameter and fitting Eq. (4.4) to our data, however, does not result in reasonable physical values for the free parameters. Although this model force F_1 seems to be unsuitable for our data, it has been used successfully to model the long-range interaction on the Si(111) – (7 × 7) cornerhole [65, 67, 103].

For $z \ll R$, Eq. (4.4) reduces to [32]

$$F_{1b}(z; H, R, z_{\text{off}}) = - \frac{HR}{6\hat{z}^2}. \quad (4.5)$$

The fit parameters (H, R) are clearly dependent, we will arbitrarily fix R in the following. This simple model, however, might describe the interaction only unsatisfactorily as the tip shank is not considered.

More complex models include cones or pyramids for describing the tip shank. Gugisberg *et al.* [111] have presented a formula for a full sphere attached to a cone with half-opening angle θ as depicted in Fig. 4.3(c), the overlap between sphere and tip cone has been handled by a correction term. The resulting force reads:

$$F_2(z; H, R, \theta, z_{\text{off}}) = -\frac{H}{6} \left(\frac{R}{\hat{z}^2} + \frac{\tan(\theta)^2}{\hat{z} + R(1 - \sin(\theta))} - \frac{R(1 - \sin(\theta))}{\hat{z}(\hat{z} + R(1 - \sin(\theta)))} \right) \quad (4.6)$$

where θ is the half-opening angle of the tip. The force law in Eq. (4.6) has four fit parameters $(H, R, \theta, z_{\text{off}})$, which we found to be dependent on each other. This fact is in agreement with an earlier finding by Hoffmann *et al.* [119]. From our analysis (see appendix A), we find reliable fits when setting R to fixed values. Eq. (4.6) has been used to describe the long-range interaction in atomic-resolution studies on KBr(001) surfaces [119, 120].

Argento and French [32] have extended their simple model by introducing a cone with half-opening angle θ on-top of a half-sphere as shown in Fig. 4.3(d):

$$F_3(z; H, R, \theta, z_{\text{off}}) = -\frac{HR^2(\sin(\theta) - 1)((R - \hat{z})\sin(\theta) - R - \hat{z})}{6\hat{z}^2(R + \hat{z} - R\sin(\theta))^2} - \frac{H \tan(\theta)((\hat{z} + R)\sin(\theta) + R\cos(2\theta))}{6\cos(\theta)(\hat{z} + R - R\sin(\theta))^2} \quad (4.7)$$

The four fit parameters $(H, R, \theta, z_{\text{off}})$ are dependent on each other. Based on our analysis in appendix A, we found that setting R to a fixed value is a robust approach for yielding a reasonable fit quality using Eq. (4.7).

The geometry of etched silicon tips often follows a pyramidal then a cylindrical cone. Zanette *et al.* [39] have derived several formulae using pyramidal tip shanks. First, they described the tip by a non-truncated pyramid with half-opening angle θ , having a sharp apex and of infinite length, see Fig. 4.3(e). The force law

$$F_{4a}(z; H, \theta, z_{\text{off}}) = -\frac{2H \tan(\theta)^2}{3\pi\hat{z}} \quad (4.8)$$

with three fit parameters $(H, \theta, z_{\text{off}})$ has been derived to describe this interaction. H and θ are clearly dependent; we will fix H to reasonable values herein.

A related formula has been found by Argento and French [32] for a sharp, infinite cone as depicted in Fig. 4.3(b)

$$F_{4b}(z; H, \theta, z_{\text{off}}) = -\frac{H \tan(\theta)^2}{6\hat{z}}. \quad (4.9)$$

As in Eq. (4.8), H and θ are clearly dependent; herein we set H to a fixed value. Zanette *et al.* [39] have extended their model described in Eq. (4.8) by truncating the pyramid forming a flat apex of half-side length L , see Fig. 4.3(f). The resulting force reads

$$F_5(z; H, L, \theta, z_{\text{off}}) = -\frac{2HL^2}{3\pi\hat{z}^3} \cdot \left(1 + \tan(\theta)\frac{\hat{z}}{L} + \tan(\theta)^2\frac{\hat{z}^2}{L^2} \right) \quad (4.10)$$

with four fit parameters $(H, L, \theta, z_{\text{off}})$. We found a dependency between these parameters (see appendix A) and reliable fits are achieved when either fixing H , L or θ . In the following, we will choose L fixed.

As the restriction to a flat apex might be unrealistic for the cases present in AFM experiments, they have furthermore expanded this model by terminating the flat pyramid with a spherical cap of height h_1 and full-sphere radius R (see Fig. 4.3(g)):

$$F_{6a}(z; H, R, \theta, h_1, L, z_{\text{off}}) = -\frac{H}{6} \cdot \left(\frac{h_1^2(3R\hat{z} + (R - \hat{z})h_1)}{\hat{z}^2(\hat{z} + h_1)^3} + \frac{L^2}{(\hat{z} + h_1)^3} + \frac{4\tan(\theta)(L + \tan(\theta)(\hat{z} + h_1))}{\pi(\hat{z} + h_1)^2} \right). \quad (4.11)$$

By closely inspecting the geometry we note the relation $L = \sqrt{R^2 - (R - h_1)^2} = \sqrt{2h_1R - h_1^2}$ (for $2R > h_1$). This allows for substituting L with parameters R and h_1 and, thus, removing one parameter resulting in the force law

$$F_{6b}(z; H, R, \theta, h_1, z_{\text{off}}) = -\frac{H}{6} \cdot \left(\frac{h_1^2(3R\hat{z} + (R - \hat{z})h_1)}{\hat{z}^2(\hat{z} + h_1)^3} + \frac{R^2 - (R - h_1)^2}{(\hat{z} + h_1)^3} + \frac{4\tan(\theta)(\sqrt{R^2 - (R - h_1)^2} + \tan(\theta)(\hat{z} + h_1))}{\pi(\hat{z} + h_1)^2} \right) \quad (4.12)$$

with fit parameters $(H, R, \theta, h_1, z_{\text{off}})$. These parameters are still not independent from each other and we found reasonable fits when fixing R (see appendix A). None of these models include assumptions or bear restrictions about the materials of tip or sample. Therefore, the formulae F_1 to F_6 are expected to remain valid on any metallic, semiconducting or insulating surface.

We show the averaged total force $\overline{F_z}$ data acquired experimentally on the calcite(10.4) surface (see Fig. 4.2, Ref. [72]), where the averaging is conducted over all lateral positions. Additionally, we give an overview over all discussed force laws using parameters describing a typical tip in Fig. 4.4

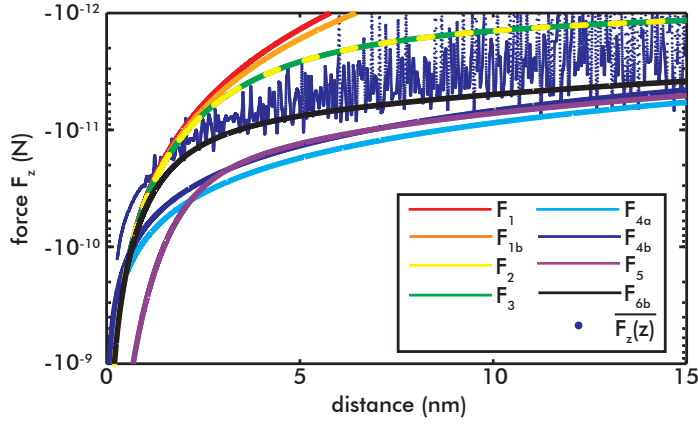


Fig. 4.4.: Plots of all models described by Eq. (4.4) to Eq. (4.12), using parameters $H = 1 \times 10^{-20}$ J, $R = 25$ nm, $\Theta = 30^\circ$, $h_1 = 4.3$ nm and $L = 14$ nm. Experimentally obtained data are included, representing the mean curve $\overline{F_z}(z)$ resulting from averaging all lateral positions in the dataset presented in Fig. 4.2.

4.4 Fit and subtraction strategies

None of the van der Waals interaction formulae are fitted to the full z range of the total force interaction data as inherently none of the formulae model the short-range interaction regime. Instead, a cutoff position z_{cut} , which defines the transition from virtually pure long-range interaction to the combined short- and long-range forces in the experimental data, is chosen and the force laws are fitted from the largest tip-sample distance z_{max} of the data up to this position z_{cut} along the z axis. The determination of this cutoff position is a delicate task as it should be chosen as close as possible to the onset of short-range interaction to increase the fit accuracy, while at the same time it should not lie within the short-range interaction regime.

Consequently, modelling the van der Waals interaction not only requires the determination of the model-specific parameters, but also requires the identification of the cutoff position z_{cut} .

We use the total vertical force data $\overline{F_z}$ averaged over all lateral positions as exemplary experimental data. The van-der-Waals interaction is by definition site-unspecific, consequently, we refrain from fitting and subtracting the background at every lateral position individually.

In principle, some of the parameters such as the tip radius or tip opening angle could be determined by complimentary methods and it might be plausible to derive the Hamaker constants for each specific tip-sample system from literature values. To deliver the general case, however, we herein model the tip without complimentary determination of parameters. Furthermore, by analysing the dependency between the fit parameters for each force law separately in appendix A, we find that fixing a specific parameter usually changes the values of the other parameters, but does not significantly change the resulting curve. Although we, consequently, abstain from the aim to precisely determine the full tip geometry, we nevertheless determine the

fit parameters to eliminate models where the parameters are significantly different from reasonable values.

We also note that in this light, the applicability of phenomenological formulae is challenging, since a reliable criterion is needed to assess the physical justification of these models.

The strategy for a reliable determination of the long-range van der Waals forces based on the above reviewed models is split into three steps: First, we identify the force law that closely represents the experimental force data, especially the herewith described geometry of the used tip. Second, physically meaningful parameters including the offset shift z_{off} should be found from the fit, justifying the applicability of the chosen model. Models with clearly unrealistic parameters will be set aside. Third, the cutoff position z_{cut} is justified using three independent criteria.

4.4.1 Model selection

In the first step, we investigate the suitability of representing the experimentally measured van der Waals interaction for each model by fitting the respective force law to the experimental data. We evaluate the quality of the regression by evaluating the mean squared error (MSE) defined by

$$\text{MSE} = \sqrt{\frac{1}{\text{max} - \text{cut}} \sum_{z_i = z_{\text{cut}}}^{z_{\text{max}}} \left(\overline{F_z}(z_i) - F_{\text{fit}}(z_i) \right)^2} \quad (4.13)$$

where $\overline{F_z}(z_i)$ is the mean experimental vertical force at height z_i and $F_{\text{fit}}(z_i)$ is the corresponding force resulting from the fit. N denotes the number of points along z . MSE has the unit of force and smaller values identify higher quality fits. The following analysis uses experimental reference data from the calcite(10.4) surface. The mean curve $\overline{F_z}(z)$ results from averaging the data over all lateral positions of the slice reproduced in Fig. 4.2(b).

The results of fitting each force law are compiled in Figs. 4.5 and 4.6. Figure 4.5 presents the calculated MSE for each model¹ described above, evaluated with respect to the cutoff position z_{cut} . For evaluating the fit and calculating the MSE, z_{cut} limits the data range along the z -direction, namely to the subset described by the spatial range $[z_{\text{cut}}, z_{\text{max}}]$ of the experimental data. The cutoff position is chosen from the MSE data either as the minimum of MSE closest to the short-range interaction or

¹In our fit procedure, we fixed for the following models the listed parameters for reasons discussed before: $F_1, F_{1b}, F_2, F_3, F_{6b}$: $R = 25 \text{ nm}$; F_{4a}, F_{4b} : $H = 1 \times 10^{-20} \text{ J}$, F_5 : $L = 5 \text{ nm}$.

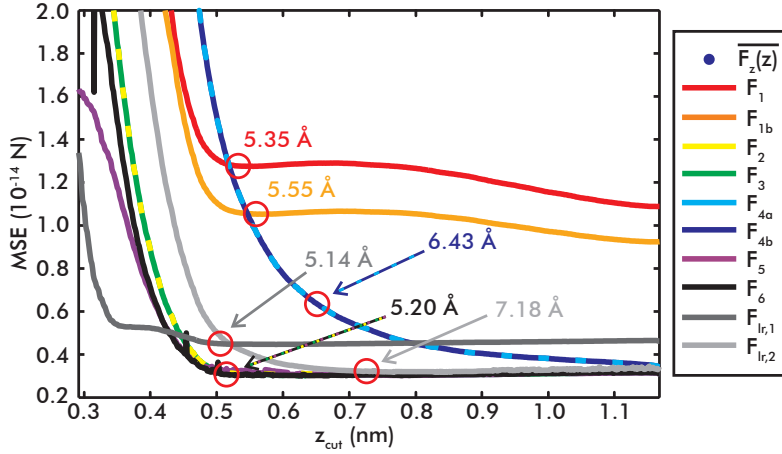


Fig. 4.5.: Fit quality MSE vs. z_{cut} . The cutoff positions used for Table 4.1 are marked. An arbitrary cutoff of $z_{\text{cut}} = 6.43 \text{ \AA}$ is used for F_{4a} and F_{4b} .

the onset of strong deviation in the MSE if no clear minimum is observed. As none of the force models introduced before describe short-range interactions, we expect a clear deviation between model and experimental data when short-range interactions contribute. We will refine the obtained values for z_{cut} in the following section based on two independent criteria.

Clear differences of the fit quality are observed for the different van der Waals models fitted to our data. Based on the smallest values of the MSE, we find in our case overall the best fit quality from using force laws F_2 , F_3 , F_5 and F_{6b} with a common cutoff position at $z_{\text{cut}} = 5.20 \text{ \AA}$. For all other models besides F_{4a} and F_{4b} , the best fits are found nearby $z_{\text{cut}} \sim 6.4 \text{ \AA}$, but the fit quality is clearly reduced. This finding is not surprising, as the force laws F_2 , F_3 , F_5 and F_{6b} cover the most realistic description of the tip geometry while the other force laws F_1 , F_{1b} , F_{4a} and F_{4b} are expected to oversimplify the interaction due to their idealized tip geometries. Clearly, F_{4a} and F_{4b} do not represent realistic models. We explain this straightforward by the fact that the tips in the experiment are expected to be much blunter.

Figure 4.6(a) depicts the experimental mean $F_z(z)$ -curve (blue dots) and the force curves resulting from the fits (solid lines) using the optimum cutoff position for each force model. The qualitative behaviour of the resulting curves from force laws F_2 , F_3 , F_5 and F_{6b} is similar, but we observe a clear deviation between experimental data and the resulting fit curves using models F_{4b} and F_{4a} and especially F_1 and F_{1b} , which is in agreement with the large MSE shown in Fig. 4.5. We will quantify the errors arising from an unfortunate model selection in Section 4.5.

As a second criterion to assess the resulting fit quality, we investigate the resulting physical parameters for the optimum cutoff position as listed in Table 4.1. For the herein used silicon cantilever on a $\text{CaCO}_3(10.4)$ surface, we expect reasonable Hamaker constants in the order of $H \approx 1 - 10 \times 10^{-20} \text{ J}$ (Refs. [121, 122]), tip

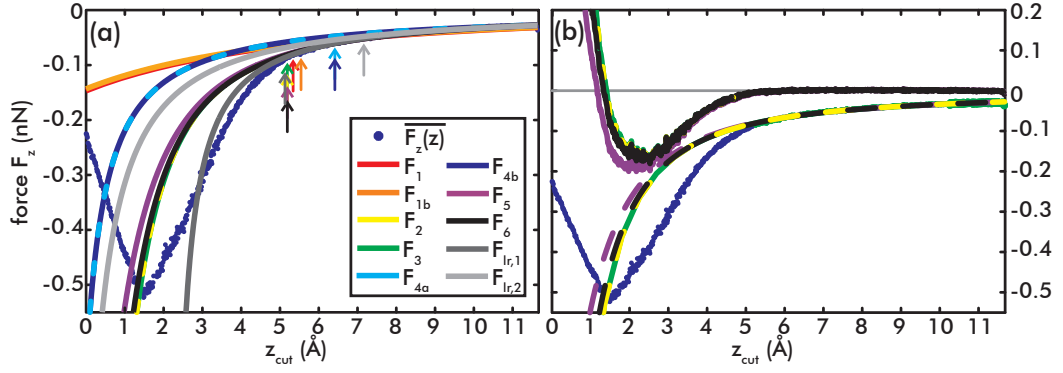


Fig. 4.6.: (a) Resulting van der Waals force curves for each model fitted to the mean force \overline{F}_z (blue dots) and extrapolated into the short-range regime. The cutoff for the best fit for each function is indicated by an arrow in the respective colour. (b) Resulting van der Waals forces (dashed lines) and short-range forces $F_{z,SR}$ (solid lines) for models F_2 , F_3 , F_5 and F_{6b} . The same colour code is used in both panels.

Tab. 4.1.: Resulting parameters for all model fits, using the optimum cutoff positions (or $z_{cut} = 6.41 \text{ \AA}$ in case of F_{4a} , F_{4b}).

model	z_{cut}	MSE 10^{-14} N	z_{off}	fixed parameter	fit parameters
F_1	5.35 \AA	1.276	1.06 nm	$R_{fix} = 25 \text{ nm}$	$H = 4.14 \times 10^{-20} \text{ J}$
F_{1b}	5.55 \AA	1.053	1.03 nm	$R_{fix} = 25 \text{ nm}$	$H = 3.64 \times 10^{-20} \text{ J}$
F_2	5.20 \AA	0.314	0.06 nm	$R_{fix} = 25 \text{ nm}$	$H = 0.44 \times 10^{-20} \text{ J}$ $\theta = 80.3^\circ$
F_3	5.20 \AA	0.313	0.06 nm	$R_{fix} = 25 \text{ nm}$	$H = 0.44 \times 10^{-20} \text{ J}$ $\theta = 80.3^\circ$
F_{4a}	6.43 \AA (set)	0.928	0.05 nm	$H_{fix} = 1 \times 10^{-20} \text{ J}$	$\theta = 75.8^\circ$
F_{4b}	6.43 \AA (set)	0.928	0.05 nm	$H_{fix} = 1 \times 10^{-20} \text{ J}$	$\theta = 77.3^\circ$
F_5	5.20 \AA	0.325	0.18 nm	$L_{fix} = 5 \text{ nm}$	$H = 0.13 \times 10^{-20} \text{ J}$ $\theta = 84.0^\circ$
F_{6b}	5.20 \AA	0.304	0.09 nm	$R_{fix} = 25 \text{ nm}$	$H = 0.56 \times 10^{-20} \text{ J}$ $\theta = 77.8^\circ$ $L = 8.04 \text{ nm}$ $h_1 = 1.30 \text{ nm}$
$F_{lr,1}$	5.14 \AA	0.450	0.21 nm		$B = -0.03 \text{ nJ}$
$F_{lr,2}$	7.18 \AA	0.322	0.05 nm		$a = -0.04 \text{ N/m}^{-1.16}$ $b = -1.16$

radii below 100 nm, opening angles θ below 90° and, accordingly, $L < 100 \text{ nm}$ and $h_1 < 100 \text{ nm}$. For metallic or semiconducting surfaces, literature predicts larger values for the Hamaker constant [123].

Although most parameters listed in Table 4.1 are within these expected regimes, we observe Hamaker constants smaller ² and tip opening angles θ larger than anticipated for most formulae besides F_1 and F_{1b} . However, this finding can be explained by the dependence between H , θ and the fixed parameter tip radius R . Still, we do not consider models F_1 and F_{1b} in the following due to their reduced MSE. The only free parameter for F_{4a} and F_{4b} is the angle θ , yielding reasonable values from the fit by fixing the Hamaker constant to $H = 1 \times 10^{-20}$ J. Still, we reject this model for our experimental data due to the clearly reduced fit quality.

The phenomenological formulae $F_{lr,1}$ and $F_{lr,2}$ lack a physical interpretation of their free parameters, thus, their justification on basis of the resulting parameters is difficult. Here, we can safely reject their applicability due to their reduced fit quality. We note additionally that the cutoff position z_{cut} following from determining the minimum in the MSE (see Fig. 4.5) for $F_{lr,2}$ leads to results in contradiction to the independent criteria discussed in the next section.

To conclude, we find that the van der Waals models described by F_2 , F_3 , F_5 and F_{6b} yield the smallest deviation from the experimental data and the fits yield plausible physical parameters. The fact that the geometrical models for these force laws are not substantially different explains the similarity of the resulting parameters. As the herein used silicon tips are etched in a pyramidal fashion rather than a symmetrical cone, we account the force model F_{6b} to have wider applicability and focus on this force law in the following discussion. We show examples of the resulting short-range forces from subtracting the respective model data from the total force interaction data in Fig. 4.6(b). The resulting curves are identical within reasonable bounds; the remaining errors in the force zero and minimum position will be quantified in Section 4.5.

4.4.2 Refinement of the cutoff position

We refine the selection of z_{cut} by evaluating the onset of site-specific interactions in the lateral and vertical forces.

Figure 4.7(b) presents the difference force $\Delta F_z(z) = F_z(x_j, z) - \overline{F_z}(z)$ between vertical force F_z curves at each lateral position x_j and the mean $\overline{F_z}$ force curve using the data reproduced in Fig. 4.7(a). The curve from every lateral position is identical within the noise limit in the long-range regime ($z > 0.5$ nm) while, in contrast, a significant broadening is observed for small tip-sample distances.

We calculate the standard deviation $\sigma_z(z)$ at height z of the total force data $F_z(x, z)$ from the average curve in the vertical forces $\overline{F_z}(z)$ for each lateral position x_j from

²For calcite-Si or calcite-SiO₂ systems, Hamaker constants around 10×10^{-20} J can be derived from literature [121, 122].

$$\sigma_z(z) = \sqrt{\frac{1}{M-1} \sum_{j=1}^M (F_z(x_j, z) - \overline{F_z}(z))^2} \quad (4.14)$$

and determine the onset of interaction from the onset of increasing values in $\sigma_z(z)$.

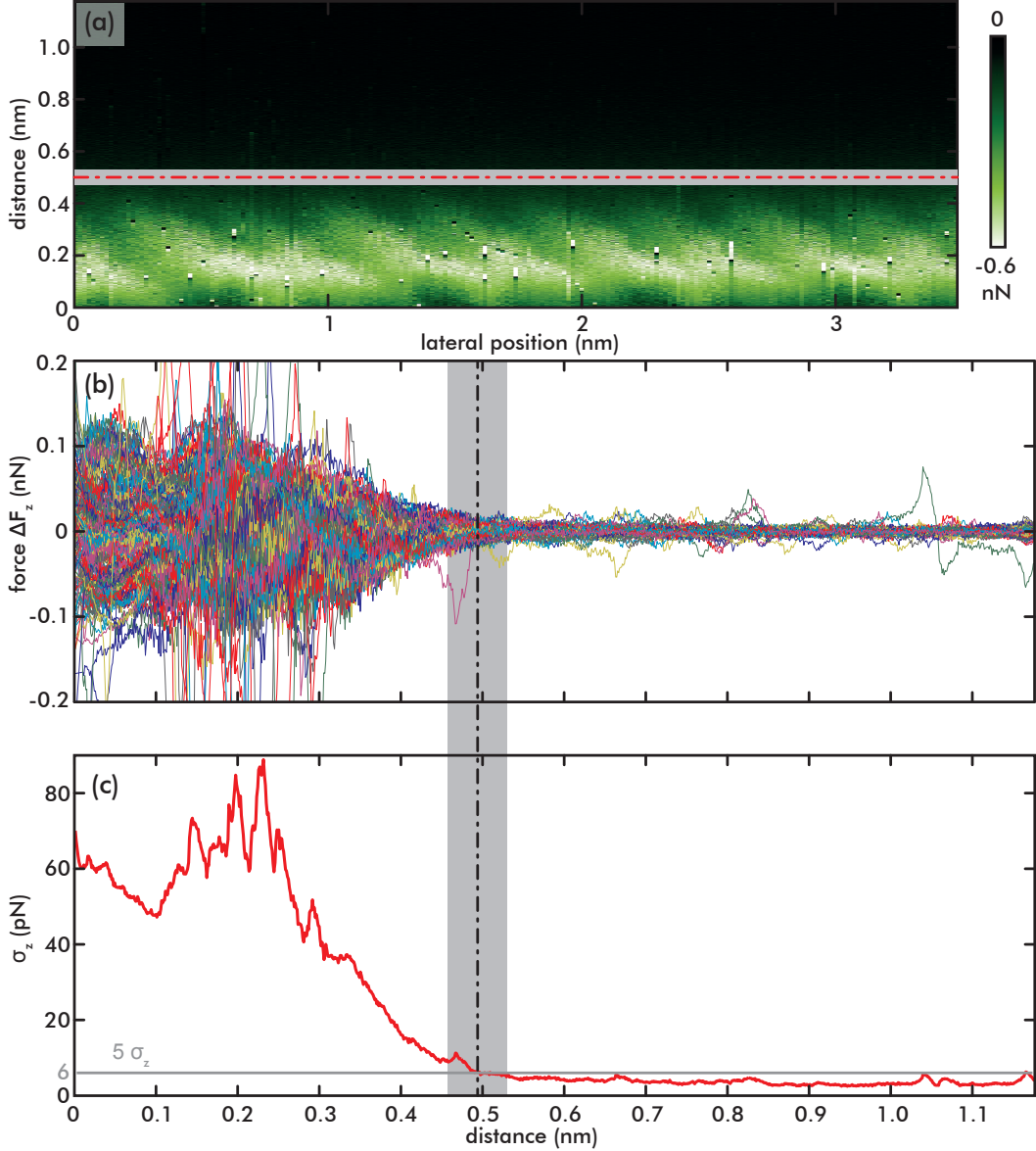


Fig. 4.7.: (a) Total vertical force F_z data. (b) $\Delta F = F_z - \overline{F_z}$ for each lateral position within the dataset. A clear broadening from the long-range noise-limited zero is indicated by a vertical dash-dotted black line. (c) Deviation σ_z of the data from the mean $\overline{F_z}$ curve at each tip-sample distance z . The gray line indicates a deviation of $5\sigma(\sigma_z)$. In agreement with panel (b), the onset of short-range interaction forces is found at $z_{\text{cut}} = (4.9 \pm 0.2) \text{ \AA}$. The dash-dotted line (red in panel (a)) indicates the cutoff, the gray shaded area gives the uncertainty.

The standard deviation $\sigma_z(z)$ is presented in Fig. 4.7(c), where we clearly find the onset of site-specific interactions at $z_{\text{cut}} = (4.9 \pm 0.2) \text{ \AA}$. This position corresponds to the $5\sigma(\sigma_z)$ position of the variance in the long-range part.

In sharp contrast to the vertical forces, the lateral forces are generally assumed to be undisturbed by long-range force interactions [94]. Consequently, we use the onset of lateral force contrast as a third criterion to refine our identification of the cutoff position z_{cut} . Especially, we understand the onset of lateral forces as the lower limit (i.e. closest point) for the onset of short-range interactions and, thus, a lower limit for the cutoff position z_{cut} .

In full analogy to the vertical force analysis, we present in Fig. 4.8(b) the lateral forces F_x at each position x_j and calculate in Fig. 4.8(c) the standard deviation $\sigma_x(z)$ extracted from the lateral force data (see Fig. 4.8(a)) from the equation

$$\sigma_x(z) = \sqrt{\frac{1}{M-1} \sum_{j=1}^M \left(F_x(x_j, z) - \overline{F_x(z)} \right)^2}. \quad (4.15)$$

By using the similar criterion of the $5\sigma(\sigma_x)$ position, we find the onset of lateral forces at $z_{\text{cut}} \sim (5.8 \pm 0.2) \text{ \AA}$. This value is located at a tip-sample distance of about 1 \AA larger than the positions determined before. Although the $5\sigma(\sigma_x)$ position criterion is chosen comparable conservative, this finding notably illustrates the challenge to define z_{cut} .

To conclude, we find cutoff positions of $z_{\text{cut}} = 5.2 \text{ \AA}$ (MSE criterion), $z_{\text{cut}} = (4.9 \pm 0.2) \text{ \AA}$ (σ_z criterion) and $z_{\text{cut}} = (5.8 \pm 0.2) \text{ \AA}$ (σ_x criterion).

Figure 4.9 presents the data for the van der Waals curves and resulting short-range forces using these three cutoff positions for model F_{6b} . The spread of the cutoff positions lead to uncertainties of the force minimum and zero position as well as the force minimum value, which we conservatively determine to $z_{\text{min}} = (2.4 \pm 0.3) \text{ \AA}$, $z_{\text{zero}} = (1.4 \pm 0.4) \text{ \AA}$ and $F_{\text{min}} = (-160 \pm 61) \text{ pN}$, respectively, using the uncertainties from the z_{cut} determination.

All positions fall within a z -range of about 1 \AA . We explain the closer distance of the MSE and σ_z criteria-based cutoff positions by the fact that the onset of site-specific short-range interactions might be hardly distinguishable from the site-unspecific long-range part and, thus, cannot be identified from the MSE and σ_z criteria alone. Consequently, our analysis suggests the usage of the σ_x criterion as the cutoff position.

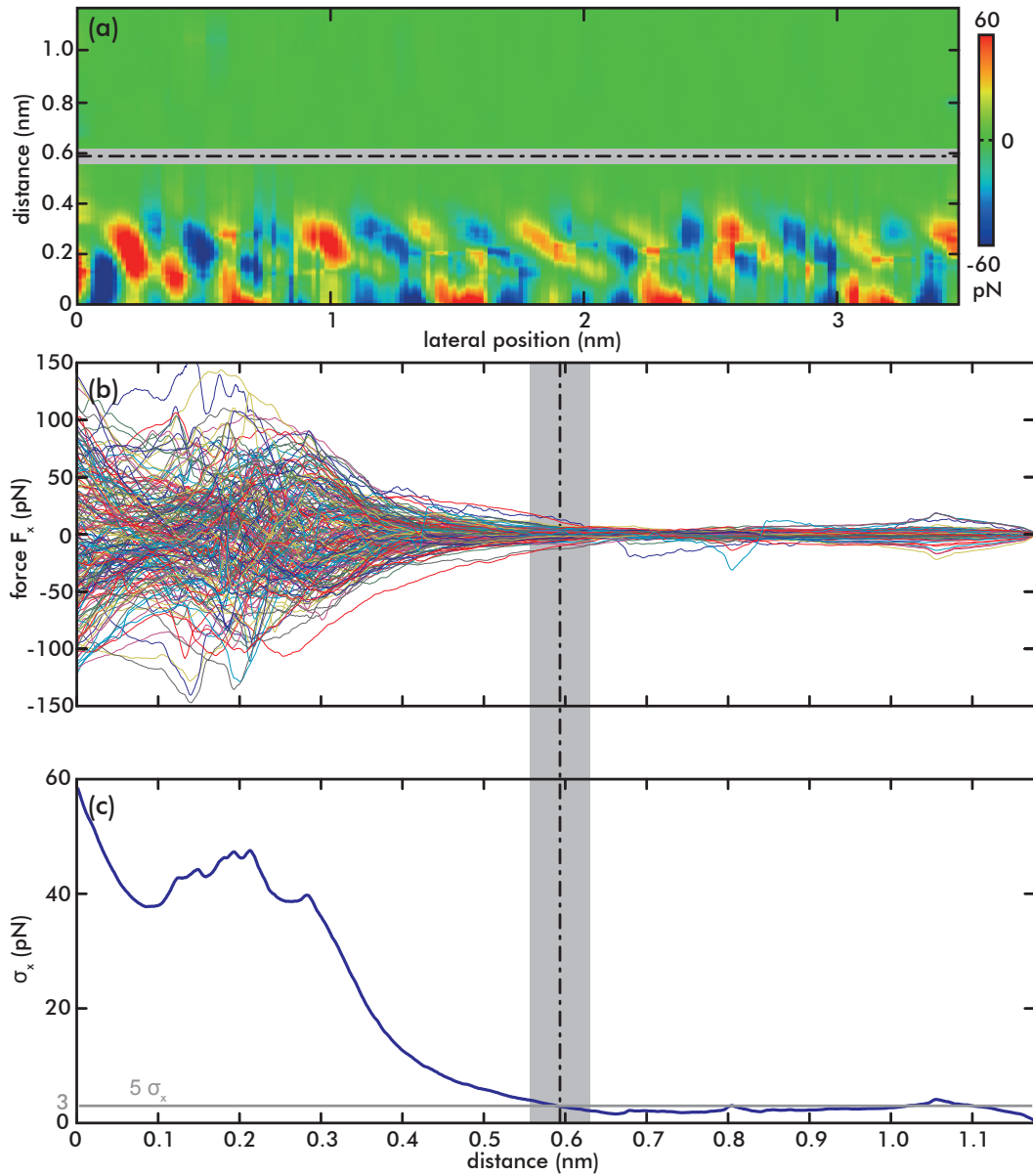


Fig. 4.8.: (a) Lateral force data. (b) F_x extracted from each lateral position within the dataset. (c) Calculated standard deviation σ_x . The onset of lateral forces and, thus, the cutoff is indicated by the dash-dotted line.

4.5 Error analysis

We discuss the resulting uncertainties in the short-range force extraction by examining two distinguished points of the short-range $F_{z,SR}$ force curve, namely the force minimum F_{\min} including its position z_{\min} and the position z_{zero} of the zero in the short-range force data.

Figure 4.10 presents these positions calculated for the van der Waals force models F_2 , F_3 , F_5 and F_{6b} when varying z_{cut} . We marked the cutoff positions according to the three criteria by vertical lines.

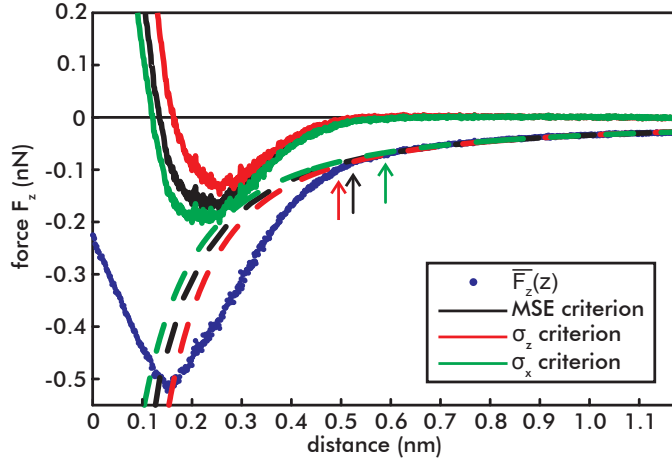


Fig. 4.9.: Resulting forces $\overline{F_{z,\text{SR}}}(z) = \overline{F_z}(z) - F_{\text{vdW}}(z)$ comparing the three criteria for z_{cut} using model F_{6b} . The experimental mean curve (blue dots), van-der-Waals fits (dashed lines) and extracted short-range forces (solid lines) are shown. The three cutoff positions derived from the three criteria are indicated by coloured arrows.

First, we find from the range $z_{\text{cut}} \in [4.9 \text{ \AA}, 5.8 \text{ \AA}]$ uncertainties that result from choosing different criteria for the cutoff position z_{cut} . For our data, we find uncertainties of the positions of minimum and zero force in the order of 40 pm and an error of about 60 pN in the magnitude of the minimum force for F_{6b} . These uncertainties are marked by gray shaded rectangles in Fig. 4.10.

However, our analysis before suggested that using the σ_x criterion only is a more reliable approach. Consequently, we secondly evaluate all reasonable models F_2 , F_3 , F_5 and F_{6b} for this criterion and find uncertainties for the minimum and zero positions of about 45 pm and an error for the minimum force of 70 pN (marked in red in Fig. 4.10). These errors solely arise from the uncertainty in the model selection by using one cutoff position. We suggest using these uncertainties as the final errors.

4.6 Conclusion

We presented a strategy to subtract long-range van der Waals forces from the total vertical force interaction data acquired in NC-AFM experiments. Our method covers the common case where no reference curve at a carefully chosen “off”-position is available and under the assumption of reasonable macroscopic tip geometries. It relies on the known principle of fitting a suitable force law to the long-range interaction regime and subtract the resulting fit including its extrapolation into the short-range regime from the total force data. We showcased a detailed analysis for experimental data acquired on the calcite(10.4) surface.

A total of ten different force laws reported in literature were analysed with respect to their fit characteristics, their fit quality to exemplary data acquired on the calcite(10.4) surface and the reasonability of their resulting parameters. We found a

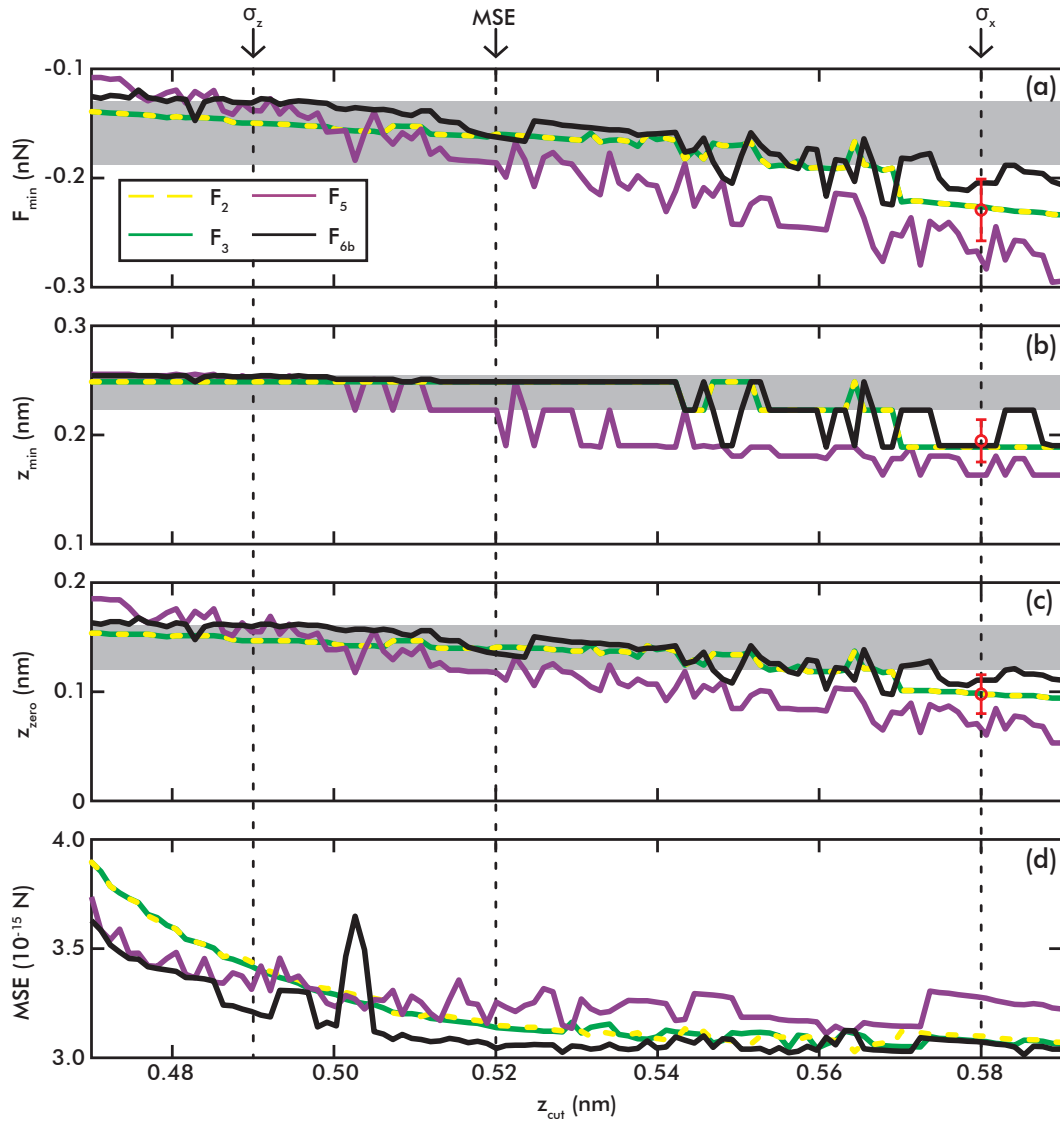


Fig. 4.10.: Error analysis based on calculating F_{min} , z_{min} and z_{zero} for relevant force laws F_2 , F_3 , F_5 and F_{6b} . Data is plotted against the cutoff z_{cut} with the criteria derived before marked. Gray shaded areas denote the error arising from different cutoff positions using F_{6b} , while uncertainties from the model selection are marked by red error bars at $z_{\text{cut}} = 0.58$ nm.

reasonable description of the van der Waals interaction for our experimental data by only four of the ten models. The most crucial point is the determination of the cutoff position for the fit, which is the transition from virtually pure long-range interaction to mixed long- and short-range forces. We introduced three criteria, namely the fit quality and the variance in vertical and lateral forces and suggest to use the criterion based on the variance of the lateral forces.

Finally, we presented an error analysis to determine the reliability of this method by determining the force minimum and zero position, especially for different cutoff positions and force models. This analysis clearly indicates the challenges and quantifies resulting uncertainties when subtracting the van der Waals data from total force data based on fitting a van der Waals interaction model.

Bulk insulator surfaces

Contents

5.1	Calcite CaCO_3	59
5.2	Dolomite $\text{CaMg}(\text{CO}_3)_2$	61
5.3	Magnesite MgCO_3	63

In this work, bulk insulator surfaces are studied, namely surfaces of carbonate minerals. The most common representative of this material class is CaCO_3 , which consists of Ca^{2+} ions and CO_3^{2-} groups. Calcite, the most stable polymorph of CaCO_3 , is one of the most ubiquitous minerals and plays a major role in biomineralisation processes [1]. Highly related are the materials dolomite $\text{CaMg}(\text{CO}_3)_2$ and magnesite MgCO_3 , which were also studied in this work. While magnesite is composed of Mg^{2+} ions and CO_3^{2-} groups, dolomite is the mixed phase of calcium and magnesium carbonate.

The central substrate for the present work was calcite CaCO_3 and its most stable cleavage plane, the (10.4) surface. A summary of its main properties will be given in Section 5.1, followed by introductions to dolomite and magnesite, respectively, in Section 5.2 and Section 5.3 with focus on the (10.4) planes.

5.1 Calcite CaCO_3

Calcium carbonate is one of the most abundant simple salts in nature. It is the main component of most limestones in sedimentary rocks [124]. Furthermore, it can be found in marine organisms such as sea shells or slugs or calcareous sponges [125], which is why it is highly relevant to biomineralisation [1]. CaCO_3 can crystallise in many different polymorphs, of which calcite is the thermodynamically most stable one. Two additional anhydrous forms can be found in nature, namely aragonite and vaterite, where the latter is a metastable hexagonal phase [124]. Calcite has been discussed as a possible origin for the homochirality of life [6]

Calcite crystallises in a trigonal crystal system described by the space group $R\bar{3}c$ [125]. It has a band gap of $E_g = 6.0$ eV, which makes it transparent in the visual regime [126]. Furthermore, it is known for its birefringence [127], making it relevant for applications in the field of optics.

The most stable cleavage plane of calcite is the (10.4) surface because cutting a bulk crystal along that plane breaks the fewest Ca-O bonds. In addition, this plane is electronically neutral. The surface energy has been calculated to 590 mJ/m^2 in the

majority of studies [128–130], although the values in literature vary between 230 and 860 mJ/m² as compiled in [131]. A model of the CaCO₃(10.4) surface is given in Fig. 5.1.

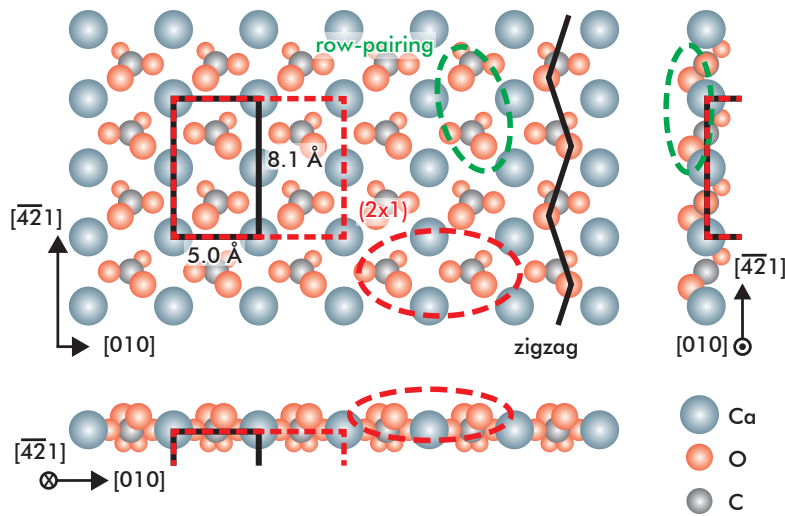


Fig. 5.1.: Bulk-truncated structure of the calcite (10.4) surface. The surface unit cell (black rectangle), the zigzag (black line), the (2×1) reconstruction (red dashed ellipse and rectangle) and the *row-pairing* reconstruction (green dashed ellipse) are marked. Adapted from [25].

The bulk-truncated, unreconstructed surface of calcite(10.4) has a rectangular unit cell with dimensions of $4.99 \times 8.10 \text{ \AA}^2$ [132], marked with a black rectangle in Fig. 5.1, and with the unit cell vectors \vec{a} and \vec{b} oriented along the $[010]$ and $[\bar{4}21]$ crystallographic directions, respectively. Two calcium ions and two carbonate groups are located within every unit cell, the two carbonate groups being tilted in the bulk by an angle of 44.63° with respect to the (10.4) planes [124, 132]. It follows from this that one oxygen atom of the carbonate group protrudes the plane of the calcium atom, while another is in plane and the third one beneath it. Additionally, these two carbonate groups are rotated with respect to each other, causing the protruding oxygen atom to point either to the left or to the right in a zigzag pattern, indicated by the black line in Fig. 5.1. It is the tilt of the carbonate groups, which reduces the symmetry of the surface and makes it a member of the plane symmetry group pg . Only one glide plane reflection with the glide axis oriented along the $[\bar{4}21]$ direction is left as a surface isomorphism [7] and, consequently, the $[\bar{4}21]$ and $[4\bar{2}1]$ directions are not equivalent. Consequently, this surface is not a chiral one due to the existence of the glide plane axis [133]. It is to note that the undetermined surface orientation is fully defined by the tilt direction of the carbonate groups.

Two reconstructions exist for the CaCO₃(10.4), which have been observed before, but their existence and origin are still discussed controversially [133–136]. These are the *row-pairing* and the (2×1) reconstruction. The latter has first been observed

by Low-Energy Electron Diffraction (LEED) in 1991 in $[010]$ direction [135]. For the (2×1) reconstruction, two bright spots along the $[010]$ direction are not imaged the same, for instance one might appear brighter than the other in AFM. This reconstruction results in a doubling of the surface unit cell, as is indicated by the red dashed rectangle in Fig. 5.1.

The *row-pairing* reconstruction has first been observed in 1992 with AFM in aqueous solution [134]. For the *row-pairing*, two of the bright spots appear differently, what might give the impression of paired spots. As this reconstruction is observed along the $[\bar{4}21]$ direction, the unit cell is not doubled by the *row-pairing*. The pairing groups are marked by a green ellipse in Fig. 5.1.

Figure 5.2 shows typical NC-AFM images on the calcite (10.4) surface. When following the preparation procedure as described above in Section 2.3 an atomically flat and clean surface is observed at larger scan sizes, see Fig. 5.2(a). After atomic resolution was achieved a typical contrast can be found, even revealing an atomic defect in Fig. 5.2(b).

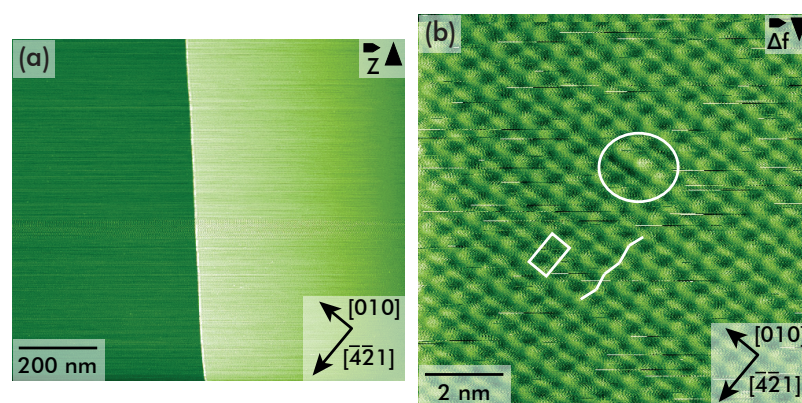


Fig. 5.2.: NC-AFM images of calcite (10.4). (a) Large scan area of $1 \times 0.87 \mu\text{m}$, showing a step edge. The surface is atomically flat and clean. (b) Atomic resolution. The unit cell, the zigzag and a surface defect are marked in white. The image size is 10×10 nm.

A comprehensive study of the contrast formation of $\text{CaCO}_3(10.4)$ with NC-AFM, and a discussion of the reconstructions has been given in a paper by Rahe *et al.* [109].

5.2 Dolomite $\text{CaMg}(\text{CO}_3)_2$

Dolomite belongs to the group of carbonate minerals and is like calcite one of the most abundant rock-forming minerals [125]. Dolomite is mainly found in sedimentary rocks, but also in metamorphic and hydrothermal deposits [124]. Dolomite and calcite play a key role in the so-called long term carbon cycle [9]. Despite its abundance in sedimentary rocks it can hardly be found in marine environments, which stands in contrast to calcite. This is known as the "dolomite problem" [10]. As a consequence, it has so far not been possible to synthesize dolomite under normal temperatures in aqueous solution. This leads one to assume that, regardless of only

small difference in structure, calcite and dolomite are fundamentally different in their macroscopic behaviour.

The structure of $\text{CaMg}(\text{CO}_3)_2$ is very similar to CaCO_3 only that it contains Ca^{2+} and Mg^{2+} as cations. Consequently, dolomite has a lower symmetry than calcite, filing it to the space group $R\bar{3}$ [124]. Both materials have in common their most stable cleavage plane, which is the (10.4) surface. The $\text{CaMg}(\text{CO}_3)_2(10.4)$ surface is shown in Fig. 5.3.

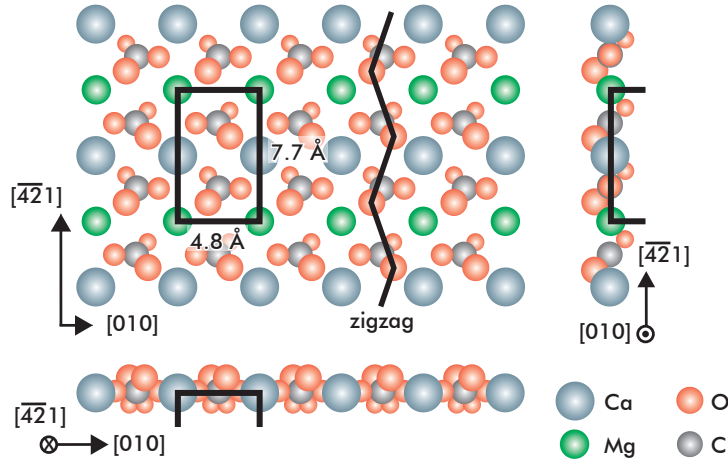


Fig. 5.3.: Bulk truncated structure of the dolomite (10.4) surface. The surface unit cell (black rectangle) and the zigzag (black line) are marked. The cations alternate along the $[\bar{4}21]$ direction, while perpendicular they remain the same.

As can be seen in Fig. 5.3, the cations alternate in $[\bar{4}21]$ direction, while they remain the same for each row in $[010]$ direction. As a consequence, the described glide plane reflection for calcite is no longer present for dolomite, which makes the $\text{CaMg}(\text{CO}_3)_2(10.4)$ surface chiral. Due to the smaller size of the Mg^{2+} ions, the size of the unit cell reduces, compared to the one of calcite. The size of the unit cell is $4.81 \times 7.70 \text{ \AA}^2$ in dolomite [124]. Values for the surface energy of dolomite (10.4) have been calculated to 601 mJ/m^2 [128] and 640 mJ/m^2 [129] and are, thus, slightly higher than the surface energy for calcite (10.4).

It follows from the described "dolomite problem" above that the dolomite samples for this work consisted of natural dolomite, unlike the calcite samples, which were synthetic. Figure 5.4 shows NC-AFM images on dolomite (10.4) in different scan sizes. From the large scale image in Fig. 5.4(a) it becomes apparent that when following the preparation procedure as described in Section 2.3, which is quite different from the one for calcite, the surface is considerably dirty compared to CaCO_3 . This is understandable, though, because the first annealing temperature was significantly lower than for calcite, whereas the second annealing step was skipped completely after cleaving. It turned out that the crystal started outgassing when the annealing temperature of the sample was too high. This resulted in even dirtier surfaces. Also heating the sample after cleaving causes an increased adsorption of contaminations. All of this is plausible since the dolomite samples were not synthetic,

as it was the case with calcite, so contaminations are to be expected. Figure 5.4(b) gives an impression of scanning the surface at smaller scan sizes after performing the described preparation procedure. A very sharp tip was present as demonstrated by the atomic resolution obtained at that large scan size. In this case, the sample surface is very dirty, making it almost impossible to measure on larger scan areas without tip changes as seen in the image. All this makes it very challenging to find even very small scan areas without contaminations to achieve stable atomic resolution as shown in Fig. 5.4(c). The unit cell and the zigzag are marked in white. In the middle of the image, both halves are laterally slightly offset to one another, which is due to an atom-tracking step, where the tip jumped to an adjacent atom during tracking. This is indicated by the white arrow. A strong *row-pairing* contrast is apparent.

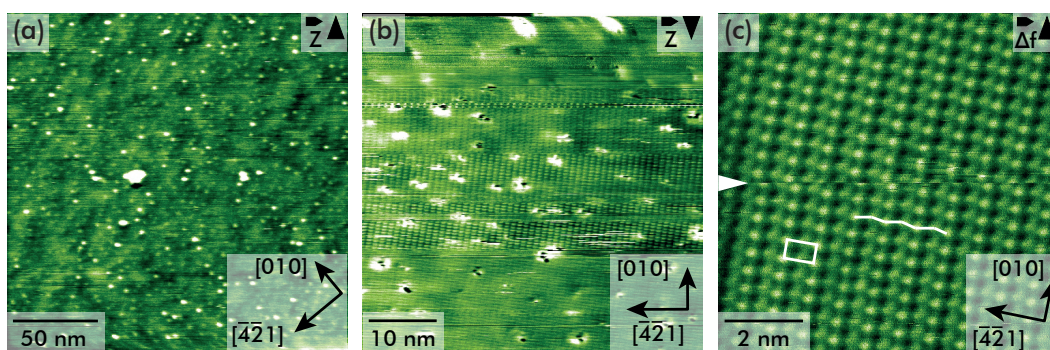


Fig. 5.4.: NC-AFM images of dolomite (10.4). (a) Large scan area of 200×200 nm. The surface is rather dirty compared to calcite as seen in Fig. 5.2(a). (b) In a scan area of 50×50 nm many defects and contaminations can be seen. Even though a sharp tip is present, obvious by the atomic resolution at this scan size, tip changes occur frequently and stable imaging is often prohibited. (c) Atomic resolution. The unit cell and the zigzag are marked in white. The white arrow indicates a tracking step. The image size is 10×10 nm.

The NC-AFM contrast formation on dolomite is comparable to calcite. There has been an extensive study by Kawai *et al.* who give an overview of different contrasts on $\text{CaMg}(\text{CO}_3)_2$ (10.4) using bimodal AFM [137]. It is to note, that in this study as well as in the present work the *row-pairing* was frequently observed (see Fig. 5.4(c)), but never the (2×1) reconstruction.

5.3 Magnesite MgCO_3

Magnesite MgCO_3 , another carbonate mineral, is structurally almost identical to calcite. The only difference are the Mg^{2+} ions instead of Ca^{2+} ions. Magnesite belongs to one of the main rock-forming minerals and can mainly be found as an alteration product of various magnesium-rich igneous and metamorphic rocks [124]. Magnesite belongs, like calcite, to the space group $R\bar{3}c$ [124]. Again, the most stable cleavage plane is the (10.4) surface which is shown in Fig. 5.5.

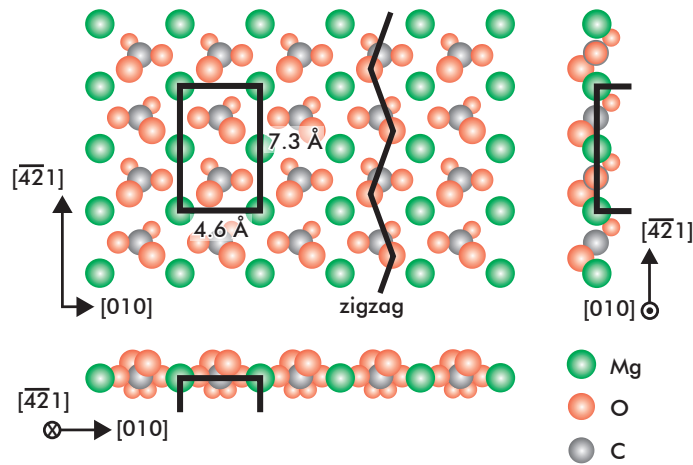


Fig. 5.5.: Bulk-truncated structure of the magnesite (10.4) surface. The surface unit cell (black rectangle) and the zigzag (black line) are marked.

When comparing Figs. 5.1 and 5.5 it becomes apparent that the only difference between calcite and magnesite is the smaller cation for the latter, which results in a smaller unit cell. The unit cell has been determined to $4.63 \times 7.33 \text{ \AA}^2$ [124]. Like calcite (10.4), magnesite (10.4) has a higher symmetry than dolomite (10.4). For the magnesite surface, a glide plane reflection is present, making it a member of the plane symmetry group pg . The surface energy of $\text{MgCO}_3(10.4)$ has been calculated to 760 mJ/m^2 [129].

Figure 5.6(a) shows a large-scale NC-AFM image with a step edge at the bottom right. Compared to Fig. 5.2(a), the surface is less clean, but less dirty than the surface of dolomite shown in Fig. 5.4(a). Since the magnesite crystals were natural as well, the same preparation procedure was applied as it was for dolomite. Consequently, it is understandable that the magnesite surface is less clean than the synthetic calcite samples. Still, atomic resolution was obtained as shown in Fig. 5.6(b), even with a point defect (white circle). The unit cell and the zigzag are marked in white, as well as a tracking step as described before for dolomite. Additionally, a strong *row-pairing* contrast can be observed. However, the (2×1) reconstruction was never seen on magnesite throughout this work.

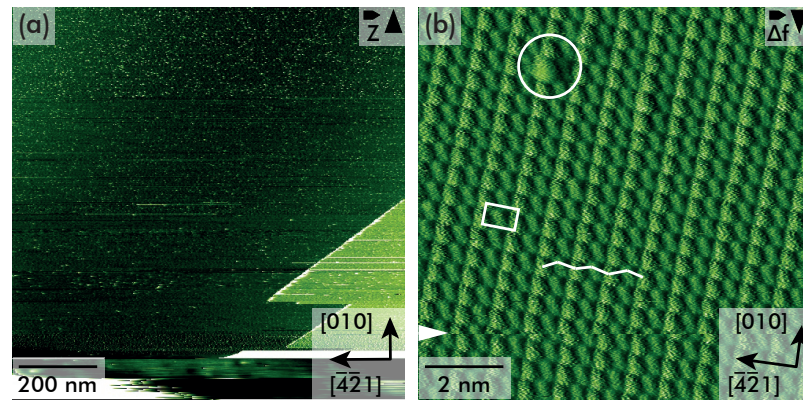


Fig. 5.6.: NC-AFM images of magnesite (10.4). (a) Large scan area of $1 \times 1 \mu\text{m}$. The surface is rather dirty compared to calcite in Fig. 5.2(a). (b) Achieved atomic resolution. The unit cell and the zigzag are marked in white. The white arrow indicates a tracking step. The image size is $10 \times 10 \text{ nm}$.

Force mapping experiments on bulk insulators

Contents

6.1	Identifying the absolute orientation of a low-symmetry surface in real space	68
6.1.1	Introduction	68
6.1.2	Properties of calcite	69
6.1.3	Optical identification	70
6.1.4	Tip-sample force measurement	71
6.1.5	Discussion	74
6.1.6	Conclusions	77
6.2	Force mapping on other bulk insulators	78
6.2.1	Magnesite	78
6.2.2	Dolomite	82
6.3	Aim for chemical identification	83

Investigating the properties of metallic or insulating surfaces at the atomic scale has progressed enormously during the last decades. Especially with the advent of scanning probe microscopy (SPM) techniques [11, 13], studies in real space of bare surface terminations [12, 138, 139] or molecular superstructures [140, 141] including the study of single molecules [23, 142] became possible. Among the long list of relevant surface properties, surface *symmetry* is probably the most decisive parameter. A knowledge of this basic surface property is of utmost importance for understanding key aspects of physico-chemical processes, especially for materials relevant in material science or abundant in the natural environment. In this context, a particularly interesting crystal is calcite due to its abundance in remarkable organic/inorganic hybrid materials known as biominerals.

This chapter presents atomic-scale force interaction data on the insulating low-symmetry substrates calcite, magnesite and dolomite, specifically on their (10.4) surfaces. Section 6.1 includes the calcite data and a detailed discussion of how they allow for a microscopic way to determine the absolute surface orientation. These results were obtained in a close collaboration with Philipp Rahe and are already published [72]. Furthermore, a detailed description of the force fields acquired on magnesite and dolomite will follow in Section 6.2 with a comparison of these substrates to calcite. Additionally, impressive results have proven that a chemical

identification of the imaged species is possible with NC-AFM. Since all prerequisites for a discrimination between surface species are given within this work, Section 6.3 describes analysis approaches aiming at the chemical identification of the different cations for the chosen substrates.

6.1 Identifying the absolute orientation of a low-symmetry surface in real space

This section presents the data for calcite. At first the relevant properties of calcite are recalled in Section 6.1.2 followed in Section 6.1.3 by the description of an optical method to independently determine the absolute orientation of the used sample. The results presented in Section 6.1.4 show a pronounced asymmetry of the imaged species which is apparent along the vertical axis and which will be identified as a tilted band of purely attractive short-range interaction forces as discussed in Section 6.1.5. The macroscopic determination of the absolute surface orientation suggests that the observed asymmetry is related to the tilt of the carbonate groups within the surface which, in turn, is linked to the surface orientation. This allows for an NC-AFM based determination of the absolute orientation of a low-symmetry surface.

Within this work I acquired a total of five 2D force maps along the $[4\bar{2}\bar{1}]$ direction as well as another five 2D slices along the $[010]$ direction. Since the microscopic determination of the absolute orientation is depending on the tilt of the carbonate groups along the $[4\bar{2}\bar{1}]$ direction, as will be shown in Section 6.1.5, the 2D slices along the $[010]$ direction are not discussed here, but briefly presented in Appendix B.

6.1.1 Introduction

For this study the substrate of choice is a surface with low symmetry. Interestingly, most surfaces studied with non-contact atomic force microscopy (NC-AFM) so far contain a large number of surface symmetry elements and the absolute surface orientation is commonly directly identified from *imaging* the unit cell with SPM. To name two examples, the prototypical dielectric substrates KBr(001) and NaCl(001) which have routinely been used for atomic-scale investigations [22, 62, 63, 143], molecular adsorption studies [140] or surface patterning [144], belong to the point group $Fm\bar{3}m$ [124]. In contrast, the absolute surface orientation can firsthand remain undisclosed in images from surfaces exhibiting a low symmetry. Especially in the NC-AFM images presented so far from the calcite(10.4) and the related dolomite(10.4) surface [109, 137], one surface direction remains undetermined.

Here we disclose this key symmetry property of the calcite(10.4) surface from short-range force data acquired with NC-AFM. The data reveals the orientation of the symmetry-breaking, tilted carbonate ion CO_3^{2-} in the calcite(10.4) surface. A macroscopic optical method allows to confirm this orientation by independent means.

The data acquisition and analysis methodology has been described in Sections 2.5.1 and 3.1. How the vertical short-range and the lateral forces were obtained was described in detail in Chapter 4 and Section 3.3. Section 5.1 introduced the calcite(10.4) surface, whereas in Section 6.1.2 a quick summary with special focus on the symmetry properties will be given. The macroscopic approach to determine the absolute orientation is outlined in Section 6.1.3 and followed by the microscopic observations, namely the tip-sample force interactions, including a model for the underlying imaging mechanism (Section 6.1.4 and Section 6.1.5).

6.1.2 Properties of calcite

As outlined in Section 5.1, the unreconstructed, rectangular unit cell of calcite(10.4) has the dimensions [132] of $4.99 \times 8.10 \text{ \AA}^2$. The two carbonate groups within the unit cell are tilted by an angle of 44.63° with respect to the (10.4) planes (see Fig. 6.1(a)) [124, 132] but are also rotated with respect to each other, causing a zigzag pattern of the protruding oxygens along $[\bar{4}21]$ (see Fig. 6.1(a)). It shall be stressed here that mainly the tilt of the carbonate groups, as visualised by a green dashed line in Fig. 6.1(a), is responsible for the reduction of the surfaces symmetry. In consequence, as explained in Section 5.1, the $[\bar{4}21]$ and $[42\bar{1}]$ directions are not equivalent. We note that the tilt direction of the carbonate groups define the undetermined surface orientation.

Figure 6.1(b) presents one prototypical contrast reflecting the surface unit cell and the zigzag pattern of the topmost oxygen atoms [109]. The earlier discussed reconstructions (see Section 5.1) are not resolved in this contrast mode. For a discussion of numerous different NC-AFM contrast modes on calcite(10.4) see [109]. Although the general *alignment* of the $[010]$ and $[\bar{4}21]$ surface directions can be obtained in all contrast modes directly from the unit cell size ¹ in XY-scanned images, the absolute surface *orientation*, as mentioned above, remains unknown as the tilt of the carbonate groups are firsthand not revealed within these data (see Fig. 6.1(c) and (d) for both possibilities).

¹Besides a careful calibration of the microscope, the images are corrected for thermal drift [44] and scanner creep to accurately determine the unit cell sizes.

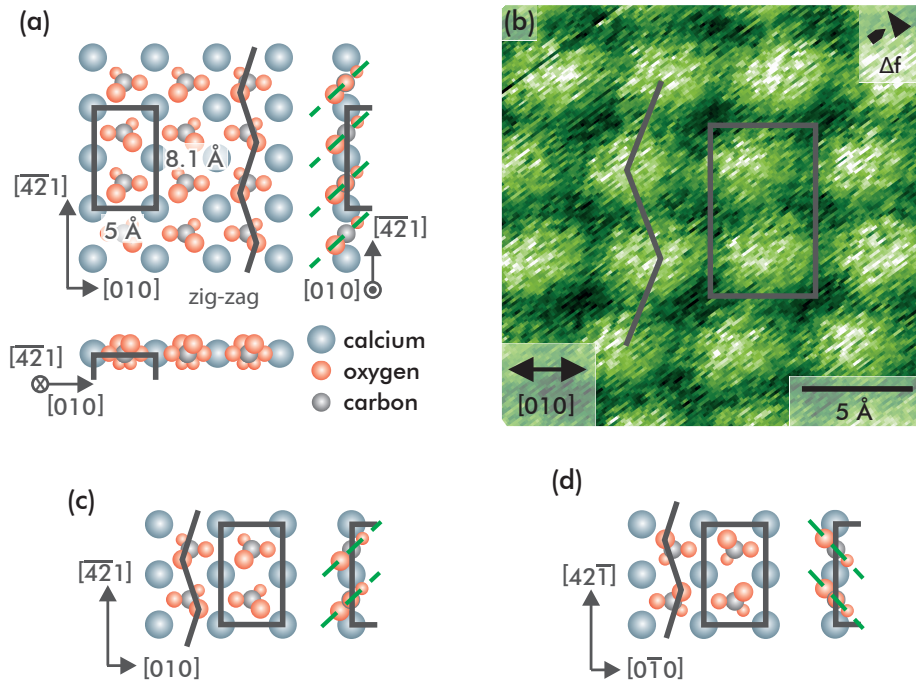


Fig. 6.1.: (a) Model of the (10.4) surface. The tilt of the carbonate groups is visualised by dashed green lines. (b) Typical NC-AFM image representing the zigzag of the protruding oxygen atoms [109]. From measuring the unit cell dimensions, an ambiguity in determining the absolute calcite surface orientation remains. (c) and (d) Two different possibilities leaving the tilt of the carbonate groups unknown.

6.1.3 Optical identification

Besides its natural relevance, calcite constitutes a particularly well-suited sample for relating the surface asymmetry measured within this work on the microscopic scale to the crystal directions. The reason is that this sample provides an independent way of easily identifying the surface orientation by macroscopic means without the necessity of i.e. X-Ray diffraction experiments. This independent, macroscopic method was developed by Philipp Rahe and shall be outlined here.

An analysis of the optical birefringence of the bulk material reveals that the (10.4) projected split vector \vec{p} between the ordinary and extraordinary ray proceeds along the $[42\bar{1}]$ direction (see [25, 72] for the full derivation) as it is defined by

$$\vec{p} = -\frac{2\sqrt{3}act(\epsilon_1 - \epsilon_3)}{12a^2\epsilon_3 + c^2\epsilon_1}\vec{e}_b$$

$$\approx -0.11t\vec{e}_b.$$

In this equation a and c are the bulk lattice constants of calcite, ϵ_1 and ϵ_3 the dielectric constants for the ordinary and extraordinary ray, respectively, t is the

crystal thickness and \vec{e}_b is a normalised unit vector pointing along the $[\overline{4}21]$ direction. The relation between this split vector, the wave vector and the Poynting vectors is outlined in Fig. 6.2(a) and derived in [25, 72].

Photographic pictures of a calcite sample mounted inside the sample holder are shown in Figs. 6.2(b) to (d). A printed black cross is brought beneath a crystal of thickness $t \sim 8$ mm. Subfigures (c) and (d) were acquired with a linear polarizing filter in front of the camera lens. The linear polarizing direction differs by 90° and is indicated in each lower right corner. In Fig. 6.2(c), the picture of the underlying cross caused by the ordinary ray is revealed while panel (d) shows the picture due to the extraordinary ray. The split vector \vec{p} points to the lower left corner, as thus, determines the $[\overline{4}21]$ direction pointing into this direction.

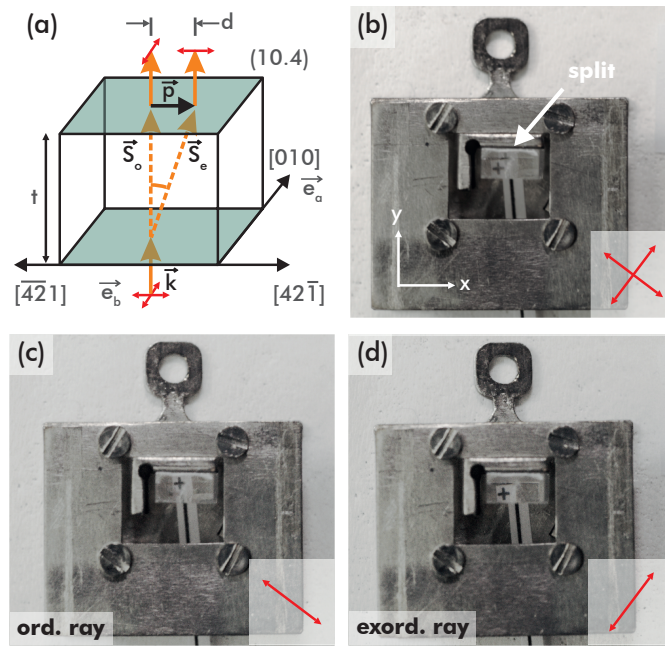


Fig. 6.2.: Macroscopic method to determine the absolute surface orientation. (a) The split vector \vec{p} between the Poynting vectors \vec{S}_o and \vec{S}_e in the (10.4) surface plane points along the $[\overline{4}21]$ direction. This split vector is easily identifiable by determining the ordinary and extraordinary ray using a linear polarizing filter, see panels (c) and (d).

6.1.4 Tip-sample force measurement

In order to microscopically determine the surface orientation and to further understand the tip-calcite interactions, we extend the force measurement to the vertical dimension with results in form of an ZY-slice from the calcite(10.4) surface presented in Fig. 6.3. These data were acquired using the atom-tracking technique [26, 69] for drift compensation and a systematic sampling of the data space as described above. The z -dependent frequency-shift $\Delta f(z)$ data (Fig. 6.3(a)) were acquired along a horizontal line as indicated in the inset. Vertically, the relevant regime of tip-to-sample distances up to about 1.2 nm is reproduced, only site-unspecific long-range forces are

measured at larger z . The total vertical forces F_z (Fig. 6.3(b)) are calculated using the Sader-Jarvis formalism [83] and the short-range vertical forces $F_{z,SR}$ (Fig. 6.3(c)) are extracted from the van der Waals background subtraction [40]. A red (blue) colour depicts an attractive force on the tip to the right (left), respectively, in the lateral forces F_y (Fig. 6.3(d)). The positive horizontal axis points along the $[42\bar{1}]$ (y) calcite direction as determined from the optical criterion for this specific crystal. A tiny misalignment of these data with respect to the axis is apparent from the lateral force data, where a slight decrease in the overall contrast is apparent. The difference appears to be too small to be detectable in the vertical forces. The total force is overall attractive (negative) throughout this data set with the minimum at about -0.6 nN.

The capability of imaging a single defect (marked by dashed yellow circles) indicates the presence of a most sharp AFM tip. The position of the ZY data slice was chosen such that it partly covers this surface defect. The difference in corrugation within each unit cell is ascribed to the zigzag orientation of the carbonate groups. As is apparent from the model in Fig. 6.1(b) every second top-most oxygen atom points out of the plane mapped in the experiment, while every other points inwards. This modulation is apparent in both, vertical and lateral data.

The most striking observation in Fig. 6.3(a) to (d), however, is a significant asymmetry observed in the raw frequency shift Δf and force data sets. When following either a bright or dark region along the Z axis, a bend of the respective regions upon approach to the surface becomes apparent in panels (a) to (c). We include a half-transparent guide to the eye for illustrating this *tilt*. It manifests a clear asymmetry along the vertical axis in accordance with the surface asymmetry along this direction caused by the tilt of the carbonate groups.

We critically analysed the NC-AFM set up and data processing (including the relative tip-to-sample orientation, cantilever tilt, piezo artefacts and force recovery strategy) and found the same orientation of the tilt in repeated experiments under different tip and sample conditions which are described in Appendix B. Consequently, we are confident about a physical origin of the observed tilt and identify two sources: the tilt is supposedly caused by either an asymmetry of the investigated surface or of the scanning tip. An asymmetric tip apex can lead to an asymmetry in the tip-to-sample interaction forces which might propagate either directly or via a tip or a surface relaxation into the measured data. This has been observed before on high-symmetry surfaces, namely on KBr(001) [62, 64], NaCl(001) [63] and graphite(0001) [94]. Any measured asymmetric tilt of the surface species on these substrates is in clear disagreement with the surface geometry and symmetry properties. Consequently, the data have been explained by either a tip deformation or by a tip-induced sample manipulation upon close approach due to an asymmetric tip.

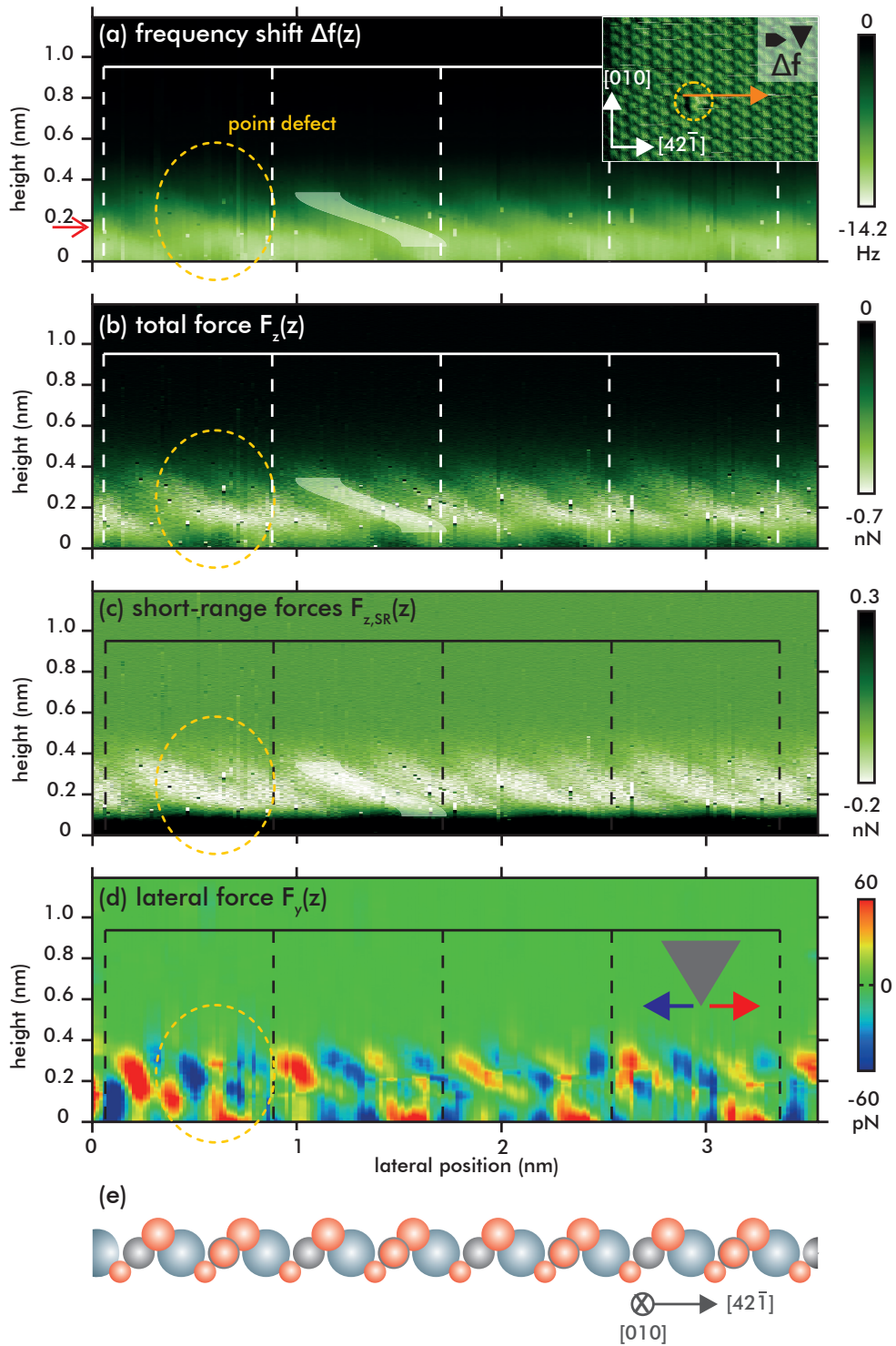


Fig. 6.3.: (a) Frequency shift Δf data from a ZY dataset with size $1.17 \times 3.48 \text{ nm}^2$ (total of 1000×201 pixel). The inset shows the $10 \times 6.7 \text{ nm}^2$ XY-scanned Δf image prior and subsequent to the 2D data acquisition. The orange arrow indicates the position of the ZY measurement, the yellow circle marks a point defect. The z position of this inset is marked by a red triangle at the vertical axis of the ZY dataset. (b) Total vertical interaction force F_z calculated from (a). (c) Short-range vertical forces $F_{z,SR}$ and (d) lateral forces. Unit cell periodicity is marked in all images and the half-transparent lines guide the eye to the tilted features. (e) True to scale calcite(10.4) surface model aligned according to long-range attractive interactions with the CO_3^{2-} groups.

6.1.5 Discussion

Foster *et al.* modelled the calcite surface structure in presence of a scanning probe tip and found a surface relaxation including shifts of all surface species as well as a rotation of the surface carbonate groups [143, 145]. Their numerical calculations have furthermore suggested two possibilities for the tip-to-surface interaction [143]: a more attractive force between the AFM tip and either the calcium or the carbonate ion, causing the carbonate group being either pushed into or pulled outwards from the surface by the atop positioned tip.

Our data is in agreement with the latter situation, namely a larger attractive interaction between the tip and the carbonate ion: First, we observe at small tip-to-sample distances a zigzag structure (see inset Fig. 6.3(a)) that has been associated with the alternating orientation of the protruding oxygen atoms before [143, 146]. Second, the high-symmetric calcium atoms are unlikely to cause a tilted feature. Third, this assignment would, in a straightforward electrostatic picture, be in agreement with a positive tip termination. This situation has been postulated before as one imaging mode for the calcite(10.4) surface [143, 145] and has also been suggested as a general property of conducting tips [117].

Following this conclusion, an analysis of the transition from site-unspecific long-range interactions to the site-specific short-range interaction regime in the total vertical force F_z data allows for assigning the surface species. Figure 6.4(a) presents a line profile from this regime, extracted at $z = 4.2 \text{ \AA}$ and averaged over 0.59 \AA (see Fig. 6.4(b)). A sinusoidal function is fitted to the experimental data (in red) as a guide to the eye. At this tip-to-sample distance we expect to measure the surface structure mainly undisturbed by the presence of the tip and, thus, we can use this region to relate our experimental data to a model of the surface structure.

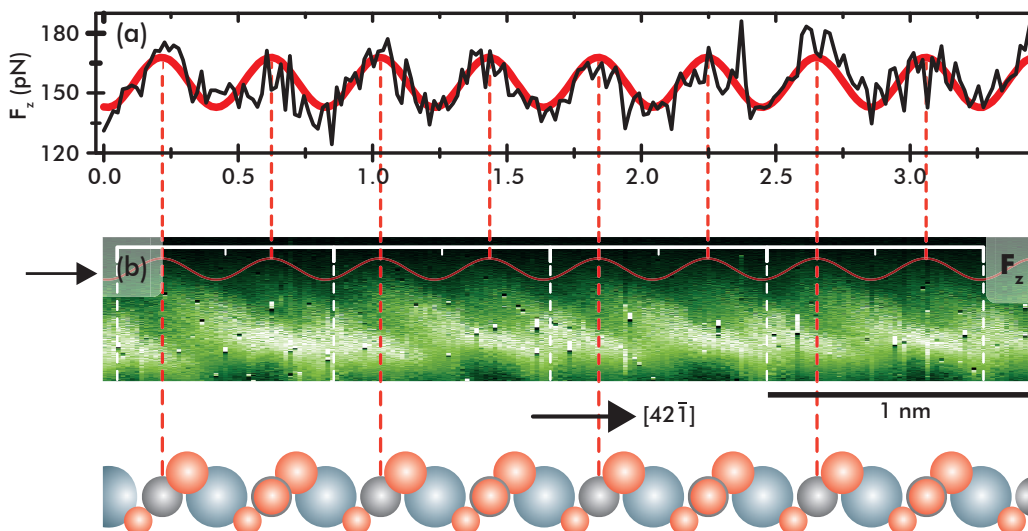


Fig. 6.4.: Onset of total vertical forces F_z employed for the assignment of surface species in the data set. The line profile in (a) is extracted at the vertical onset of atomic corrugation at $z = 4.2 \text{ \AA}$ from the F_z data.

If we assume an attractive interaction of the tip with the full carbonate group as substantiated before, we can assign the positions of maximum attractive interaction to the positions of the carbonate group centres as depicted in Fig. 6.4. Interestingly, this assignment is in agreement with the measurement of lateral forces presented later in Fig. 6.5(b). We find a sector towards which the tip feels an attractive force from both, the left and the right side in the lateral forces. This sector is located in-between the red and blue area. Importantly, these areas of large lateral forces are clearly tilted and this tilt has the same orientation as observed in the vertical forces before.

Thus, these data are in full agreement with imaging the carbonate groups attractive and as a single entity at large tip-sample distances (height z_1). The surface structure in Figs. 6.3 and Fig. 6.5 are accordingly included.

To further analyse the tip-surface interaction mechanism on the calcite(10.4) surface, we focus on the vertical $F_{z,\text{SR}}$ and lateral F_y short-range forces across a single unit cell extracted from the full dataset and reproduced in Fig. 6.5(a) and (b), respectively. The short-range forces $F_{z,\text{SR}}$ describe the specific interaction of the tip front atoms with each surface species. We determine the tip height for the optimum binding position from the zero of $F_{z,\text{SR}}$ (simultaneously the minimum of the short-range interaction potential) and mark these heights z_3 by a solid red line in Fig. 6.5(a) and (b). At the same height, the lateral forces exhibit a regime of reduced interactions – a finding giving us strong confidence about the validity of our short-range force extraction procedure.

Based on this analysis, the tilt is exclusively observed at tip-to-sample distances larger than the force zero, namely at heights z_1 and z_2 as marked in Fig. 6.5. This allows us to conclude that purely attractive short-range interactions between the tip apex and the surface species are responsible for the observed tilt. This tilt constitutes the passage from a short-range force uninfluenced carbonate group (at tip-to-sample distances $z > z_1$) to the optimum carbonate binding situation in the combined tip-sample potential (at tip-to-sample distance $z = z_3$).

When uniting all findings, we explain the orientation of the tilt in the regime of attractive short-range forces by a transition between two interactions: at large tip-to-sample distances (around height z_1 in Fig. 6.5) our $F_{z,\text{SR}}$ data suggests the largest attraction between the tip and the carbonate group as one entity. When reducing the tip-to-sample distance at $z < z_1$, we explain the tip-surface attraction being dominated by the force between the tip and the protruding oxygen atom only; the proximity to the oxygen atom is understood to outweigh the attraction to the whole group. Both cases are illustrated in Fig. 6.6. This explanation is further substantiated when inspecting the lateral force F_y data in Fig. 6.5(b). A zone (marked by two triangles) to which the tip is dragged from both the left and the right side is clearly apparent. From the surface structure depicted below, we identify the topmost oxygen

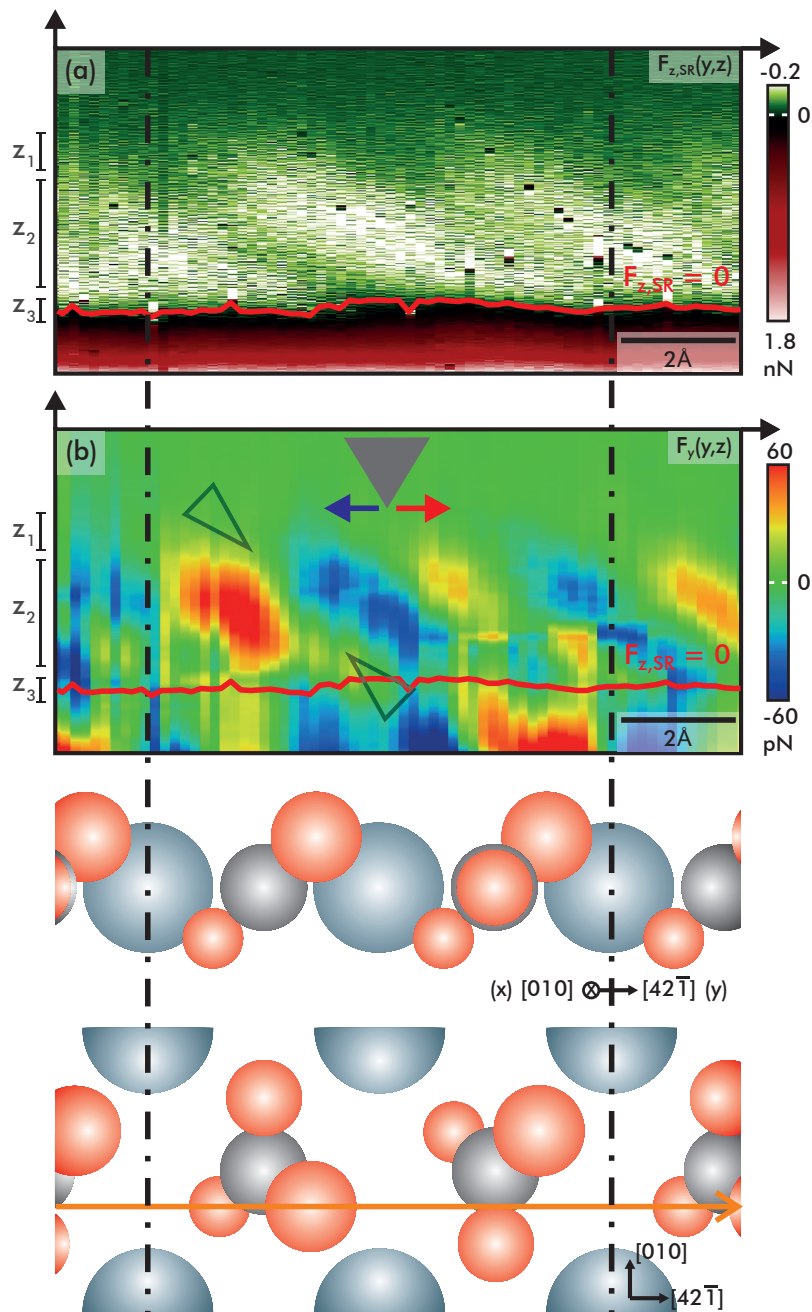


Fig. 6.5.: (a) Vertical short range forces $F_{z,SR}$ and (b) lateral forces F_y extracted for a single surface unit cell. The heights of $F_{z,SR}(z) = 0$ are marked by red lines. (c) Corresponding model in side-view and top-view aligned with the experimental data.

atom lying centred in this zone. With this explanation, the observed shift of the tilt to the right originates in the position of the oxygen atom and, thus, in the orientation of the carbonate group and the surface.

The *trajectory* of the tilt in the lateral and vertical force data within height ranges z_1 and z_2 is in good agreement with the surface geometry. However, relaxation of the surface carbonate group or secondary interactions with the neighbouring surface or tip species could lead to an amplification of the observed tilt, especially giving a

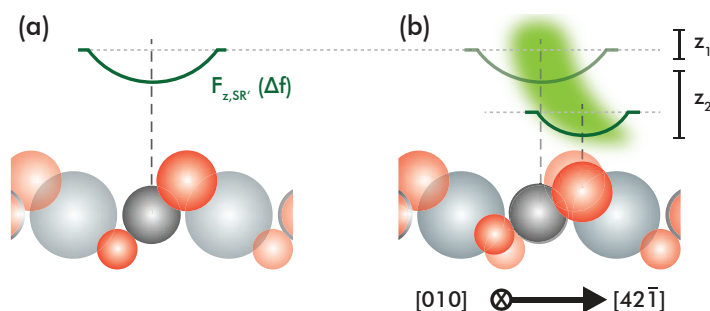


Fig. 6.6.: (a) The full carbonate group is imaged at large tip-sample distances, while (b) the maximum attractive interaction shifts towards the topmost oxygen atom, located at the right.

plausible explanation for the *tail* observed in the vertical interaction at tip-to-sample distances z_3 and closer. The relaxation of single molecules has very recently been measured for the case of two CO molecules [147], which bend towards each other in the attractive interaction regime. The observation of strikingly similar features in our lateral force data leads us to the conclusion that a relaxation of the carbonate group in the surface might amplify the interaction transition, especially at small tip-to-sample distances. The repeatability of observing the same tilt orientation under different conditions, the identification of pure attractive interactions and our explanation gives us strong confidence that the calcite surface is the source for the tilt orientation in our data.

6.1.6 Conclusions

In conclusion, we investigated the tip-sample interaction forces on a low-symmetry substrate, namely the calcite(10.4) surface. We found a pronounced tilt of the measured surface species in our vertical and lateral force data, which we clearly identified as purely attractive short-range interaction. We explain these attractive short-range force data by a transition from the tip interacting with the entire carbonate group to an interaction with the topmost oxygen atom only at reduced tip-to-sample distances. The experimentally observed tilt is related to the surface structure and symmetry and discloses the absolute surface orientation – a parameter especially relevant when studying physico-chemical processes in the context of i.e. understanding and mimicking biomineralisation. Thus, the ability to directly determine an essential surface property from interaction force data constitutes another important step in the field of investigating crystalline surfaces in real space.

6.2 Force mapping on other bulk insulators

With a contrast formation mechanism revealed for calcite, it is now to compare these results to force fields on other related bulk insulator surfaces. For that purpose, magnesite MgCO_3 (10.4) and dolomite $\text{CaMg}(\text{CO}_3)_2$ (10.4) are the obvious choices and so I collected force maps on these substrates. Besides the question whether the same contrast pattern can be observed in these related materials, the most interesting question arising is, whether it is possible or not to distinguish between the different cations on $\text{CaMg}(\text{CO}_3)_2$ with a microscopy-based technique. Such results have already been presented for alloys consisting of Si, Sn and Pb, demonstrating the ability to tell the different species apart by NC-AFM [67], which is why the present work holds the possibility in a chemical identification of the imaged species, as shall be discussed in Section 6.3.

For that purpose, the discussion shall, again, be limited to the data along the $[42\bar{1}]$ direction since this is the direction in which the cations change on the dolomite (10.4) surface (see Fig. 5.3). The data that I acquired along the $[010]$ direction are presented in Appendix B for both cases, magnesite and dolomite.

6.2.1 Magnesite

The force field data for magnesite were obtained in the same manner as the calcite data and as described earlier in Section 2.5. A total of two 3D maps and three 2D maps were successfully recorded. Two of the 2D maps are aligned along the $[42\bar{1}]$ and one perpendicularly along the $[010]$ direction. To increase resolution without further increasing the acquisition time for the full 3D maps, we decided to record two smaller data volumes instead of a single, big map, with the two of them having the resolution considerably reduced in one of the two surface directions but in turn increased along the other direction. Consequently, each of the two data volumes contains dense data along one surface direction, so that the combined 3D maps resolve both surface directions comparable to the 2D slices. This is of great advantage since the overall number of curves, and therefore the time to acquire the data, does not change while the resolution in both directions is increased significantly. This is in contrast to one big data volume, where both directions would have been acquired with inferior resolution.

Figure 6.7 presents an overview of the two ZY slices and the dense data volume along $[42\bar{1}]$. For data conversion, we proceeded as before (see Sections 3.1 and 3.3 and Chapter 4), and since the short-range forces $F_{z,\text{SR}}$ are ultimately to be discussed here, they are presented immediately in Fig. 6.7. Details about the extraction of $F_{z,\text{SR}}$ are compiled in Appendix C.

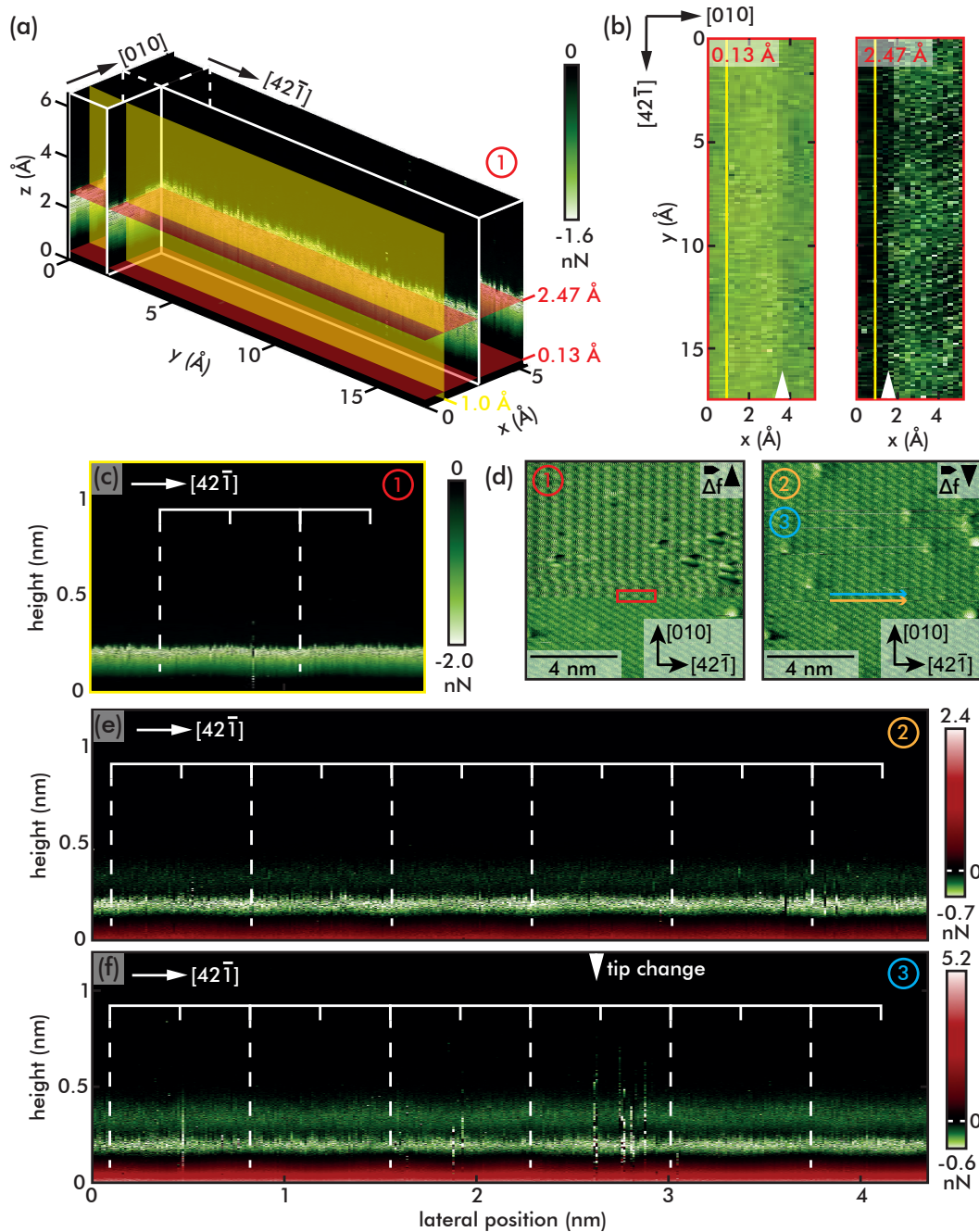


Fig. 6.7.: Force maps on magnesite. (a) Representation of the 3D force map dense along the $[42\bar{1}]$ direction. Dimensions are $0.52 \times 1.74 \times 1.2 \text{ nm}^3$ with a total of $20 \times 157 \times 1000$ pixel. The red (yellow) shaded areas indicate extracted XY (ZY) intersections. (b) XY intersections from different heights, extracted from (a). The yellow line shows the position of the ZY slice, the white arrows point to tip changes. (c) ZY slice along $[42\bar{1}]$ at the position marked in (a). (d) Δf scan images prior and after the force field acquisition with scan size $10 \times 10 \text{ nm}^2$. The red box in the left image shows the position of the 3D map in (a), the blue and orange arrows in the right scan give the positions of the force fields shown (e) and (f). (e) 2D force field along $[42\bar{1}]$ with dimensions of $4.35 \times 1.2 \text{ nm}^2$ and 361×1000 pixel. (f) Second 2D force field along $[42\bar{1}]$ with the same dimensions and number of points as the force field in (e). The unit cell periodicity is highlighted by the white dashed lines. All force fields are immediately presented in terms of short-range forces $F_{z,\text{SR}}$.

The full data volume is represented in Fig. 6.7(a) with the distance Z scale set arbitrarily to 0 Å at the point of closest approach. The force map is of rectangular shape and is aligned along the surface directions with the longer side in $[42\bar{1}]$ direction. The 3D force map has a volume of $0.52 \times 1.74 \times 1.2 \text{ nm}^3$, containing $20 \times 157 \times 1000$ pixel which gives a total of 3140 curves. The resolution along the $[42\bar{1}]$ direction is 11 pm while perpendicularly it is 26 pm. The force map covers more than two consecutive surface unit cells along $[42\bar{1}]$.

With the whole data volume available it is now possible to extract any intersection desired. Two XY planes were extracted as well as a ZY slice, as indicated by the red and yellow shaded areas in Fig. 6.7(a). One XY plane was extracted in the short-range repulsive regime at a height of 0.13 Å, see left image in Fig. 6.7(b), and one in the short-range attractive regime at 2.47 Å, see right image in Fig. 6.7(b). It is important to note that during the data acquisition apparently two tip changes occurred, marked with a white arrow, which are visible at different separations Z. It is to note that the position of the force map on the surface might have changed due to the tip change. Consequently, the ZY cross section, shown as the yellow shaded area and yellow line in Fig. 6.7(a) and (b), respectively, was extracted before the first tip change with the aim to show a slice above the protruding oxygen atoms. This ZY slice is presented in Fig. 6.7(c). The left image in Fig. 6.7(d) shows the scan image before and after the 3D data acquisition. Here, a tip change is immediately visible, since the contrast is significantly different in both parts of the image. The sample is in general rather dirty which increases the probability for a tip change. Additional 2D force fields are available and shown in Fig. 6.7(e) and (f). Both slices have the same dimension, namely $4.35 \times 1.2 \text{ nm}^2$ with the same number of points 361×1000 pixel giving a lateral resolution of 12 pm. This is comparable to that of the 3D map. Both slices are recorded consecutively, so they share the same scan image before and after the force field measurement. The XY image is shown in Fig. 6.7(d) on the right. The positions where they were acquired are marked with an orange and blue arrow, respectively. Furthermore, another tip change is visible in Fig. 6.7(f) as marked by a white arrow.

From the 2D force fields in Fig. 6.7(e) and (f) two separate regions of attractive interaction are visible, a less bright one at greater tip-to-sample distances and a brighter one closer to the sample. Hereby the latter constitutes the global minimum of the $F_{z,\text{SR}}$ curve and shows site-specific contrast, but only with small corrugation. The less bright region is a local minimum in the $F_{z,\text{SR}}$ curve with a depth of roughly 0.2 nN, the blue curve in Fig. C.2(d), hardly showing any dependence on the atomic corrugation. Therefore, we believe that the region of weaker attractive interaction at greater distance Z shows an artefact of the tip. Presumably a peripheral atom at the tip apex relaxes reversibly. Slight contrast in the dissipation channel is visible in this region giving further evidence for this assumption.

Additionally it is to observe that the maximum attractive force $F_{z,SR}$ for the 3D map (1.6 nN) is much larger than that of both the 2D slices. This is probably due to a different tip termination compared to the slices that causes a stronger interaction of tip and sample for the case of the 3D map. Still, the observed contrast in all cases remains roughly the same in the region where strong atomic contrast can be seen, which suggests that the different tip termination does not have a tremendous effect on the imaging mechanism.

When comparing the magnesite force data from Fig. 6.7 with the data on calcite in Fig. 6.3, one realises a different contrast in two regards. First of all, for the calcite case there were two bright imaged features observed within one unit cell, which is indicated by the dashed line in Fig. 6.3(c). This is an intuitive result since the unit cell contains two carbonate groups. These features differ in brightness which can readily be explained by the zigzag: every second of the protruding oxygen atoms is only partly covered by the force slice. For the case of magnesite, only one bright feature is imaged within the unit cell as highlighted in Fig. 6.7(e) and (f). A possible explanation for this might be an extreme manifestation of the zigzag as can be suggested from the XY scan image in Fig. 6.7(d). The zigzag is imaged in such a way that the 2D slice only covers every second oxygen atom.

The far more striking difference in the force fields of calcite and magnesite is the missing tilt of the imaged features for magnesite, as reported above for calcite. In general we believe that the tilt and the mechanism behind it is a feature of the carbonate groups and, therefore, it is expected to be visible in the magnesite force data as well. Even the lateral forces F_y do not show a hint of the tilt for magnesite as exemplary data show in Fig. 6.8.

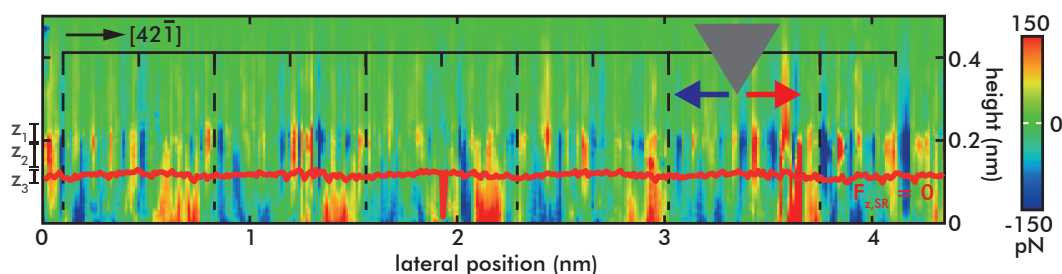


Fig. 6.8.: Lateral forces on magnesite of the dataset shown in Fig. 6.7 (e). The data is cropped and stretched along the vertical axis for better visibility. The red line marks the transition from short-range attractive to short-range repulsive regime, the black dashed lines the unit cell periodicity.

Figure 6.8 shows the lateral forces of the data grid presented in Fig. 6.7(e). Analogue to calcite in Fig. 6.5, the different interaction regimes are marked from z_1 to z_3 . It is immediately visible that region z_2 , the region where the tilt was observed for calcite, is tremendously smaller for the case of magnesite. In regime z_3 , where the transition from short-range attractive to short-range repulsive forces takes place, there is almost no contrast compared to other regions. Entering the repulsive regime, calcite and magnesite show a similar contrast and a clear alternation of attractive

and repulsive lateral forces is visible. Like for calcite, we do not attempt to discuss the repulsive regime since relaxations of the surface species are to be expected, preventing a concluding interpretation from this data only.

An explanation for the missing tilt in the magnesite data could be that the tilt-exhibiting attractive interaction regime z_2 for this specific tip-sample combination is small compared to the tilt itself, assuming the same underlying contrast formation mechanism as for calcite. If only a small region of the tilt can be visualised by the tip it would not appear as a tilted area in the force field. Another explanation could be that this data was obtained with a rather blunt tip of decisively different configuration. Therefore, an interpretation of these data in terms of identifying the contrast formation mechanism is not entirely conclusive.

6.2.2 Dolomite

For dolomite, I acquired one 2D map along the $[010]$ direction and one along the $[42\bar{1}]$. Due to the earlier described difficulties in measuring on dolomite in general (see Section 5.2), a full 3D force field on this substrate is yet to be acquired. Analogue to the previous Section 6.2.1, short-range force $F_{z,SR}$ data are presented for the force map along the $[42\bar{1}]$ direction. Additional details about the extraction of $F_{z,SR}$ are given in Appendix D.

The force map has physical dimensions of $2.175 \times 1.13 \text{ nm}^2$ with 150×1000 pixel, therefore it covers more than two and a half unit cells along the $[42\bar{1}]$ direction. Like all the other force data presented in this work, this force slice is positioned above the protruding oxygen atoms in the $[42\bar{1}]$ direction. The maximum attractive force of around 0.4 nN fits quite well to the observed force maxima for calcite and magnesite. Similar to the case of magnesite, only one bright feature is imaged in every unit cell, which might again find its reasons in the imaging contrast depicted in XY scan image before the force mapping experiment in the inset in Fig. 6.9(a). Contrary to the magnesite data in Fig. 6.7(d), the zigzag is hardly visible in the XY image for dolomite, and the features along the $[42\bar{1}]$ direction appear almost as one continuous stripe. This might be a consequence of an extreme expression of the *row-pairing* reconstruction as has been reported earlier in [109]. In that case two features along the $[42\bar{1}]$ direction appear as one. This would explain the contrast in the XY image and why only one bright feature is visible within the unit cell in the force field. Again, as already observed for magnesite, a tilt in the force field of the imaged features cannot be identified.

The contrast of the lateral forces F_y in Fig. 6.9(b), however, does not have any resemblance to the calcite or magnesite data at all. Apparently a tip change occurred early during the data acquisition as marked with a black arrow. From there on a clear

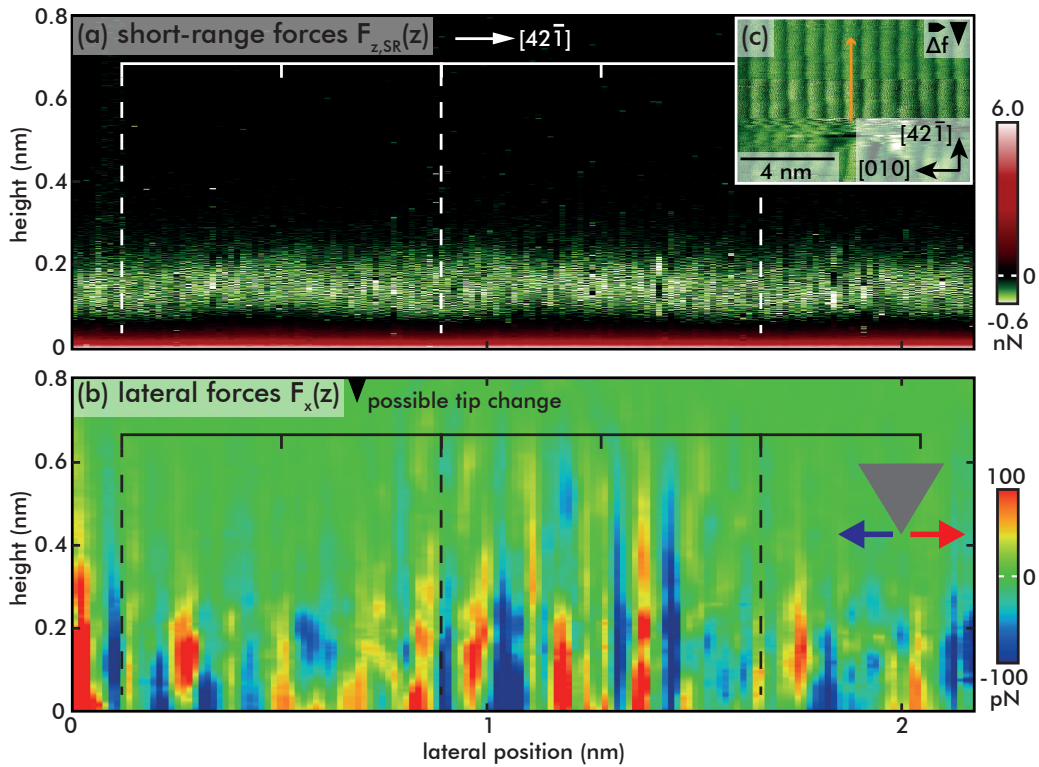


Fig. 6.9.: 2D force map on dolomite. (a) Short-range force $F_{z,SR}$ slice with 150×1000 pixel in $2.175 \times 1.13 \text{ nm}^2$. The inset shows the scan image before and after the data acquisition. The scan size is $10 \times 7 \text{ nm}^2$. A loss of atomic contrast is visible after the completion of the force measurement. (b) Resulting lateral forces F_y of the same data. The dolomite unit cell periodicity is marked with the dashed lines.

pattern in the lateral forces cannot be identified. Interestingly the tip change is not visible in the vertical forces $F_{z,SR}$, but in the lateral force F_y only. From the XY image in the inset of Fig. 6.9(a) it is clear that at some point the tip must have changed. However, based on the $F_{z,SR}$ data only, it is not definitely clear at what point. Since the tip changed rather early during the force measurement, a further data analysis in terms of identifying the regimes of different interaction, as was described for calcite and magnesite, is not an option. These regimes cannot be identified in a meaningful way, so they were not included in Fig. 6.9(b).

Due to the early change of the tip configuration a conclusive analysis of the data is prohibited. An interpretation why the tilt in the beginning of the force map, before the tip change, is not visible remains speculative.

6.3 Aim for chemical identification

It has been reported in literature that NC-AFM holds the potential to identify the chemical nature of the imaged species by force spectroscopy, as was reported by Sugimoto *et al.* in 2007 [67]. In their work they have used an alloy composed of

Si, Sn and Pb as a substrate where they have distinguished the components by comparing the maximum attractive force of each component. For several different cantilevers they have recorded Δf curves above each constituent in an atom-tracking controlled way, and after conversion to $F_{z,SR}$ they have compared the ratio of maximum attractive force for each set of curves. Normalising the Si-tip interaction to 100 % they have determined the relative interaction ratio of Si to Sn to 77 %, and of Si to Pb to 59 %. Furthermore they have found these interaction ratios to remain unchanged for different cantilevers. This significant difference in ratio allows them to unambiguously assign the chemical nature to the imaged atoms. Yet, a chemical identification based on NC-AFM measurements have only once been shown so far. My work holds all the necessary prerequisites to follow the approach of Sugimoto *et al.* for a chemical identification. Not only the technical requirements in form of a well-controlled scan protocol are met, but also the tested extraction of short-range forces allows for a confident analysis of the data. Therefore, the goal of this analysis was a discrimination between the cations Ca^{2+} and Mg^{2+} on the dolomite $\text{CaMg}(\text{CO}_3)_2$ (10.4) surface, complemented by the force data on the calcite and magnesite surfaces. Contrary to [67], for the case of the present work the three different substrates CaCO_3 , MgCO_3 and $\text{CaMg}(\text{CO}_3)_2$ and, therefore, the different species were imaged with different tips each.

In order to follow Sugimotos approach, a suitable surface site has to be found to which the interaction of the cations can be related to. Since the most attractive interaction of the tip is with the carbonate groups as was shown earlier in Section 6.1, the CO_3^{2-} groups pose an intuitive selection.

As a first approach, similar to Sugimoto *et al.*, i determined the interaction ratio at the force minimum for the carbonate group and the cation by averaging all the associated curves for each acquired force map on each substrate. In order to do so, a model of the respective surface was to arranged in a meaningful way beneath the force data to be able to select and group the curves for the surface species that belong together. This was done in the same way as shown earlier in Fig. 6.4: at a distance Z close beneath the onset of vertical force contrast in the attractive regime, a line profile was extracted so the surface model can be placed in such a way that the centre of the CO_3^{2-} groups are in the most attractive regimes of the line profile. When I determined the interaction ratio I found that it is above 90 % for both cations and that they show only a slight difference between Mg^{2+} and Ca^{2+} . Regarding the dolomite force field the interaction ratio for the respective cation sites could not be found.

There are two possibilities why the cations were not distinguished here. First, even if the regions to be averaged are chosen small, with this approach a dataset is divided into two regions which results in considerable averaging. Second, the 2D slices were obtained above the protruding oxygen atoms and, as is apparent from

Fig. 6.5(c), the cation sites are not covered by the slice. A meaningful assignment of the extracted curves to contain only the cation interaction is therefore not possible.

In a second approach I abandoned the classification of curves into different groups. Instead, I extracted the value of the force minimum F_{\min} and its position z_{\min} for every curve along Y (and X where a 3D map was available). The result is an oscillation which was then normalised to the common minimum, which is the point of strongest attractive interaction with the sample. Here the minimum positions are assigned to the carbonate groups, as described above. Consequently, using the underlying surface model, the interaction ratio for the cations can directly be read out from this approach and, thus, no errors were introduced due to averaging. Nevertheless, the problem remains that the cation sites were still not directly covered by the slice.

In order to get rid of this flaw, 3D data on calcite that have been previously acquired by myself [148] were included in the data evaluation. Two more data volumes are available with dimensions of $2.175 \times 1.914 \times 3.2 \text{ nm}^3$ and $2.175 \times 2.175 \times 1.1 \text{ nm}^3$ containing $75 \times 85 \times 500$ pixel and $85 \times 85 \times 500$ pixel, respectively. For completeness' sake the 3D force map on magnesite was included which is dense along the [010] direction. It has the dimensions $0.87 \times 1.688 \times 1.2 \text{ nm}^3$ with $31 \times 152 \times 1000$ pixel. When following the above described procedure of finding F_{\min} for every position (X,Y) one will obtain a two dimensional F_{\min} map. For an initial 2D slice this will produce a line. This is exemplarily shown in the following Fig. 6.10 for the available 3D data on CaCO_3 and MgCO_3 , as well as the relevant slice for $\text{CaMg}(\text{CO}_3)_2$.

I applied this procedure to all available force data and compared them to the F_{\min} map of dolomite. As is apparent from Fig. 6.10(c), a clear distinction between the Ca^{2+} and Mg^{2+} ions is not possible. A detailed analysis gives a ratio of the protruding oxygen to Ca^{2+} of 87% and for Mg^{2+} to Oxygen of 92%. Compared to the results of Sugimoto *et al.*, the obtained ratios are too close together. This does not allow for a clear distinction between the two cations. Additionally, these values cannot be found at the respective positions in the dolomite F_{\min} map and line profile, as shown in Fig. 6.10. A convincing discrimination of the cations is prohibited by the restriction of the dolomite force data to two dimensions because, as it was explained earlier, the cations are not directly covered during the measurement.

Although at least the same 2D slice for every substrate is available, 3D force maps should ideally be used for a convincing analysis of the data. Concluding, for a trustworthy statement on the possibility for chemical identification on these substrates the final evidence is missing.

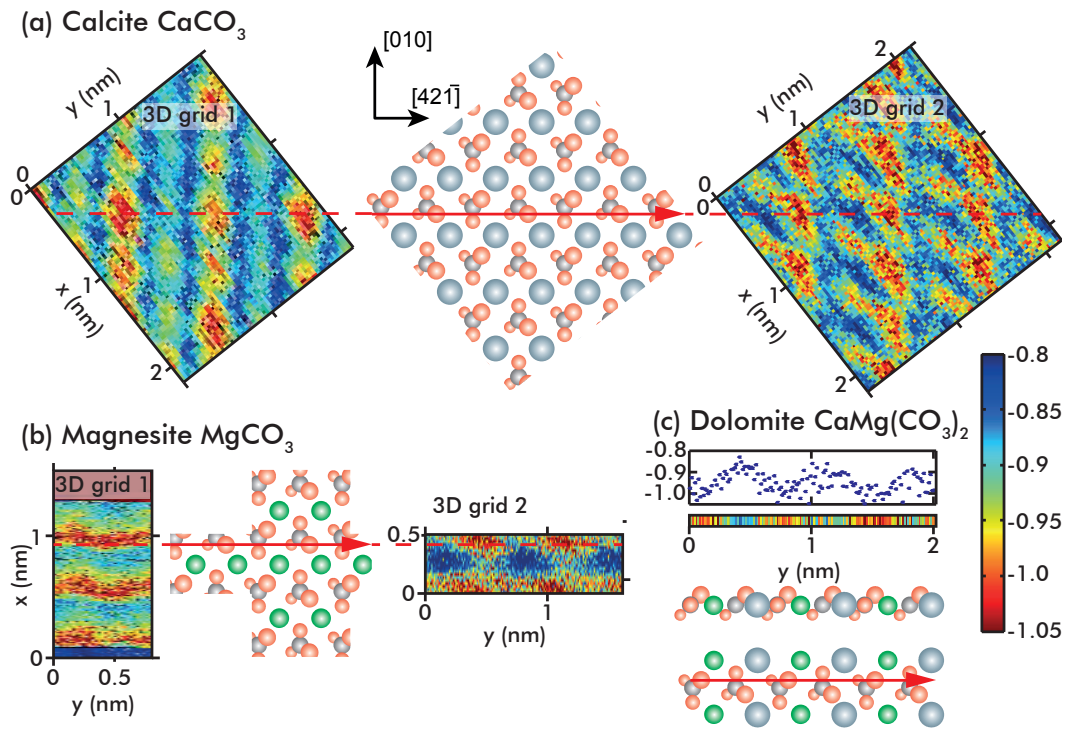


Fig. 6.10.: Normalised F_{\min} map for every available 3D force field on calcite and magnesite and the dolomite slice. (a) Calcite data, the rotated surface model in the middle matches the two maps on the left and the right. (b) Magnesite data with the surface model according to the F_{\min} maps. (c) Line profile and F_{\min} map for dolomite with the surface model beneath. The colour scale is valid for every F_{\min} map. All surfaces and force maps are rotated in such a way that the $[42\bar{1}]$ direction is pointing to the right.

Summary

Concluding, this thesis gives an extensive study of fundamental properties of the calcite $\text{CaCO}_3(10.4)$ and related mineral surfaces which becomes possible by not only using state-of-the-art non-contact atomic force microscopy, but mainly by the sophisticated and highly advanced force mapping technique. This measurement mode allows for a detailed understanding of different kinds of forces at the atomic scale and gives insight into atomistic processes. All measurements were executed at room temperature. As outlined in Chapter 2, this poses a severe problem since the thermal drift at these temperatures prevents a long-term data acquisition with the highest precision that was required for this work. The handling of the implemented home-built atom-tracking system led to the desired measurements of force fields with atomic resolution. An elaborate and highly flexible scan protocol ensured a reliable data acquisition.

However, the pure data acquisition does not result in a force map yet. This is caused by the fact that the measurement signal is a frequency shift Δf which at first has to be converted into force. The conversion of the raw Δf data into the vertical net force F_z is not a straightforward process: Several different approaches to do so are presented in literature, and it is important to find out which approach fits best to the experimental conditions. Chapter 3 gives a detailed description of how to correctly obtain the vertical force F_z for the conditions within this work. Data smoothing can be necessary but holds the potential to falsify the data. It was shown in an elaborate study that the combined use of Lanczos differentiators and Savitzky-Golay filters of a specific order allow for an effective smoothing of the raw F_z data without distorting significant values in F_z .

Besides the conversion into vertical force, a calculation of the potential landscape is possible from the acquired Δf data. The knowledge of the interaction potential allows for a further, at first not intuitive, calculation of the lateral forces F_y which states an additional channel for data analysis that is not accessible from standard imaging in NC-AFM. Lateral forces F_y allow for an even deeper insight into atomic scale mechanisms. Furthermore, dissipation data can yield useful information as well, therefore it is important to know how to rescale the dissipation raw data into useful, physical dimensions. With all this available, it is possible to access the full potential of every obtained force map.

With the vertical forces F_z available it is possible to extract the chemical short-range forces $F_{z,\text{SR}}$. Short-range forces give deepest insight into atomic scale mechanisms and are therefore of utmost interest. The extraction of $F_{z,\text{SR}}$, however, is a delicate and error-prone task, especially on substrates where an *on-minus-off* approach is not possible, for instance on bulk insulators like calcite. On such insulating substrates one has to rely on fitting the van der Waals interaction and subtract it from the experimentally obtained data. When performing this procedure one has to find a suitable model to describe the macroscopic tip shank and, more importantly, precisely find the cut-off position z_{cut} which states the transition from interaction of pure long-range nature to mixed interaction.

Chapter 4 describes how both obstacles were overcome within this thesis, namely by finding three independent criteria to determine z_{cut} : First, the point where the fit quality, determined by the mean-squared error (MSE), starts to increase; second, the position where the vertical forces F_z start deviating from each other and, third, the same criterion for the lateral forces F_y . In the latter two cases this is determined by the standard deviation $\sigma_{z,y}$.

An extensive error analysis confirms that by choosing the criterion for the deviation of F_y trustworthy short-range forces can be obtained. This is the first time that in an elaborate analysis a criterion was giving for reliably finding z_{cut} , complemented by a detailed error analysis. This analysis constitutes a guideline for extracting trustworthy short-range forces $F_{z,\text{SR}}$ on any sample surface.

With the knowledge of the short-range forces $F_{z,\text{SR}}$ and the lateral forces F_y it was possible to identify one of the fundamental properties of the investigated sample, the calcite $\text{CaCO}_3(10.4)$ surface: the absolute orientation. It is the orientation, the tilt, of the carbonate groups within the (10.4) surface that renders the $[4\bar{2}1]$ and the $[42\bar{1}]$ direction unequal, and it is this difference that is not distinguishable with standard NC-AFM imaging. Calcite, however, offers the unambiguous identification of the absolute orientation, namely macroscopically by optical means which allows for this work to always know the absolute orientation within the force field data.

Force maps have been acquired on calcite, and in the channels Δf , F_z , $F_{z,\text{SR}}$ and F_y a strong tilt of the imaged features is observable. This contrast can be correlated to the tilt of the carbonate groups, exactly determined by the optical method. Short-range and lateral forces show a tilted trajectory of the tip towards the CO_3^{2-} groups indicating the tips most favourable path along the potential landscape towards the surface. From these findings it can be concluded that at greater tip-to-sample distances the carbonate groups are imaged as a whole entity, while at decreasing separations the protruding oxygen is imaged. This would explain the tilted trajectory of the tip towards the surface.

Furthermore, a detailed analysis was shown on the recorded force maps on magnesite MgCO_3 and dolomite $\text{CaMg}(\text{CO}_3)_2$. Here the tilt of the carbonate groups is not

visible in the data. This is probably due to a specific and unknown tip configuration that resolves the tilt in a very small distance regime, only, which makes it impossible to see it in the data. Additionally, two approaches have been described aiming on the chemical identification of the cations Ca^{2+} and Mg^{2+} of the chosen substrates. Since a full 3D force map on dolomite could not be achieved, the final evidence is missing for clearly distinguishing between the different cations.

In conclusion, this thesis is a comprehensive study on the demanding force mapping technique, ranging from a detailed description on the data acquisition to the interpretation of the extracted forces, highlighted by the unravelling of a process at the atomic scale for contrast formation on the calcite $\text{CaCO}_3(10.4)$ surface. The force conversion, application of filters and, most importantly, the extraction of the short-range forces $F_{z,\text{SR}}$ serve as an instruction for anyone who is interested in these quantities. The microscopic determination of the absolute surface orientation and the revealed mechanism are of fundamental importance when discussing molecular adsorption or chirality of calcite which are in turn relevant aspects for biomineralisation.

Bibliography

- [1] L. Addadi, S. Weiner, *Angewandte Chemie-International Edition* **1992**, *31*, 153–169.
- [2] S. Hirano, T. Yogo, K. Kikuta, *Progress in Crystal Growth and Characterization of Materials* **1991**, *23*, 341–367.
- [3] E. Hadicke et al., *Physical Chemistry Chemical Physics* **1999**, *1*, 3891–3898.
- [4] J. Rieger, J. Thieme, C. Schmidt, *Langmuir* **2000**, *16*, 8300–8305.
- [5] H. Cölfen, *Current Opinion in Colloid Interface Science* **2003**, *8*, 23–31.
- [6] L. Addadi, S. Weiner, *Nature* **2001**, *411*, 753–755.
- [7] R. M. Hazen, T. R. Filley, G. A. Goodfriend, *Proceedings of the National Academy of Sciences* **2001**, *98*, 5487.
- [8] C. A. Orme et al., *Nature* **2001**, *411*, 775–779.
- [9] R. A. Berner, A. C. Lasaga, R. M. Garrels, *American Journal of Science* **1983**, *283*, 641–683.
- [10] R. S. Arvidson, F. T. Mackenzie, *American Journal of Science* **1999**, *299*, 257–288.
- [11] G. Binnig, C. Quate, C. Gerber, *Physical Review Letters* **1986**, *56*, 930–933.
- [12] F. J. Giessibl, *Science* **1995**, *267*, 68–71.
- [13] G. Binnig et al., *Physical Review Letters* **1982**, *49*, 57–61.
- [14] G. Meyer, N. M. Amer, *Applied Physics Letters* **1988**, *53*, 1045–1047.
- [15] T. R. Albrecht et al., *Journal of Applied Physics* **1991**, *69*, 668–673.
- [16] F. J. Giessibl, *Reviews of Modern Physics* **2003**, *75*, 949–983.
- [17] S. Rode, PhD thesis, Johannes Gutenberg-Universität, **2011**.
- [18] F. J. Giessibl, *Applied Physics Letters* **2001**, *78*, 123–125.
- [19] F. J. Giessibl, *Phys. Rev. B: Condens. Matter* **1997**, *56*, 16010–16015.
- [20] H. Hölscher et al., *Physical Review B* **2000**, *61*, 12678–12681.

- [21] S.-I. Kitamura, M. Iwatsuki, *Japanese Journal of Applied Physics Part 2: Letters* **1995**, *34*, L145–L148.
- [22] C. Barth et al., *Advanced Materials* **2011**, *23*, 477–501.
- [23] L. Gross et al., *Science* **2009**, *325*, 1110–1114.
- [24] F. J. Giessibl et al., *Science* **2000**, *289*, 422–425.
- [25] P. Rahe, PhD thesis, Johannes Gutenberg-Universität, **2011**.
- [26] P. Rahe et al., *Review of Scientific Instruments* **2011**, *82*, 063704.
- [27] J. E. Lennard-Jones, *Proceedings of the Physical Society* **1931**, *43*, 461–482.
- [28] M. Nonnenmacher, M. P. O’Boyle, H. K. Wickramasinghe, *Applied Physics Letters* **1991**, *58*, 2921–2923.
- [29] W. Melitz et al., *Surface Science Reports* **2011**, *66*, 1.
- [30] F. London, *Zeitschrift für Physik* **1930**, *63*, 245–279.
- [31] H. C. Hamaker, *Physica (The Hague)* **1937**, *4*, 1058.
- [32] C. Argento, R. H. French, *Journal of Applied Physics* **1996**, *80*, 6081–6090.
- [33] H. B. G. Casimir, D. Polder, *Physical Review* **1948**, *73*, 360–372.
- [34] J. N. Israelachvili, *Proceedings of the Royal Society of London. A. Mathematical and Physical Sciences* **1972**, *331*, 39.
- [35] D. Sarid, *Scanning Force Microscopy: With Applications to Electric, Magnetic, and Atomic Forces*, Oxford University Press, Cary, NC, USA, **1994**.
- [36] B. R. Holstein, *American Journal of Physics* **2001**, *69*, 441–449.
- [37] A. Šiber et al., *Phys. Rev. B* **2009**, *80*, 165414.
- [38] R. Perez et al., *Physical Review B* **1998**, *58*, 10835–10849.
- [39] S. I. Zanette et al., *Surface Science* **2000**, *453*, 75–82.
- [40] S. Kuhn, P. Rahe, *Physical Review B* **2014**, *89*, 235417.
- [41] L. Tröger et al., *Review of Scientific Instruments* **2009**, *80*, 063703.
- [42] H. Hölscher et al., *Applied Physics Letters* **2002**, *81*, 4428–4430.
- [43] B. J. Albers et al., *Nanotechnology* **2009**, *20*, 264002.
- [44] P. Rahe, R. Bechstein, A. Kühnle, *J. Vac. Sci. Technol. B* **2010**, *28*, C4E31–C4E38.
- [45] D. W. Pohl, R. Möller, *Review of Scientific Instruments* **1988**, *59*, 840–842.
- [46] B. S. Swartzentruber, *Physical Review Letters* **1996**, *76*, 459–62.
- [47] M. Krueger, B. Borovsky, E. Ganz, *Surface Science* **1997**, *385*, Times Cited: 36, 146–154.
- [48] E. Hill, B. Freelon, E. Ganz, *Physical Review B* **1999**, *60*, 15896–15900.

- [49] M. Abe et al., *Nanotechnology* **2005**, *16*, 3029–3034.
- [50] S. M. Langkat et al., *Surface Science* **2003**, *527*, 12–20.
- [51] A. Schwarz et al., *Scanning Tunneling Microscopy/Spectroscopy and Related Techniques: 12th International Conf.* **2003**, *696*, 68–78.
- [52] B. Such et al., *Nanotechnology* **2012**, *23*, 045705.
- [53] M. Z. Baykara et al., *Physical Review B* **2013**, *87*, 9.
- [54] M. Ashino et al., *Nanotechnology* **2009**, *20*, 264001.
- [55] D. A. Braun et al., *Nanotechnology* **2009**, *20*, 264004.
- [56] D. A. Braun et al., *Journal of Vacuum Science & Technology B* **2010**, *28*, C4B6–C4B11.
- [57] R. Pawlak et al., *Journal of Physics-Condensed Matter* **2012**, *24*.
- [58] C. Chiu et al., *Physical Review Letters* **2012**, *108*, 268302.
- [59] A. Schirmeisen, D. Weiner, H. Fuchs, *Physical Review Letters* **2006**, *97*, 136101–4.
- [60] K. Ruschmeier, A. Schirmeisen, R. Hoffmann, *Physical Review Letters* **2008**, *101*, 156102.
- [61] K. Ruschmeier, A. Schirmeisen, R. Hoffmann, *Nanotechnology* **2009**, *20*, 264013.
- [62] B. Such et al., *Journal of Vacuum Science & Technology B* **2010**, *28*, C4B1.
- [63] S. Kawai et al., *Physical Review B* **2011**, *83*, 035421.
- [64] S. Fremy et al., *Nanotechnology* **2012**, *23*, 055401.
- [65] M. Abe et al., *Applied Physics Letters* **2005**, *87*, 173503.
- [66] M. Heyde et al., *Nanotechnology* **2006**, *17*, S101–S106.
- [67] Y. Sugimoto et al., *Nature* **2007**, *446*, 64–67.
- [68] Y. Sugimoto et al., *Science* **2008**, *322*, 413.
- [69] M. Abe et al., *Applied Physics Letters* **2007**, *90*, 203103.
- [70] Y. Sugimoto et al., *Physical Review B* **2008**, *77*, 195424.
- [71] Y. Naitoh et al., *Physical Review Letters* **2012**, *109*, 5.
- [72] S. Kuhn et al., *Physical Review B* **2014**, *90*, 195405.
- [73] M. Heyde et al., *Applied Physics Letters* **2006**, *89*, 263107.
- [74] B. J. Albers et al., *Nature Nanotechnology* **2009**, *4*, 307–310.
- [75] A. M. Sweetman et al., *Nature Communications* **2014**, *5*, 7.
- [76] Y. Sugimoto et al., *Physical Review B* **2010**, *81*, 245322.
- [77] Y. Sugimoto et al., *Applied Physics Letters* **2010**, *96*, 263114.

- [78] R. Pawlak et al., *ACS nano* **2011**, *5*, 6349–6354.
- [79] T. Fukuma et al., *Physical Review Letters* **2010**, *104*, 016101.
- [80] C. Marutschke et al., *Nanotechnology* **2014**, *25*, 7.
- [81] M. Z. Baykara et al., *Beilstein Journal of Nanotechnology* **2012**, *3*, 637–650.
- [82] U. Dürig, *Appl. Phys. Lett.* **1999**, *75*, 433–435.
- [83] J. E. Sader, S. P. Jarvis, *Applied Physics Letters* **2004**, *84*, 1801–1803.
- [84] J. Welker, E. Illek, F. J. Giessibl, *Beilstein Journal of Nanotechnology* **2012**, *3*, 238–248.
- [85] J. Sader, S. Jarvis, Determination of Force and Energy vs Separation from Frequency vs Separation Data, <http://www.nanofunction.org/storage/resources-images/techniques/fm-afm/fmafmsader.nb>, **2004**.
- [86] G. H. Simon, M. Heyde, H. P. Rust, *Nanotechnology* **2007**, *18*.
- [87] A. Stannard, A. Sweetman, *Imaging and Manipulation of Adsorbates using Dynamic Force Microscopy. Advances in Atom and Single Molecule Machines, Vol. 4*, Springer, **submitted**.
- [88] J. Lübke et al., *Beilstein Journal of Nanotechnology* **2013**, *4*, 227–233.
- [89] S. Cook et al., *Nanotechnology* **2006**, *17*, 2135–2145.
- [90] J. L. Hutter, J. Bechhoefer, *Review of Scientific Instruments* **1993**, *64*, 1868–1873.
- [91] M. Ternes et al., *Science (Washington DC United States)* **2008**, *319*, 1066–1069.
- [92] G. Langewisch et al., *Physical Review Letters* **2013**, *110*, 5.
- [93] D. Rugar et al., *Nature* **2004**, *430*, 329–332.
- [94] S. Kawai et al., *Physical Review B* **2010**, *81*, 085420.
- [95] O. Pfeiffer et al., *Physical Review B* **2002**, *65*, 161403–161403.
- [96] P. M. Hoffmann et al., *Physical Review Letters* **2001**, *87*, 265502.
- [97] A. Schirmeisen, H. Holscher, *Physical Review B* **2005**, *72*, 5431.
- [98] S. Kawai et al., *Physical Review B* **2011**, *84*, 9.
- [99] G. Langewisch et al., *Small* **2012**, *8*, 602–611.
- [100] M. Lange, D. van Vorden, R. Moller, *Beilstein Journal of Nanotechnology* **2012**, *3*, 207–212.
- [101] S. Kawai et al., *Physical Review B* **2012**, *86*, 10.
- [102] C. Loppacher et al., *Physical Review B (Condensed Matter)* **2000**, *62*, 13674–9.
- [103] M. A. Lantz et al., *Science* **2001**, *291*, 2580–2583.

- [104] A. Yurtsever et al., *Physical Review B* **2012**, *85*, 125416.
- [105] N. Hauptmann et al., *New Journal of Physics* **2012**, *14*, 073032.
- [106] U. Hartmann, *Annual Review of Materials Science* **1999**, *29*, 53.
- [107] A. Sweetman, A. Stannard, *Beilstein Journal of Nanotechnology* **2014**, *5*, 386–393.
- [108] M. Ternes et al., *Physical Review Letters* **2011**, *106*, 016802.
- [109] P. Rahe, J. Schütte, A. Kühnle, *Journal of Physics-Condensed Matter* **2012**, *24*, 084006.
- [110] P. Sharp et al., *Applied Physics Letters* **2012**, *100*, 233120.
- [111] M. Guggisberg et al., *Physical Review B* **2000**, *61*, 11151–11155.
- [112] M. Saint Jean et al., *Journal of Applied Physics* **1999**, *86*, 5245–5248.
- [113] P. M. Morse, *Physical Review* **1929**, *34*, 57.
- [114] W. A. Hofer, A. S. Foster, A. L. Shluger, *Reviews of Modern Physics* **2003**, *75*, 1287.
- [115] G. H. Enevoldsen et al., *Physical Review B* **2008**, *78*, 045416.
- [116] C. Barth et al., *Journal of Physics-Condensed Matter* **2001**, *13*, 2061–2079.
- [117] G. Teobaldi et al., *Physical Review Letters* **2011**, *106*, 216102.
- [118] L. Olsson et al., *Journal of Applied Physics* **1998**, *84*, 4060.
- [119] R. Hoffmann et al., *Applied Surface Science* **2002**, *188*, 238.
- [120] R. Hoffmann et al., *Physical Review Letters* **2004**, *92*, 146103.
- [121] L. Bergström, *Advances in Colloid and Interface Science* **1997**, *70*, 125–169.
- [122] R. French et al., *Solid State Ionics* **1995**, *75*, 13–33.
- [123] S. C. Fain et al., *Nanotechnology* **2006**, *17*, S121.
- [124] W. A. Deer, R. A. Howie, J. Zussman, *An introduction to the rock forming minerals*, Pearson Education Limited, **1992**.
- [125] *Carbonates: mineralogy and chemistry*, (Ed.: R. J. Reeder).
- [126] D. R. Baer, D. L. Blanchard, *Applied Surface Science* **1993**, *72*, 295–300.
- [127] J. W. Gifford, *Proceedings of the Royal Society of London* **1902**, *70*, 329–340.
- [128] J. O. Titiloye, N. H. de Leeuw, S. C. Parker, *Geochimica Et Cosmochimica Acta* **1998**, *62*, 2637–2641.
- [129] S. C. Parker et al., *Faraday Discussions* **2003**, *124*, 155–170.
- [130] R. Kristensen, S. L. S. Stipp, K. Refson, *Journal of Chemical Physics* **2004**, *121*, 8511–8523.
- [131] M. Bruno et al., *Crystal Engineering Communications* **2010**, *12*, 3626–3633.

- [132] H. Effenberger, K. Mereiter, J. Zemann, *Zeitschrift Für Kristallographie* **1981**, 156, 233.
- [133] P. Rahe, S. Kuhn, A. Kühnle, *Journal of Unsolved Questions* **2013**, 3, 21.
- [134] A. L. Rachlin, G. S. Henderson, M. C. Goh, *American Mineralogist* **1992**, 77, 904–10.
- [135] S. L. Stipp, M. F. Hochella, *Geochimica Et Cosmochimica Acta* **1991**, 55, 1723–1736.
- [136] J. Schütte et al., *Langmuir* **2010**, 26, 8295–8300.
- [137] S. Kawai et al., *Nanotechnology* **2013**, 24, 055702.
- [138] G. H. Simon et al., *Physical Review B* **2008**, 78, 113401–4.
- [139] C. Barth, M. Reichling, *Nature* **2001**, 414, 54–57.
- [140] P. Rahe et al., *Advanced Materials* **2013**, 25, 3948.
- [141] J. V. Barth, G. Costantini, K. Kern, *Nature (London United Kingdom)* **2005**, 437, 671–679.
- [142] L. Gross, *Nature Chemistry* **2011**, 3, 273–278.
- [143] A. S. Foster, A. L. Shluger, R. M. Nieminen, *Applied Surface Science* **2002**, 188, 306–318.
- [144] R. Bennewitz et al., *Surface Science* **2001**, 474, L197–L202.
- [145] A. S. Foster et al., *Applied Surface Science* **2003**, 210, 146–152.
- [146] Y. Liang et al., *Surface Science* **1996**, 351, 172–82.
- [147] A. J. Weymouth, T. Hofmann, F. Giessibl, *Science* **2014**, 343, 1120.
- [148] S. Kuhn, Diploma thesis, Johannes Gutenberg-Universität, **2012**.

Parameter dependency of fit models

We investigated for each fit model possible dependencies between the fit parameters. In case of F_{1b} , F_{4a} and F_{4b} , two fit parameters are clearly dependent on each other due to their multiplicative appearance in the force law: HR can be formulated in a single parameter in case of F_{1b} and $H \tan(\theta)^2$ reduces to a single parameter in case of F_{4a} and F_{4b} .

For all other formulae, parameter dependencies are not necessarily directly apparent from the equations. We used a practical two-step approach. First, we evaluate the fit and observe the confidence intervals for all parameters. For dependent parameters, the intervals are expected to be large. In this case, we calculate in a second step the zero and minimum position of the resulting short-range force curve for several cases, having a single parameter fixed in each. If a single parameter is dependent on others, the resulting fit is expected to be virtually identical over a large range for the fixed parameter while the other parameters adjust accordingly to yield the same fit result.

For F_1 we find very large confidence intervals when leaving all fit parameters free. Thus, the parameters are not independent from each other. Fixing the Hamaker constant H gives unreasonable large radii for the tip in the order from several hundred nm up to μm . Since this formula does not consider the tip shank, a large tip seems to compensate for the missing shank. Even for optimum fits, the MSE is still an order of magnitude larger than for other formulae. Fixing R yields fits similar to the one shown in Fig. 4.6(a), but the resulting short-range forces are purely attractive and, consequently, no z_{zero} exists. Only for the unrealistic case of $R < 1$ nm, a zero position is found. Based on these findings, we decided not to choose this model for fitting.

Formulae F_2 and F_3 are discussed together, since both formulae describe a similar geometry and yield nearly identical results as can be seen in Figs. 4.4 to 4.6 and Table 4.1. Fitting these formulae to our experimental data results in large confidence intervals for H and R , pointing to a dependency between these parameters. We investigate the fit quality when fixing either of them by evaluating the position of the force zero and the MSE. Results are presented in Fig. A.1 and clearly show a robust fit when choosing R as a fixed value. In contrast, the minimum position and the fit quality change severely when fixing H . A similar behaviour of highly reduced

fit quality and varying z_{zero} is observed when setting θ or z_{off} to fixed values (not shown). Thus, constraining the latter three parameters is not justified.

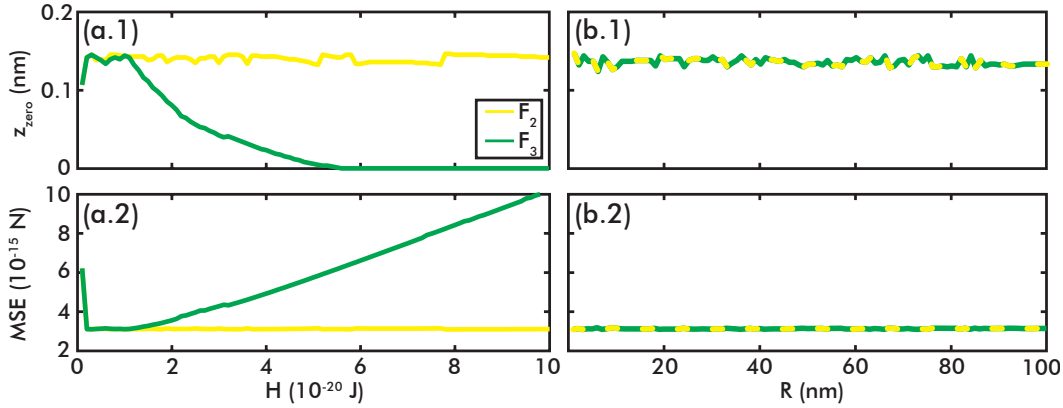


Fig. A.1.: Force laws F_2 and F_3 . Position z_{zero} of force zero (a.1), (b.1) and fit quality MSE (a.2), (b.2) when fixing the parameters H (a panels) or R (b panels).

Fitting F_5 with all parameters as fit variables results in large confidence intervals for H and L . For the data given herein, we found that removing either H , L or θ as a free fit parameter is a justified approach. Fixing either of these values result in the same fit quality and the same zero position within a small error, see Fig. A.2. It should be noted, however, that $\theta > 20^\circ$ is required for this conclusion.

The resulting confidence intervals of the parameters when fitting F_{6b} with all parameters free are large. We found that removing R as a free parameter and setting it to reasonable values does have a severe influence neither on the fit quality, nor on the resulting zero and minimum positions as shown in Fig. A.3(a). In contrast, fixing any other parameter (H , h_1 , θ , z_{off}) results in a dependency of the fit and fit quality on the parameter value. We exemplarily present the analysis for a fixed Hamaker constant H in Fig. A.3(a) additional to the case of fixed R in panel (b).

Based on this analysis, we chose to remove and fix parameters from the force models as listed in Table A.1.

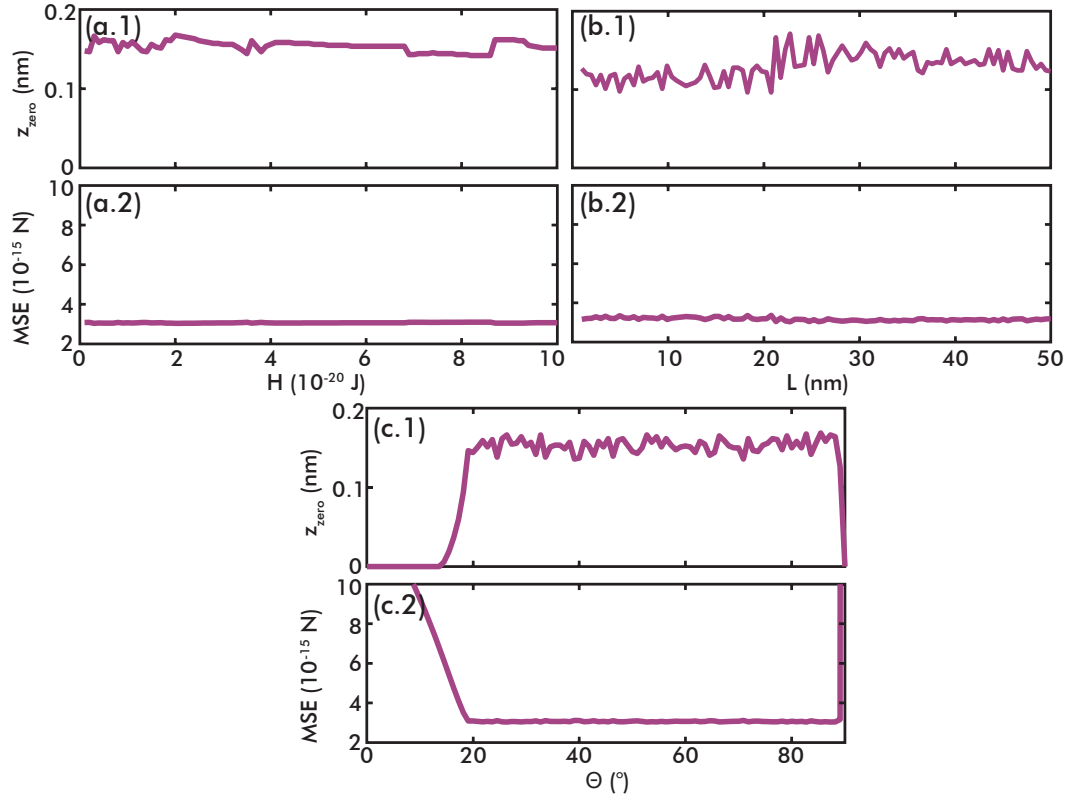


Fig. A.2.: Force law F_5 . Position z_{zero} of force zero (a.1), (b.1), (c.1) and fit quality MSE (a.2), (b.2), (b.3) when fixing parameters H (a panel), L (b panel) or θ (c panel).

Tab. A.1.: Parameters held fixed in the model evaluation and fit due to dependencies within the fit parameters of each model.

model	fixed parameter
F_1	$R_{\text{fix}} = 25$ nm
F_{1b}	$R_{\text{fix}} = 25$ nm
F_2	$R_{\text{fix}} = 25$ nm
F_3	$R_{\text{fix}} = 25$ nm
F_{4a}	$H_{\text{fix}} = 1 \times 10^{-20}$ J
F_{4b}	$H_{\text{fix}} = 1 \times 10^{-20}$ J
F_5	$L_{\text{fix}} = 5$ nm
F_{6b}	$R_{\text{fix}} = 25$ nm

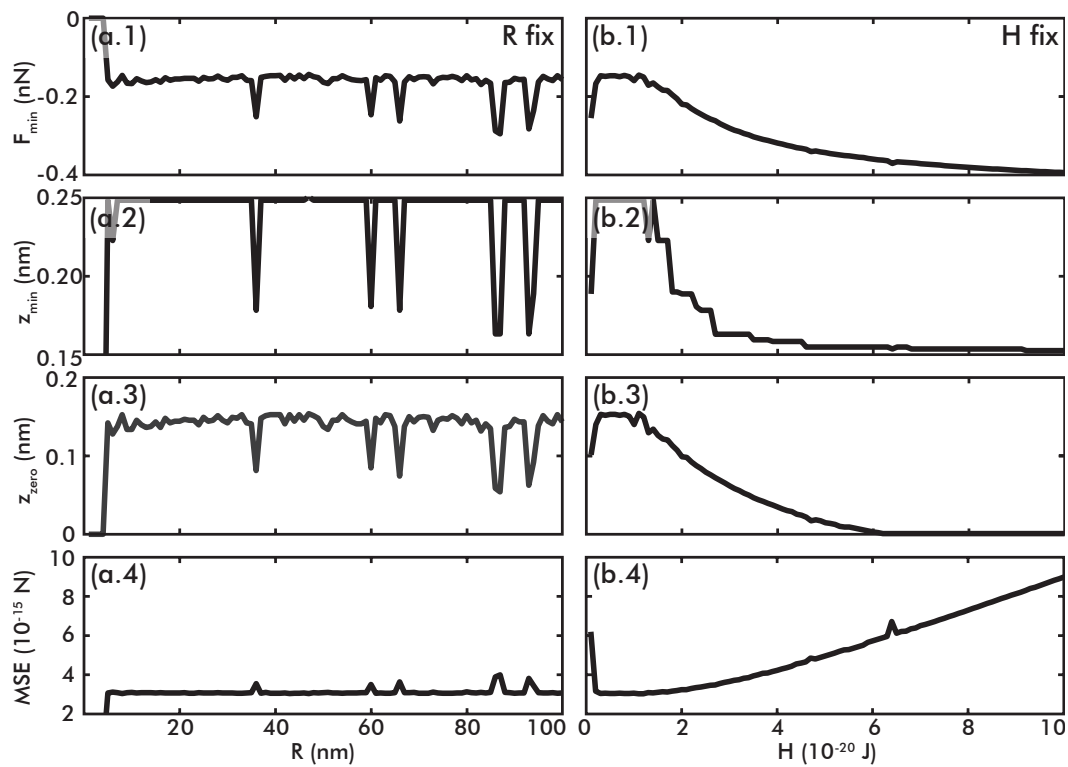


Fig. A.3.: Force law f_{6b} . Magnitude F_{\min} (a.1), (b.1) and position z_{\min} (a.2), (b.2) of the force minimum, position z_{zero} (a.3), (b.3) of force zero and fit quality MSE (a.4), (b.4) when fixing parameters R (a panels) or H (b panels)

Supplementary data for 2D force slice and additional datasets

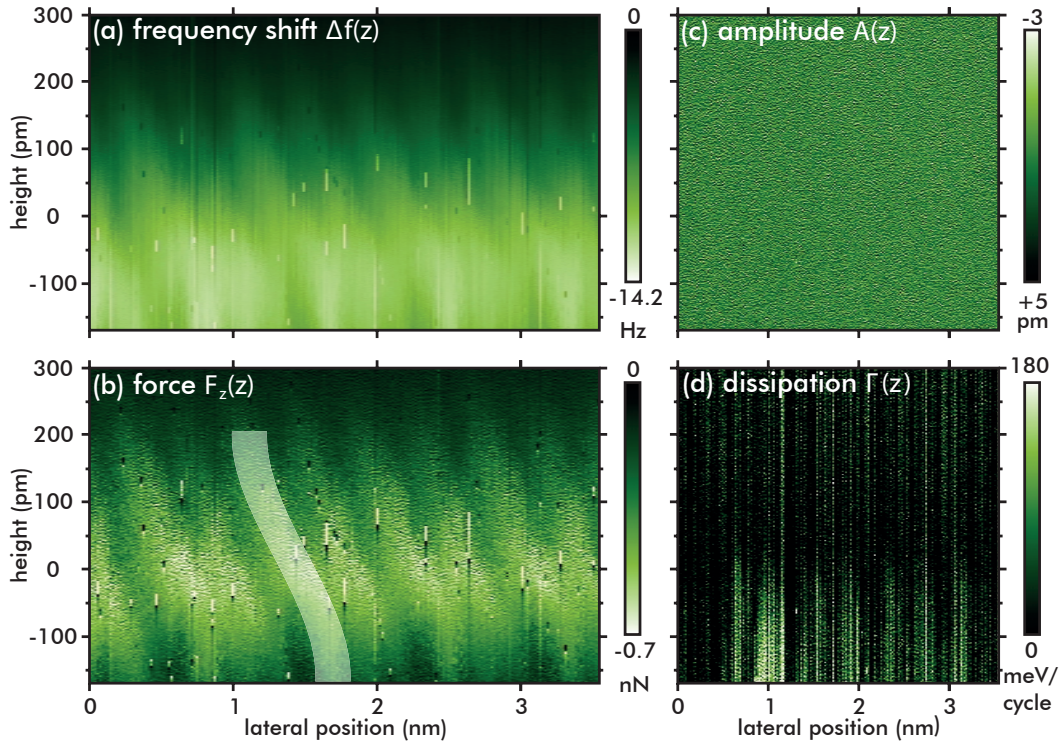


Fig. B.1.: (a) Frequency shift Δf , (b) vertical total force interaction F_z , (c) amplitude A and (d) dissipation Γ data. The data are represented with a stretched vertical axis for better representation.

All measurement channels for the data presented in Fig. 6.3 and Fig. 6.5 of Section 6.1 are reproduced in Fig. B.1. No site-specific contrast is apparent in the amplitude data shown in Fig. B.1(c), instead we find pure white noise with $\sigma = 1.5$ pm. With the amplitude constant to better than 0.01 % we find that the Sader-Jarvis force recovery strategy given in Eq. (3.2) is fully justified. A small site-specific contrast is observed in the dissipation $\Gamma(z)$ data in Fig. B.1(d). These data were converted into units of eV/cycle using Eq. (3.15), as described in Section 3.4 and used in [99]. In our dataset, the dissipative contribution raises to a maximum of around 180 meV/cycle at very close tip-to-sample distances. We find the largest dissipation within this dataset next to the identified point defect, as indicated in Fig. B.1(a) and (b) by a dashed yellow circle. It is noteworthy that although we measure a dissipative interaction, no change is apparent in the amplitude.

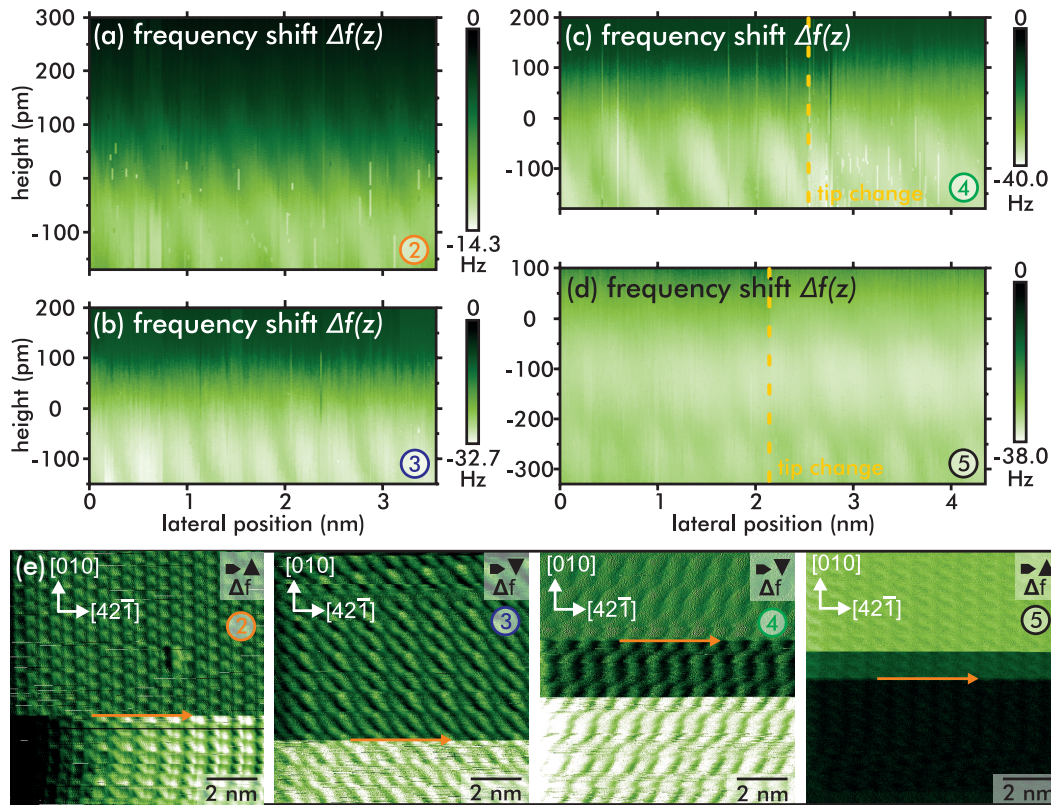


Fig. B.2.: Frequency shift raw data on calcite, presenting the tilt along the same direction. All data aligned along the $[42\bar{1}]$ direction and cropped along Z only depicting the relevant short-range part. Experimental sizes (Z \times Y): (a) $1.17 \times 3.48 \text{ nm}^2$ and 1000×201 pixels, (b) $1.15 \times 4.35 \text{ nm}^2$ and 1000×301 pixels (this dataset is also cropped along X), (c) $1.18 \times 4.35 \text{ nm}^2$ and 1000×301 pixels, (d) $1.33 \times 4.35 \text{ nm}^2$ and 1000×361 pixels. Datasets are presented stretched along the vertical axis. In (c) and (d), tip changes occurred at the positions indicated by a yellow dashed line. (e) XY scanned Δf -images prior and subsequent to the force field measurement. The orange arrow indicates the position and direction of the ZY data acquisition. All images are $10 \times 10 \text{ nm}^2$ and represent Δf raw data.

We provide further evidence that it is the calcite surface and not the tip which is the source for the observed asymmetric tilt in our data by repeating the experiment under different tip and sample conditions. Four ZY slices representing four different contrast modes are presented in Fig. B.2 (frequency shift Δf) and in Fig. B.3 (total force F_z). For all presented data, the absolute orientation for different crystals is determined by the macroscopic optical method (see Section 6.1.3) as marked by arrows. We find the same tilt direction in all of these F_z and also Δf data sets.

The contrast in Fig. B.2(a) is similar to Fig. 6.3, including a similar tilt shape and direction. The data in cB.2(b) presents a different contrast mode, a different total interaction force and a different tilt shape, but leaves the tilt orientation itself unchanged. Especially, the features imaged most attractive (“bright”) appear pairwise closer, which is known as the row-pairing reconstruction [109, 134]. In the data reproduced in Fig. B.2(c), an extreme variant of the row-pairing reconstruction is apparent, where the two bright features completely join into a single one. This

mode has been observed in plain XY imaging earlier [109]. However, even for this distinctly different contrast mode, the tilt exhibits the very same orientation as indicated in Fig. B.2(c). Another striking finding is the fact that the tilt orientation is even retained after the tip change occurring halfway in the data set (marked by an orange dashed line in Fig. B.2(c)). The fourth data set in Fig. B.3(d) presents the most complex interaction mode of the herein discussed data. At a height of $z \sim -100$ pm, the extreme row-pairing is apparent while the individual species are again resolved at closer tip-to-sample distances. Even as this change in contrast is explained by a complex tip apex structure, the tilt orientation remains the same as observed in all data before.

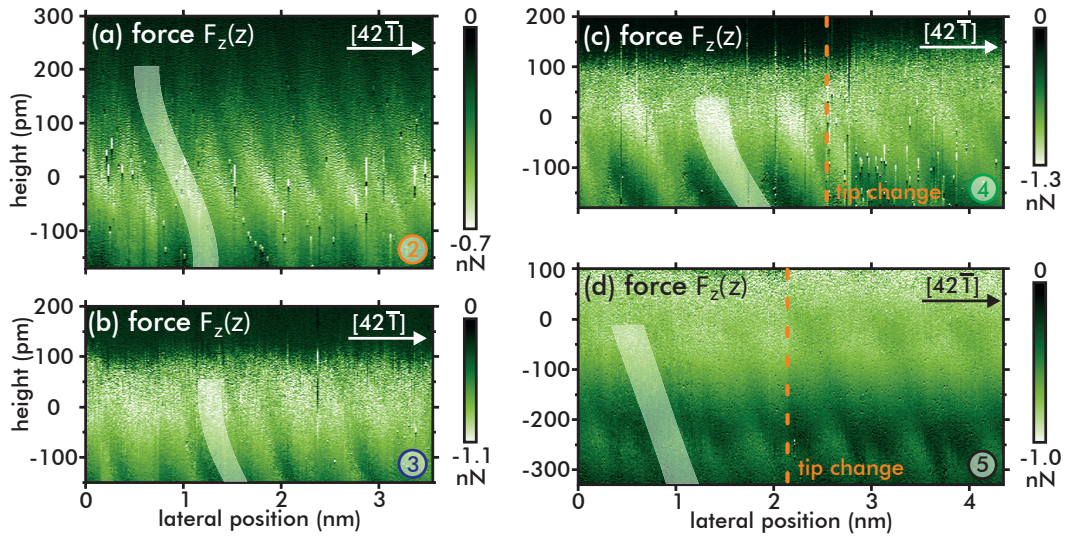


Fig. B.3.: ZY slices on calcite(10.4) representing different contrast modes. All data are aligned along the $[42\bar{1}]$ direction as indicated and are cropped along z to depict the relevant part. Experimental sizes as in Fig. B.2. Datasets are presented stretched along the vertical axis. In (c) and (d), tip changes occurred at the positions indicated by an orange dashed line.

All F_z data presented in Fig. B.3(a) to (d) are aligned with the $[42\bar{1}]$ direction pointing to the right as indicated. In each of these measurements, the imaging contrast modes, the total vertical interaction forces as well as the shapes of the tilt differ slightly. We ascribe these differences to different tip apex configurations. However, even with different tip terminations we clearly observe the exact same tilt orientation in all slices and in Fig. B.3.

To compare the datasets, we set the zero point in z -direction arbitrarily to the force minimum of each dataset. The averaged frequency shift and total vertical interaction force curves $\overline{F_z}$, for each of the five data sets presented in this work are shown in Fig. B.4(a) and (b), respectively, and are offset for clarity. For all data sets, the maximum attractive force is roughly about -1.0 nN.

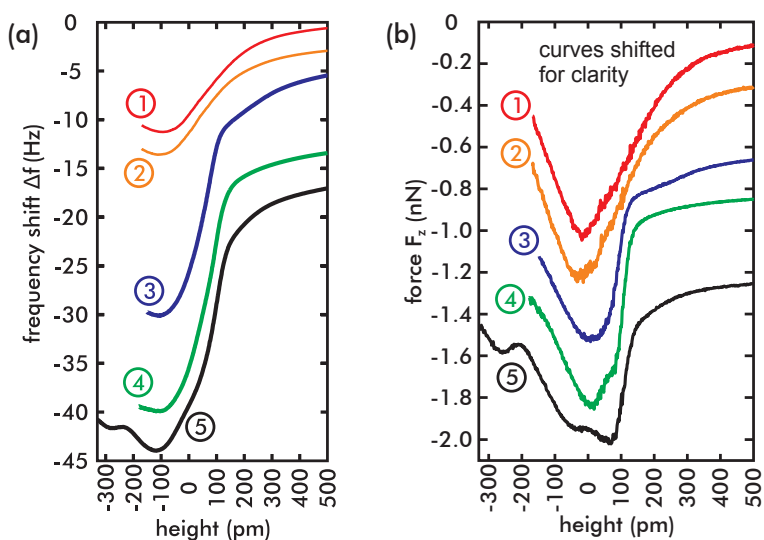


Fig. B.4.: (a) The average vertical frequency shift curves from the data in Fig. B.2. (b) The average vertical interaction force curves from the data in Fig. B.3. Curves are offset for clarity and aligned along Z to match the minimum positions in both Δf and F_z .

Besides the datasets along the $[42\bar{1}]$ direction, I acquired a further set of five 2D ZX force maps on calcite along the $[010]$ direction. In all cases the 2D force maps along $[42\bar{1}]$ and $[010]$ were acquired consecutively with the same tip and using the same reference position for tracking to allow for comparability of the force maps of the two surface directions. The two force maps along $[42\bar{1}]$ and $[010]$ for each set intersect each other in the middle. Consequently, the $[010]$ dataset share the same XY scan image before and after the force field measurement as the datasets along $[42\bar{1}]$, which are shown in Fig. B.2(e). The $[010]$ datasets are presented in Fig. B.5 and are numbered from one to five, where the colour code indicates the associated force map along $[42\bar{1}]$ from Fig. B.3.

The contrasts for these slices are comparable to the contrasts of the $[42\bar{1}]$ force fields from Fig. B.3. It is immediately visible, that the same tilt along the vertical Z axis is apparent along this surface direction as it is perpendicular to it. The data in Fig. B.5 show, that the observed tilt remains in the same surface direction for all the different tips, as the half-transparent guide to the eye indicates, which is in agreement with the earlier presented from Fig. B.3. It shall be stressed here, that for the force fields from Fig. B.5 (c) and (e) not the $[010]$ direction is pointing to the right, but its inverse, the $[0\bar{1}0]$ direction. Therefore, the direction of the tilt is the same for all the presented data herein.

As stated above in Section 6.2, I additionally acquired ZX force fields along the $[010]$ direction for magnesite and dolomite. For MgCO_3 there is one 2D slice available as

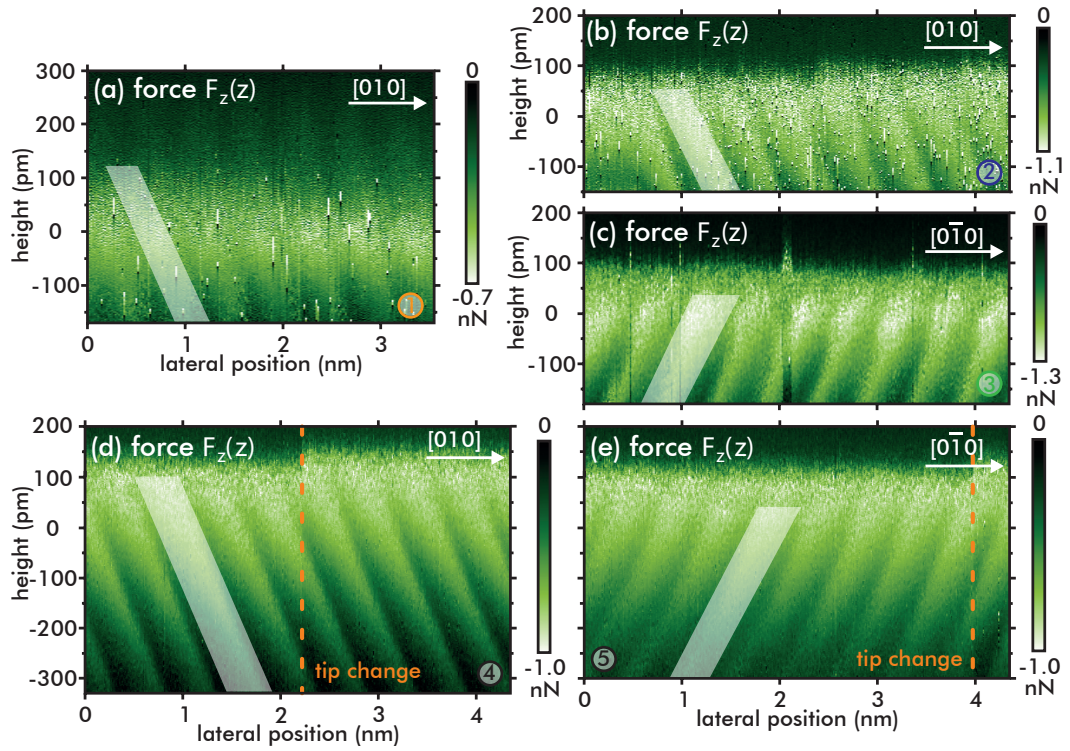


Fig. B.5.: ZX slices on calcite(10.4) representing different contrast modes. All data are aligned along the $[010]$ direction as indicated and are cropped along z to depict the relevant part. Experimental sizes ($Z \times X$): (a) $1.17 \times 3.48 \text{ nm}^2$ and 1000×201 pixels, (b) $1.15 \times 4.35 \text{ nm}^2$ and 1000×301 pixels (this dataset is also cropped along X), (c) $1.18 \times 4.35 \text{ nm}^2$ and 1000×301 pixels, (d) $1.33 \times 4.35 \text{ nm}^2$ and 1000×361 pixels, (e) $1.3 \times 4.35 \text{ nm}^2$ and 1000×361 pixels. Datasets are presented stretched along the vertical axis. In (d) and (e), tip changes occurred at the positions indicated by an orange dashed line.

well as a full 3D force map with the resolution greatly enhanced along $[010]$, as was introduced in Section 6.2. The data are presented in Fig. B.6.

The XY scan images before and after the force field measurement are the same as presented in Fig. 6.7(d). The 3D force map has physical dimensions of $1.69 \times 0.87 \times 1.2 \text{ nm}^3$ with a total of $152 \times 31 \times 1000$ pixel and, thus, covers more than three unit cells along the $[010]$ direction, but due to a tip change, marked in Fig. B.6, around two and a half unit cell remain for data analysis. The ZX slice in Fig. B.6 (d) has the dimensions $2.175 \times 1.2 \text{ nm}^2$ with 365×1000 pixel. It covers over four unit cells along this surface direction.

The same observations as described for the data along $[42\bar{1}]$ above in Section 6.2.1 also hold true for the presented data here. Contrary to calcite, only one bright species is imaged within every unit cell. Furthermore, a tilt along the vertical axis Z can neither be observed along the $[42\bar{1}]$ nor the $[010]$ direction.

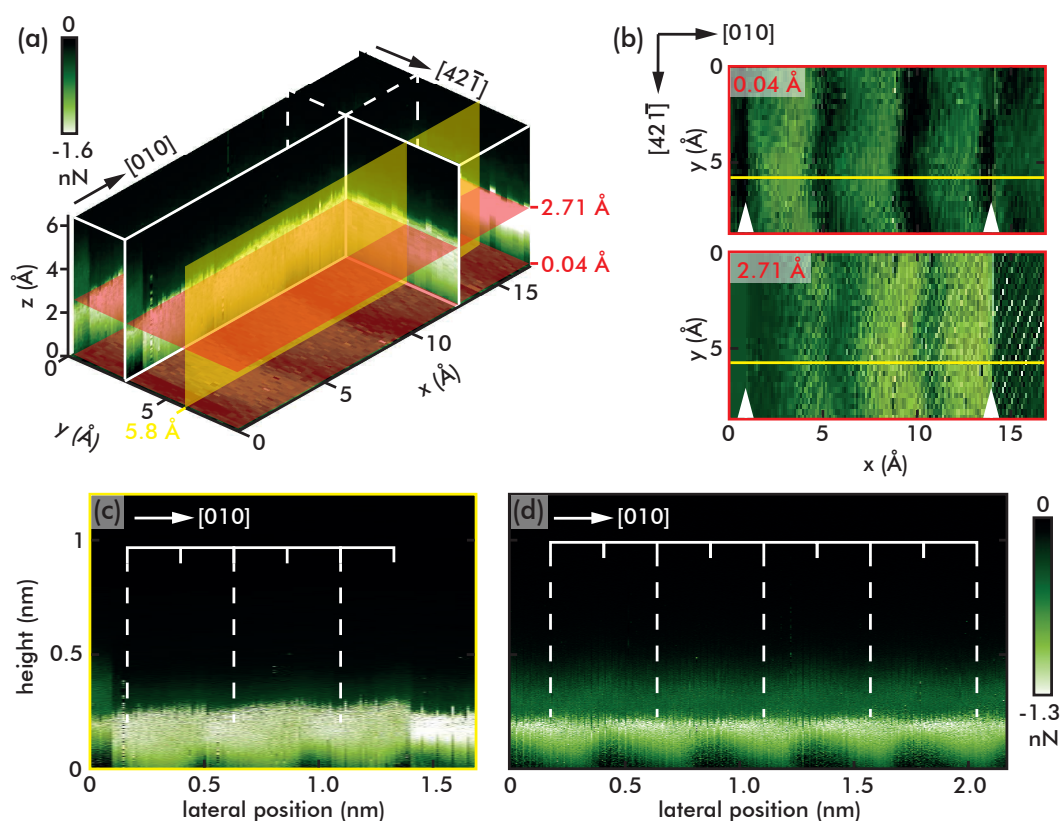


Fig. B.6.: Force maps on magnesite, aligned along the $[010]$ direction as indicated. (a) Representation of the 3D force map dense along the $[010]$ direction. Dimensions are $1.69 \times 0.87 \times 1.2 \text{ nm}^3$ with a total of $152 \times 31 \times 1000$ pixel. The red (yellow) shaded areas indicate extracted XY (ZX) intersections. (b) XY intersections from different heights, extracted from (a). The yellow line shows the position of the ZX slice, the white arrows point to tip changes. (c) ZX slice at the position marked in (a). (d) 2D force field with dimensions of $2.175 \times 1.2 \text{ nm}^2$ and 365×1000 pixel. For (c) and (d) the unit cell periodicity is marked by the dashed lines, the colour scale holds true for both slices.

Besides the earlier described force field on dolomite Section 6.2.2, I recorded another 2D slice on this substrate along the $[010]$ direction. This is the only other force map that is available for dolomite and it is shown in Fig. B.7.

The XY scan before and after the ZX slice is shown in the inset of Fig. 6.9(a), since I acquired this force field directly before the slice along $[42\bar{1}]$. The dimensions are $1.74 \times 1.2 \text{ nm}^2$ with a total of 155×1000 pixel. Therefore, the ZX slice covers at least three unit cells along the $[010]$ direction. From Fig. B.7 a slight lateral shift of the imaged species to the left is visible from the point on where the tip change occurred. This becomes apparent when closely inspecting the indicated unit cell periodicity. Again, as described for the $[42\bar{1}]$ slice, no tilt of the imaged species is observable.

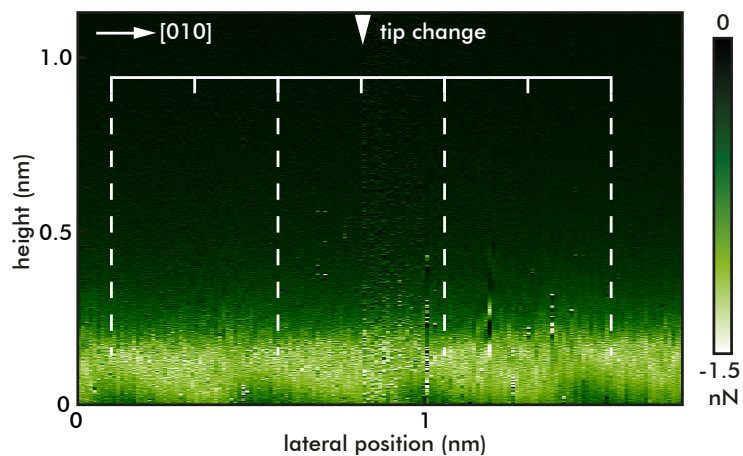


Fig. B.7.: ZX slice on dolomite, aligned along the [010] direction as indicated. Dimensions are $1.74 \times 1.2 \text{ nm}^2$ with a total of 155×1000 pixel. The unit cell periodicity is marked by the dashed lines, the white arrow indicates a tip change.

Details on the short-range force extraction for the magnesite data

The relevant details when I extracted the short-range forces $F_{z,SR}$ on magnesite are described here, following the exact same procedure as described in Chapter 4. As was shown earlier for determining the cut-off z_{cut} , it is necessary to inspect the mean-squared error (MSE) of the conducted fit for each of the given models (see Fig. 4.3) to the experimental data and the standard deviations of the vertical and lateral forces σ_z and σ_y . From the MSE plot the model to use can be determined.

Figure C.1 compiles this data for the 3D dataset dense along the $[42\bar{1}]$ direction which is discussed in Section 6.2.1. It shall be noted here that I inspected the data in detail regarding the two tip changes during the data acquisition and whether the mean curves $\overline{F_z}$ for the respective regions do affect the determination of z_{cut} . I found that fitting to the overall $\overline{F_z}$ curve of the whole dataset gives the same result for finding z_{cut} and the tip model as for the $\overline{F_z}$ curve of the individual regions. This is not surprising since tip changes should alter the microscopic tip and therefore the contrast observed, rather than the macroscopic tip shank. So fitting the macroscopic tip should give the same result even after a tip change. Consequently, the $\overline{F_z}$ curve for the whole dataset was used and is shown in Fig. C.1(d).

The best model turned out to be the flat pyramid with a spherical cap, model F_{6b} . The MSE plot is given in Fig. C.1(a) with a model of the tip in the inset. The cut-off is found in the minimum of this curve at 5.8 \AA . The σ_z and σ_y plots are shown in Fig. C.1(b) and (c), respectively, with cut-offs of 6.8 \AA and 6.9 \AA . The resulting fit using the z_{cut} of the σ_y criterion is presented in Fig. C.1(d).

Fit parameters were found to be $H = 9.15 \times 10^{-20} \text{ J}$, $\Theta = 5.29^\circ$, $h_1 = 1.36 \text{ nm}$, $L = 8.15 \text{ nm}$ and $z_{off} = 0.15 \text{ nm}$ with the radius R fixed to 25 nm . The low half-opening angle of $\Theta = 5.3^\circ$ seems surprising at first, but after closer inspecting the model F_{6b} one will find that an angle of 0° will result in a cuboid with base length L , still resulting in a possible model for the tip. For other models, such as F_2 , an angle of 0° is not realistic since this would reduce the tip to a sphere as is evident from inserting $\Theta = 0^\circ$ into Eq. (4.6). The result is the formula for model F_{1b} , see Eq. (4.5). This is not the case for model F_{6b} . Further confidence in the conducted fit is given by the fact, that the confidence intervals for this specific fit were overall very small as

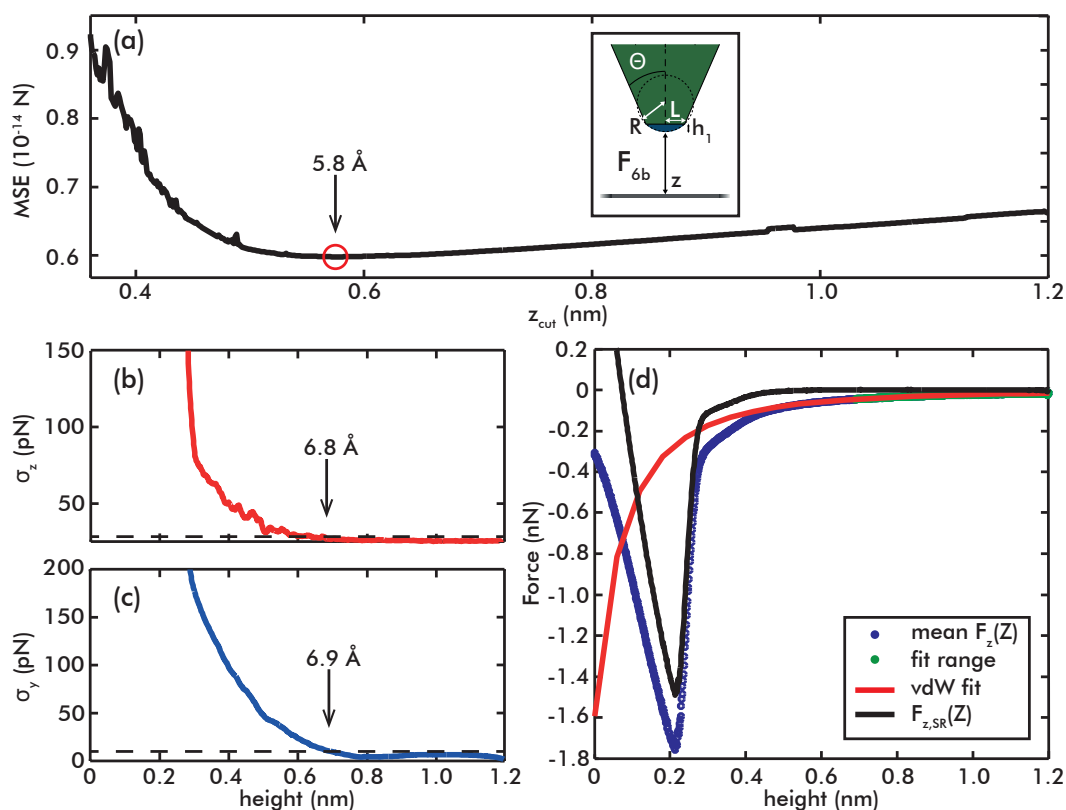


Fig. C.1.: $F_{z,SR}$ extraction of the 3D dataset on magnesite. (a) Fit quality expressed as the mean squared error (MSE) from fitting a van der Waals model to the mean experimental curve as a function of the lower fit range z_{cut} . The used model is presented in the inset. (b) Standard deviation σ_z of the vertical force F_z . (c) Standard deviation σ_y of the lateral force F_y . Resulting cut-off points are marked in both panels. (d) Mean total vertical interaction force $\overline{F_z}$ (blue), van der Waals interaction force F_{vdW} (red) and resulting mean vertical short-range force $\overline{F_{z,SR}}$

well as the errors.

In the following, the short-range force that I extracted for the two 2D slices shall be discussed, as were presented in Fig. 6.7(e) and (f). For both grids the mean $\overline{F_z}$ curve is roughly the same, and an analysis of both datasets showed that in both cases the same fit can be applied. For clarities' sake, Fig. C.2 shows the relevant data for one of the two datasets.

As is apparent from Fig. C.2(a) three models yielded good results for the fit, namely F_2 , F_3 and F_5 . Because models F_2 and F_3 gave the same result they are treated the same. Therefore, I only consider model F_3 in the following discussion. For model F_5 the z_{cut} was determined to 5.2 \AA , while for model F_3 z_{cut} is 5.7 \AA from the fit quality criterion. The vertical and lateral standard deviations in Fig. C.2(b) and (c) yield a z_{cut} of 6.0 \AA and 6.2 \AA , respectively. The two resulting fits for models F_3 (red dashed line) and F_5 (red solid line) with the z_{cut} from the σ_y criterion are given

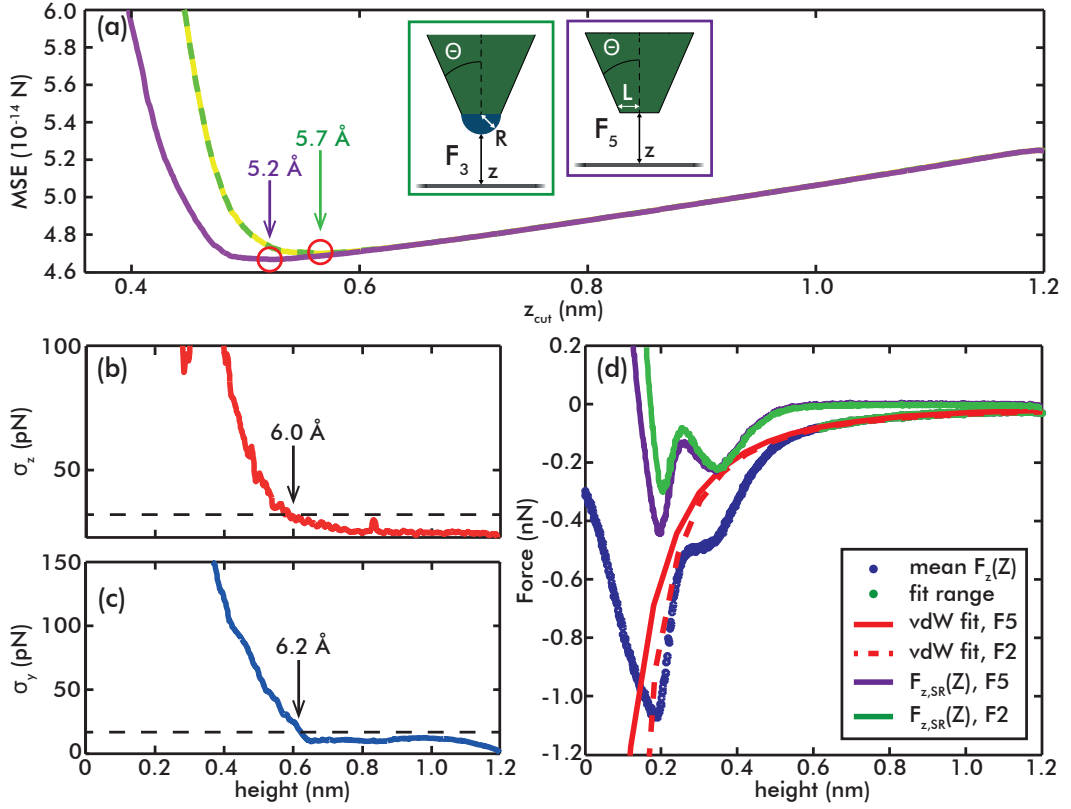


Fig. C.2.: $F_{z,SR}$ extraction of the 2D dataset on magnesite. (a) Mean squared error (MSE) from fitting a van der Waals model to the mean experimental curve as a function of z_{cut} . Two models are possible, so both MSE curves are shown, including the models in the inset. (b) Standard deviation σ_z of the vertical force F_z . (c) Standard deviation σ_y of the lateral force F_y . Resulting cut-off points are marked in both panels. (d) Mean total vertical interaction force $\overline{F_z}$ (blue), van der Waals interaction force F_{vdW} (solid and dashed red) and resulting mean vertical short-range force $\overline{F_{z,SR}}$ for the two models.

in Fig. C.2(d) with the respective resulting short-range forces.

For the model F_3 the fit parameters were determined to $H = 7.06 \times 10^{-20}$ J, $\Theta = 66.9^\circ$ and $z_{off} = 0$ nm with fixed R of 25 nm. Most striking is the z_{offset} of 0 nm indicating a microscopic tip with 0 nm height. In that case the part of the tip that is responsible for atomic resolution is located within the macroscopic tip shank. This might seem unusual but is still possible, therefore this model has to be taken into account as a reasonable possibility for the fit.

When using model F_5 the resulting fit parameters are $H = 4.62 \times 10^{-20}$ J, $\Theta = 69.9^\circ$ and $z_{off} = 0.18$ nm with fixed L of 5 nm. Here all the fit parameters are within the expected range and give a plausible model for the tip. Since for both models F_3 and F_5 realistic tip models are obtained and the confidence intervals for the fit are equally low, it can not be determined which of the two models is superior. Consequently, both have to be considered. When discussing the data in Section 6.2.1 the fit for model F_5 is presented since for this model all fit parameters were in the expected range. The data analysis described in Sections 6.2.1 and 6.3, however, was

conducted with both models. Since the interpretation and the outcome, however, did not change the shown data are restricted to the case of fitting model F_5 , only.

Details on the short-range force extraction for the dolomite data

Analogue to the magnesite data in Appendix C, I describe the extraction of $F_{z,SR}$ for dolomite here. Consequently, Fig. D.1 presents the fit quality in terms of the mean-squared error MSE in panel (a), the vertical and lateral standard deviations σ_z and σ_y in panels (b) and (c) and the final fit using the σ_y criterion in panel (d).

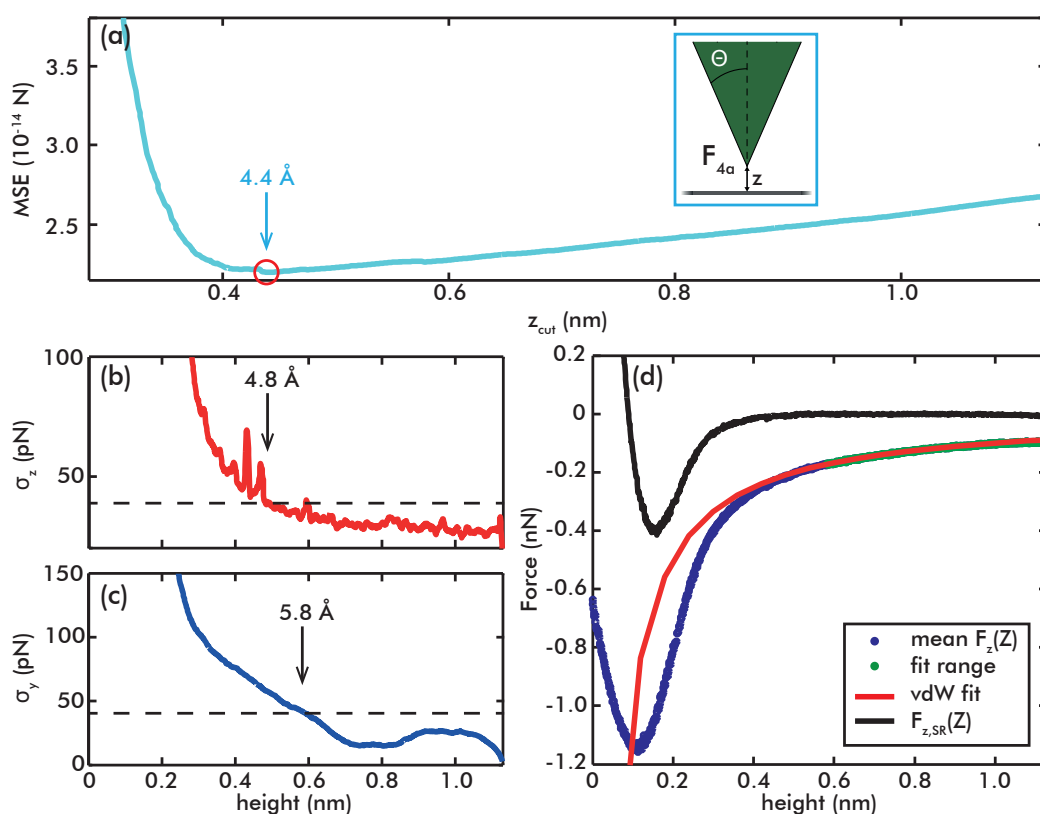


Fig. D.1.: $F_{z,SR}$ extraction of the 2D data on dolomite. (a) Mean squared error (MSE) from fitting a van der Waals model to the mean experimental curve as a function of z_{cut} . The best model is presented in the inset. (b) Standard deviation σ_z of the vertical force F_z . (c) Standard deviation σ_y of the lateral force F_y . Resulting cut-off points are marked in both panels. (d) Mean total vertical interaction force $\overline{F_z}$ (blue), van der Waals interaction force F_{vdW} (red) and resulting mean vertical short-range force $F_{z,SR}$.

For the MSE criterion the z_{cut} can be determined to 4.4 \AA , while for the σ_z and σ_y criteria 4.8 \AA and 6.2 \AA were found. When fitting model F_{4a} to the experimental mean curve (blue, Fig. D.1(d)) using the cut-off from σ_y , the tip was modelled

with the following fit parameters: $\Theta = 81.7^\circ$ and $z_{off} = 0$ nm when H is fixed to 1×10^{-20} J. As previously discussed (Appendix C), an offset of 0 nm might at first seem unusual but is still a possible and realistic description of the tip. Since the confidence intervals for this fit are reasonably well, this fit was chosen for the extraction of $F_{z,SR}$. For all other models the confidence intervals are considerably higher and also offer unrealistic fit parameters which gives further confidence in the conducted fit.

MATLAB Code for fitting a van der Waals Model

The MATLAB Code that I wrote to fit any of the described van der Waals Models from Section 4.3 to the mean $\overline{F_z}$ curve of a given dataset with subsequent subtraction of the conducted fit from the whole data shall be presented here.

At first the desired data is loaded from a struct containing the whole information of a specific force map.

```

1 % Load or prepare data
2 % after storing, data can easily be loaded directly
3 % data_average_save
4 load('fullmeandata.mat');
5
6 % Lowest turning Point in nm;
7 z_min = 0.1673; % Negative of this is the smallest z axis value
8
9 % Identifier of the desired data
10 ident = 'F(Z)-lancz5-sgolay3-smoothafter5';
11
12 % Get the data struct; the function 'helper_finddatabyident' searches
13 % for the desired data
14 fzdatastruct = helper_finddatabyident(afmdata, ident);
15 fvsize = size(fzdatastruct.data);

```

After that, the starting parameters for the fit are chosen.

```

1 %% Start values and bounds for all fit parameters
2 % length are scaled in nm, H is scaled in 10^-18
3 fitparams = struct();
4 % z offset position
5 fitparams.zoff = struct('start', 0.15, 'lower', 0, 'upper', Inf);
6 % physical van-der-Waals models
7 fitparams.H = struct('start', 0.01, 'upper', Inf, 'lower', 0);
8 fitparams.Hret = struct('start', 1.5e-9, 'upper', 2e-8, 'lower', 0);
9 fitparams.R = struct('start', 25, 'upper', 50, 'lower', 10);
10 fitparams.theta = struct('start', pi/4, 'upper', pi/2, 'lower', 0);
11 fitparams.L = struct('start', 5, 'upper', 30, 'lower', 0);
12 fitparams.h1 = struct('start', 2, 'upper', 20, 'lower', 0);
13 % empirical parameters
14 fitparams.B = struct('start', -1.4e-10, 'upper', 1, 'lower', -1);
15 fitparams.a = struct('start', -0.55, 'upper', 10, 'lower', -10);

```

```
16 fitparams.b = struct('start', -2.3, 'upper', 10, 'lower', -10);
```

The following sequence prepares the fit. Here, the cut-off z_{cut} is chosen in pixel as well as the models, which are defined later on in this sequence.

```
1 %% Prepare the fit
2
3 % Select the fit model
4 % Available models: F1a, F1b, F2, F3, F3r, F4a, F4b, F5, F6a, F6b, F7,
5 % F8
6 F = 'F6b';
7
8 % Define the cut-off, in Pixel;
9 z = 500;
10
11 % Define the z-axis including a shift to avoid the pole at z = 0
12 zendidx = length(zaxis);
13
14 zaxis_LR = (zaxis(z:zendidx).*1e9)+z_min;
15 zaxis_full = (zaxis(:).*1e9)+z_min;
16 data_LR = fullmean(z:zendidx);
17
18
19 [xData,yData] = prepareCurveData(zaxis_LR,data_LR);
20
21 % Set up fittype and options.
22 fo = fitoptions('Method','NonlinearLeastSquares');
23
24 % Initialise each model individually (dependency on parameter list)
25 h = 'tflasc';
26
27 %% vdW force F1a: sphere against infinite plane
28 %
29 % Sphere-Plate;
30 % Argento and French, J Appl Phys 80, 6081 (1996)
31 if(strcmp(F, 'F1a'))
32     disp('Used model is F1a');
33     % p is [H, R, z_offset]
34     ft = fittype(@ (H,zoff,z) vdW_F1a([H,25,zoff],z), ...
35         'independent','z', 'options',fo);
36
37 function F = vdW_F1a(p, z)
38
39 H = p(1);
40 R = p(2);
41 zoff = p(3);
42
43 F = -(2.*H.*R.^3) ./ (3.*(z+zoff).^2.*((z+zoff)+2*R).^2);
44
```

```

45
46 %% vdW force F1b: sphere against infinite plane, case z << R
47 %
48 % Sphere-Plate;
49 % Argento and French, J Appl Phys 80, 6081 (1996)
50 elseif(strcmp(F, 'F1b'))
51     disp('Used model is F1b');
52     % p is [H, R, z_offset]
53     ft = fittype(@ (H,zoff,z) vdW_F1b([H,25,zoff],z), ...
54         'independent','z', 'options',fo);
55
56 function F = vdW_F1b(p, z)
57
58 H = p(1);
59 R = p(2);
60 zoff = p(3);
61
62 F = -H.*R./(6.*(z+zoff).^2);
63
64 %% vdW force F2: Full sphere at cone against infinite plane
65 %
66 % Guggisberg, Phys Rev B 61, 11151 (2000)
67 elseif(strcmp(F, 'F2'))
68     disp('Used model is F2');
69     % p is [H, R, theta, z_offset]
70     ft = fittype(@ (H,theta,zoff,z) vdW_F2([H,25,theta,zoff],z), ...
71         'independent','z', 'options',fo);
72
73 function F = vdW_F2(p, z)
74
75 H = p(1);
76 R = p(2);
77 theta = p(3);
78 zoff = p(4);
79
80 F = -(H./6).*(R./(z+zoff).^2) ...
81     + (tan(theta).^2./((z+zoff)+(R.*(1-sin(theta)))) ...
82     - ((R.*(1-sin(theta)))./(z+zoff).^2 ...
83     + (R.*(1-sin(theta)).*(z+zoff))));
84
85
86 %% vdW force F3: sphere at cone against infinite plane
87 %
88 % Argento and French, J Appl Phys 80, 6081 (1996)
89 elseif(strcmp(F, 'F3'))
90     disp('Used model is F3');
91     % p is [H, R, theta, z_offset]
92     ft = fittype(@ (H,theta,zoff,z) vdW_F3([H,25,theta,zoff],z), ...
93         'independent','z', 'options',fo);
94
95 function F = vdW_F3(p, z)

```

```

96
97 H      = p(1);
98 R      = p(2);
99 theta  = p(3);
100 zoff   = p(4);
101
102 F = ((H.*R.^2).*(1-sin(theta)).*(R.*sin(theta)-(z+zoff).*sin(theta)...
103      -R-(z+zoff)).)/((6.*(z+zoff).^2).*(R+(z+zoff) ...
104      -R.*sin(theta)).^2)-((H.*tan(theta)).*(z+zoff) ...
105      .*sin(theta)+R.*sin(theta)+R.*cos(2.*theta)) ...
106      ./((6.*cos(theta)).*(z+zoff)+R-R.*sin(theta)).^2);
107
108
109 %% vdW force F3r: half-sphere at cone against infinite plane
110 % including retardation
111 %
112 % Saint Jean, J Appl Phys 86, 5245 (1999)
113 elseif(strcmp(F, 'F3r'))
114     disp('Used model is F3r');
115     % p is [Hret, R, theta, z_offset]
116     ft = fitype(@(Hret,R,theta,zoff,z) vdW_F3r([Hret,R,theta,zoff], ...
117         z), 'independent','z', 'options',fo);
118
119 function F = vdW_F3r(p, z)
120
121 Hret  = p(1);
122 R     = p(2);
123 theta = p(3);
124 zoff  = p(4);
125
126 F = (-Hret./30).*(1+tan(theta).^2)./((z+zoff)+R ...
127     .*sin(theta)).^2)+ (2.*R-(z+zoff)) ...
128     ./(z+zoff).^3);
129
130
131 %% vdW force F4a: full pyramid with sharp apex against infinite plane
132 %
133 % Zanette, Surf Sci 453, 75 (2000)
134 elseif(strcmp(F, 'F4a'))
135     disp('Used model is F4a');
136     % p is [H, theta, z_offset]
137     ft = fitype(@(theta,zoff,z) vdW_F4a([0.010,theta,zoff],z), ...
138         'independent','z', 'options',fo);
139
140 function F = vdW_F4a(p, z)
141
142 H      = p(1);
143 theta  = p(2);
144 zoff   = p(3);
145
146 F = -(2.*H.*tan(theta).^2)./(3.*pi.*(z+zoff));

```

```

147
148
149 %% vdW force F4b: full pyramid with sharp apex against infinite plane
150 %
151 % Argento and French, J Appl Phys 80, 6081 (1996)
152 elseif(strcmp(F, 'F4b'))
153     disp('Used model is F4b');
154     % p is [H, theta, z_offset]
155     ft = fittype(@(theta,zoff,z) vdW_F4b([0.010,theta,zoff],z), ...
156         'independent','z', 'options',fo);
157
158 function F = vdW_F4b(p, z)
159
160 H     = p(1);
161 theta = p(2);
162 zoff  = p(3);
163
164 F = -(H.*tan(theta).^2)./(6.*(z+zoff));
165
166
167 %% vdW force F5: truncated pyramid with flat apex against infinite
168 % plane
169 %
170 % Zanette, Surf Sci 453, 75 (2000)
171 elseif(strcmp(F, 'F5'))
172     disp('Used model is F5');
173     % p is [H, L, theta, z_offset]
174     ft = fittype(@(H,theta,zoff,z) vdW_F5([H,5,theta,zoff],z), ...
175         'independent','z', 'options',fo);
176
177 function F = vdW_F5(p, z)
178
179 H     = p(1);
180 L     = p(2);
181 theta = p(3);
182 zoff  = p(4);
183
184 F = (-2.*H.*L.^2)./(3.*pi.*(z+zoff).^3).*(1+(tan(theta) ...
185     *(z+zoff)./L)+(tan(theta).^2.*(z+zoff).^2./(L.^2)));
186
187
188 %% vdW force F6a: truncated sphere at pyramidal tip against infinite
189 % plane
190 %
191 %Zanette, Surf Sci 453, 75 (2000)
192 elseif(strcmp(F, 'F6a'))
193     disp('Used model is F6a');
194     % p is [H, R, theta, hsphere, L, z_offset]
195     ft = fittype(@(H,R,h1,theta,L,zoff,z) vdW_F6b([H,R,theta,h1,L, ...
196         zoff],z), 'independent','z', 'options',fo);
197

```

```

198 function F = vdW_F6a(p, z)
199
200 % parameter
201 H      = p(1);
202 R      = p(2);
203 theta  = p(3);
204 hsphere = p(4);
205 L      = p(5);
206 z_offset = p(6);
207
208 F = (-H/6).*(((hsphere.^2.*(3.*R.*(z+z_offset)+R.*hsphere-(z ...
209     +z_offset).*hsphere))./(z+z_offset).^2.*(z ...
210     +z_offset+hsphere).^3))+L.^2./(z+z_offset ...
211     +hsphere).^3)+(4.*tan(theta).*(L+tan(theta) ...
212     *(z+z_offset+hsphere))./(pi.*(z+z_offset+hsphere).^2));
213
214
215 %% vdW force F6b truncated sphere to pyramidal tip against infinite
216 %plane
217 %
218 %Zanette, Surf Sci 453, 75 (2000)
219 % Substitute L = sqrt(R^2-(R-hsphere)^2) in F6a
220 elseif(strcmp(F, 'F6b'))
221     disp('Used model is F6b');
222     % p is [H, R, theta, hsphere, z_offset]
223     %%% This resets start and/or bounds:
224     fitparams.R.upper = 50;
225     fitparams.R.start = 20;
226     %%% By removing the 'H' from the anonymous function and setting it
227     %%% to 0.04 constrains H to 0.04 and removes this fit parameter
228     %%% in this case
229     ft = fittype(@(H,theta,h1,zoff,z) vdW_F6b([H,25,theta,h1,zoff], ...
230         z), 'independent','z', 'options',fo);
231
232 function F = vdW_F6b(p, z)
233
234 % parameter
235 H      = p(1);
236 R      = p(2);
237 theta  = p(3);
238 hsphere = p(4);
239 z_offset = p(5);
240
241 % function value
242 F = (-H/6).*(((hsphere.^2.*(3.*R.*(z+z_offset)+R.*hsphere-(z ...
243     +z_offset).*hsphere))./(z+z_offset).^2.*(z ...
244     +z_offset+hsphere).^3))+((R.^2-(R-hsphere).^2) ...
245     ./z+z_offset+hsphere).^3)+(4.*tan(theta) ...
246     *(sqrt(R.^2-(R-hsphere).^2)+tan(theta).*(z ...
247     +z_offset+hsphere))./(pi.*(z+z_offset+hsphere).^2));
248

```

```

249 %% Emprirical formula F7
250 %
251 % Langkat et al., Surf Sci 527, 12 (2003)
252 elseif(strcmp(F, 'F7'))
253     disp('Used model is F7 (emp.)');
254     % p is [B, z_offset]
255     ft = fitype(@(B,zoff,z) vdW_F7([B,zoff],z), ...
256         'independent','z', 'options',fo);
257
258 function F = vdW_F7(p, z)
259
260 % parameter
261 B     = p(1);
262 zoff = p(2);
263
264 F = B./(z-zoff);
265
266 %% Emprirical formula F8
267 %
268 % Hauptmann et al., New Journal of Physics, 14, 073032 (2012)
269 elseif(strcmp(F, 'F8'))
270     disp('Used model is F8 (emp.)');
271     % p is [a, b, zoff]
272     ft = fitype(@(a,b,zoff,z) vdW_F8([a,b,zoff],z), ...
273         'independent','z', 'options',fo);
274 function F = vdW_F8(p, z)
275
276 % parameter
277 a     = p(1);
278 b     = p(2);
279 zoff = p(3);
280 F = a.*(z+zoff).^b;
281
282
283 else
284     disp(['Model <' F '> is unknwon']);
285     break;
286 end
287
288 % Set further options for the fit
289 opts = fitoptions(ft);
290 opts.Robust = 'Off';
291 opts.Display = 'Off';
292 opts.Algorithm = 'Trust-Region';
293 o = 'hnis';
294 opts.MaxIter = 1000000;
295 opts.MaxFunEvals = 1000000;
296 opts.DiffMaxChange = 1e-6;
297 opts.DiffMinChange = 1e-6;
298 opts.TolFun = 1e-6;
299 opts.TolX = 1e-6;

```

```

300
301 % Set start values and boundaries for relevant parameters
302 % Note: If non-default parameter names chosen, this function might
303 % fail!!!
304 [s u l] = fit_find_start_boundaries(ft, fitparams, F);
305 opts.StartPoint = s;
306 opts.Upper = u;
307 opts.Lower = l;

```

Now, the actual fit can be conducted, including a subtraction from a single test curve as well as from the whole data set. Furthermore, relevant positions like the force minimum F_{\min} , its position z_{\min} and the zero-crossing z_{zero} are determined.

```

1 % Fit model to data.
2 [fitresult,gof,odata] = fit(xData,yData,ft,opts);
3 % [fitresult,gof,odata] = fit(zaxis,fullmean,ft,opts);
4
5 printfitstats(fitresult,gof,odata)
6
7 % Subtract data from a single curve and the mean curve
8 curve = squeeze(fzdatastruct.data(60,1,:)*1e9);
9 data_SR_curve = curve-fitresult(zaxis_full);
10 x = 1:length(zaxis_full);
11 for i=1:fvsize(1)
12     data_SR_full(i,1,x) = squeeze(fzdatastruct.data(i,1,x).*1e9)-
13         fitresult(zaxis_full);
14 end
15
16 data_SR = fullmean-fitresult(zaxis_full);
17
18
19 %% Handle the resulting parameters
20 n = 'hewein';
21 fres = struct('zoff', 0, 'H', NaN, 'Hret', NaN, 'L', NaN, 'R', ...
22             NaN, 'h1', NaN, 'theta', NaN);
23 try
24     fres.zoff = fitresult.zoff;
25 catch err
26 end
27 try
28     fres.H = fitresult.H;
29 catch err
30 end
31 try
32     fres.R = fitresult.R;
33 catch err
34 end
35 try
36     fres.h1 = fitresult.h1;

```

```

37 catch err
38 end
39 try
40     fres.theta = fitresult.theta;
41 catch err
42 end
43 try
44     fres.L = fitresult.L;
45 catch err
46 end
47 % Calculate L for case F6b
48 if strcmp(F, 'F6b')
49     fres.L = sqrt(25^2 - (25 - fres.h1)^2);
50 end
51
52 %% Find relevant positions
53 %% Smooth short-range data at the beginning
54 data_SR_smooth = smooth(data_SR, 20);
55
56 % Zero-crossing
57 check = find(data_SR_smooth(1:300) > 0);
58 l = 'derlo';
59 if check >= 1;
60     reps = find(data_SR_smooth < 0);
61     zero_pixel = reps(1);
62     zzero = zaxis_full(zero_pixel)
63
64 % Force minimum
65     Fmin = min(data_SR_smooth)
66
67 % Position of force minimum
68     zmin_pixel = find(data_SR_smooth == min(data_SR_smooth));
69     zmin = zaxis_full(zmin_pixel)
70
71 else
72 % Force minimum
73     Fmin = min(data_SR_smooth)
74
75 % Position of force minimum
76     zmin_pixel = find(data_SR_smooth == min(data_SR_smooth));
77     zmin = zaxis_full(zmin_pixel)
78
79 %% Subtract vdW-Fit from whole dataset
80 x = 1:length(zaxis_full);
81 for i=1:fvsize(1)
82     data_SR_full(i,1,x) = squeeze(fzdatastruct.data(i,1,x) .* 1e9)
83         - fitresult(zaxis_full);
84 end

```

Finally, the data are plotted

```

1 %% Plot fit with data.
2
3 % Plot the mean curve
4 figure
5 hold on
6 plot(zaxis_full,fullmean,'.')
7 plot(zaxis_LR,data_LR,'.g')
8 plot(fitresult, '-.r');
9 plot(zaxis_full,data_SR, '-k')
10 legend('Mean total F_z(Z)', ...
11        'Selected Fitrangle', ...
12        'vdW-Fit', ...
13        'Mean short-range F_z(Z)');
14
15 % Make title and label axes for the mean curve
16 % Der Code enthaelt ein Geheimniss!
17 title(sprintf(['z: %6.0f, z_{offset}: %0.5g, ' ...
18              'H: %0.5f 10^{−18} J, \n' ...
19              'L: %2.2f nm, R: %0.2f nm, hsphere: %2.2f nm, ...
20              theta: %2.2f '], z, fres.zoff, fres.H, fres.L, ...
21              fres.R, fres.h1, fres.theta/pi*180));
22 ylim([-0.8,0.2]);
23 xlim([0, 1.1+z_min]);
24 xlabel( 'z in nm' );
25 ylabel( 'F in nN' );
26 grid on
27
28
29 % Plot a single curve
30 figure
31 hold on
32 plot(zaxis_full,curve,'.')
33 plot(fitresult, '-.r');
34 plot(zaxis_full,data_SR_curve, '-k')
35 legend('Selected F_z(Z)', ...
36        'vdW-Fit', ...
37        'Short-range F_z(Z)');
38
39 % Make title and label axes
40 title(sprintf(['z: %6.0f, z_{offset}: %0.5g, ' ...
41              'H: %0.5f 10^{−18} J, \n' ...
42              'L: %2.2f nm, R: %0.2f nm, hsphere: %2.2f nm, ...
43              theta: %2.2f '], z, fres.zoff, fres.H, fres.L, ...
44              fres.R, fres.h1, fres.theta/pi*180));
45 ylim([-1.0,0.4]);
46 s = strcat(l,o,h,n)
47 xlim([0,1.1+z_min]);
48 xlabel( 'z in nm' );
49 ylabel( 'F in nN' );
50 grid on
51

```

```

52
53 % Plot the force minimum, the position and the zero-crossing
54 figure
55 plot(zaxis_full,data_SR, '-g')
56 hold on
57 plot(zaxis_full,data_SR_smooth, '-r')
58 plot(zmin,Fmin, '.b', 'MarkerSize',20)
59 plot(zzero,data_SR_smooth(zero_pixel), '.b', 'MarkerSize',20)
60 xlabel( 'z in nm' );
61 ylabel( 'F in nN' );
62 xlim([0,0.8])
63 ylim([Fmin-0.1,0.2])
64 legend('raw data', 'smoothed data', 'marker', 'Location', ...
65         'SouthEast');
66
67 % Show the dataset with short-range forces
68 figure
69 imagesc(flipud(squeeze(data_SR_full(:,1,1:1000))'))
70 colormap(reigreen(256))
71 caxis([-0.3 0.2]);

```


Acknowledgements

An dieser Stelle möchte ich allen Menschen danken die dazu beigetragen haben, dass diese Arbeit in der Form existieren kann, wie sie heute vorliegt:

- ... [REDACTED] gilt mein größter Dank, da sie mir die Möglichkeit gab, eine Arbeit in ihrer Gruppe an einem mehr als spannenden und faszinierenden Thema verfassen zu können. Ihr Vertrauen und die stets offene und unkomplizierte Art waren beispiellos.
- ... [REDACTED] sei gedankt für die freundliche und unkomplizierte Übernahme des Zweitgutachtens,
- ... [REDACTED] für den Prüfungsvorsitz.

Nicht zu vernachlässigen ist natürlich die unschätzbare Hilfe der Kollegen des [REDACTED] [REDACTED] Stete Hilfestellungen, engagiertes Mitdenken und der offene sowie humorvoll unkomplizierte Umgang miteinander waren immer von unschätzbarem Wert, auch neben der Arbeit. Das Zusammensein mit euch, bei und auch fern der Arbeit, war mir immer eine große Freude. Besonders hervorheben möchte ich jedoch

- ... [REDACTED] als meinen Vorgänger, ohne dessen Zutun weder die Extraktion der kurzreichweitigen Kräfte noch die Interpretation der Kraftdaten auf Kalzit in diesem Ausmaße möglich gewesen wären. Die zahlreichen und oft langen Diskussionen waren mir stets eine Freude sowie eine große Hilfe.
- ... [REDACTED] denn seine, oft humorvolle, Hilfeleistung die man jederzeit in Anspruch nehmen konnte hat mich in weitaus mehr als nur wissenschaftlichen Belangen, jedoch hier ganz besonders, vorangebracht.
- ... [REDACTED] für die Diskussion über die mittlere quadratische Abweichung.

Außerhalb des Arbeitskreises möchte ich mich vielmals bei [REDACTED] für die immer freundliche und kompetente Hilfestellung bei allen MATLAB Problemen sowie den sehr lehrreichen MATLAB Kurs bedanken. Ohne sie hätte das Skript zum Fitten der langreichweitigen Wechselwirkung sicher lange nicht so gut funktioniert.

Abseits der Wissenschaft geht mein Dank an

- ... [REDACTED] die viel Geduld beim Korrekturlesen meiner Arbeit aufbrachten und trotz des immer enger werdenden Zeitrahmens dies auch stets ohne zu murren zügig taten.
- ... [REDACTED], welches immer für einen freien Kopf sorgte und meine Abwesenheit in stressigen Zeiten verständnisvoll akzeptierte.
Gambate!
- ... [REDACTED] die mir immer Unterstützung entgegenbrachten und für die nötige Entspannung sorgten.
- ... [REDACTED] für alles. Mehr muss nicht gesagt werden.



Publications and presentations

Publications in peer-reviewed journals

- **Discriminating short-range from van der Waals forces using total force data in noncontact atomic force microscopy**
S. Kuhn, P. Rahe
Phys. Rev. B **89**, 235417 (2014)
- **Identifying the absolute orientation of a low-symmetry surface in real space**
S. Kuhn, M. Kittelmann, Y. Sugimoto, M. Abe, A. Kühnle, P. Rahe
Phys. Rev. B **90**, 195405 (2014)
- **Is Calcite (10.4) a Chiral Surface?**
P. Rahe, S. Kuhn, A. Kühnle
Journal of unsolved Questions **3**, 21 (2013)
- **Exploring the possibilities of metal-organic coordination networks on calcite (10.4)**
S. Kuhn, L. Schüller, R. Bechstein, A. Kühnle
in preparation

Talks

(presenting author underlined)

- **Determining the absolute orientation of a low-symmetry surface**
S. Kuhn, M. Kittelmann, Y. Sugimoto, M. Abe, A. Kühnle, P. Rahe
(NC-AFM 2013, Maryland, USA)
- **Revealing and understanding atomic-scale details in the force-field above CaCO₃**
S. Kuhn, M. Kittelmann, Y. Sugimoto, M. Abe, A. Kühnle, P. Rahe
(Physics Boat Workshop 2014, Helsinki, Finland)

Poster Presentations

(presenting author underlined)

- **3D force maps on CaCO₃ (10.4) at room temperature**
S. Kuhn, M. Kittelmann, Y. Sugimoto, M. Abe, A. Kühnle, P. Rahe
(NC-AFM 2012, Český Krumlov, Czech Republic)
- **Measuring Force-Fields on Bulk Insulators with Atomic Resolution**
S. Kuhn, M. Kittelmann, Y. Sugimoto, M. Abe, A. Kühnle, P. Rahe
(MRS 2012, Boston, USA)
- **Extracting short-range forces from total force data**
S. Kuhn, P. Rahe
(NC-AFM 2014, Tsukuba, Japan)

Curriculum vitae (educational)

Stefan Kuhn

born on June 12th 1986 in Frankenthal (Pfalz)



1992 - 1996 Grundschule Eppstein-Flomersheim

1996 - 2005 Karolinen-Gymnasium Frankenthal

2006 - 2012 Johannes Gutenberg-Universität Mainz
Studies of chemistry

2012 Graduation with degree "Diplom Chemiker"
Thesis: "3D Kraftspektroskopie auf der Kalzit (10.4)-Spaltfläche"
supervised by Prof. Dr. Angelika Kühnle

2012 - 2015 Johannes Gutenberg-Universität Mainz
Doctoral studies supervised by Prof. Dr. Angelika Kühnle

